UNIVERSITY OF BELGRADE

FACULTY OF TECHNOLOGY AND METALLURGY

WALEED MOHAMMED OMYMEN

PHOTOELECTROCHEMICAL CELL BASED ON TITANIUM DIOXIDE NANOTUBES MODIFIED BY IRON OXIDE

Doctoral Dissertation

Belgrade, 2018

UNIVERZITET U BEOGRADU

TEHNOLOŠKO-METALURŠKI FAKULTET

WALEED MOHAMMED OMYMEN

FOTOELEKTROHEMIJSKA ĆELIJA NA BAZI NANOCEVI TITAN-DIOKSIDA MODIFIKOVANIH GVOŽĐE OKSIDOM.

doktorska disertacija

Beograd, 2018

Mentor:

Dr Branimir Grgur, redovni profesor,
Univerzitet u Beogradu, Tehnološko-metalurški fakultet

Članovi komisije:

Dr Milica Gvozdenović, vanredni profesor,
Univerzitet u Beogradu, Tehnološko-metalurški fakultet

Dr Branimir Jugović, naučni savetnik,
Institut tehničkih nauka – SANU, Beograd

Datum odbrane: ___ ___ _____ god.

ACKNOWLEDGEMENT

I would like to express this appreciation to Professor Branimir Grgur, for his supervision, guidance, encouragements, and advice throughout the duration of study and experimental work.

I would also to thanks sincere appreciation to my Mentor Professor Branimir Grgur, Professor Milica Gvozdenović and Dr. Branimir Jugović, for guideless during the work on this doctoral dissertation.

Finally deep thanks to the Libyan Government, and my family for their patent, and encouragements during my Ph.D study at Belgrade University.

Thank you.

PHOTOELECTROCHEMICAL CELL BASED ON TITANIUM DIOXIDE NANOTUBES MODIFIED BY IRON OXIDE

ABSTRACT

The fast reaction of forced hydrolysis of iron(III) nitrate in hypochlorite solution at room temperature, leads to the formation of mainly hematite, α-Fe_2O_3. Successive ion adsorption and reaction (SILAR) is applied to decorate an electrochemically formed TiO_2 nanotube electrode. The anodic photoelectrochemical behavior of pure TiO_2-NT's and modified electrodes are investigated in a sulfate containing solution at pH=9.2. It is shown that such a modification leads to an increase of anodic photoactivity, as well as that at the same current density, the photoelectrochemical cell with a modified electrode operates at a voltage lower by 0.7 V. The band gap and flat band potentials are estimated, and the structure of the band gap and possible charge transfer reactions and mechanism are discussed.

The electrochemical oxidation of the urea in near neutral pH is investigated on platinum electrode. It is shown that oxidation reaction is practically inhibited up to the potentials of ~0.9 V. The same reaction is investigated onto electrochemically obtained titanium dioxide nanotubes modified by hematite using SILAR method. It is shown that such system possesses electrocatalytic activity at very low potentials, and activity can be further improved by the illumination of the electrode in the photo-assisted reaction. The possible application of the photoactive anode is considered in the application of urea based water electrolysis and urea based fuel cell.

Keywords: Hematite; Forced hydrolysis; Photoelectrochemical cell; Urea; Oxidation

Scientific field: Technological engineering

Specific scientific field: Chemical engineering

FOTOELEKTROHEMIJSKA ĆELIJA NA BAZI NANOCEVI TITAN-DIOKSIDA MODIFIKOVANIH GVOŽĐE OKSIDOM

REZIME

Brza reakcija prisilne hidrolize gvožđa (III) nitrata u rastvor hipohlorita na sobnoj temperaturi, dovodi do stvaranja uglavnom hematita, α-Fe_2O_3. Sukcesivna jonska adsorpcija i reakcija (SILAR) primenjena je za modifikaciju elektrohemijski formirane elektrode od TiO_2 u obliku nanocevi. Anodno fotoelektrohemijsko ponašanje čistih TiO_2-NT i modifikovanih elektroda ispitano je u rastvoru sulfata pri pH = 9.2. Pokazano je da takva modifikacija dovodi do povećanja anodne fotoaktivnosti, kao i da kod iste gustine struje fotoelektrohemijska ćelija sa modifikovanom elektrodom radi na naponu manjem za 0,7 V. Procenjena je vrednost širine energetske barijere i potencijala izravnatih zona. Diskutovano je o strukturi energetske barijere ispitivanih materijala, mogućim reakcijama i mehanizmu prenosa naelektrisanja.

Elektrohemijska oksidacija uree u rastvoru pH=9,2 je ispitana na platinskoj elektrodi. Pokazano je da je reakcija oksidacije praktično inhibirana do vrednosti potencijala od ~ 0,9 V. Ista reakcija je ispitana na elektrohemijski dobijenim nanocevima titan-dioksida modifikovanim hematitom koristeći SILAR metodu. Pokazano je da takav sistem poseduje elektrokatalitičku aktivnost pri veoma niskim potencijalima, a aktivnost se može dodatno poboljšati osvetljavanjem elektrode. Moguća primena fotoaktivne anode je razmatrana za primenu u elektrolizi vode na bazi uree i gorivne ćelije na bazi uree.

Ključne reči: Hematit; Prinudna hidroliza; Fotoelektrohemijska ćelija; Urea; Oksidacija
Naučna oblast: Tehnološko inženjerstvo
Uža naučna oblast: Hemijsko inženjerstvo

CONTENTS

1. INTRODUCTION

From the Industrial Revolution to the present day, there was, amazing, civilization exponential growth in demand for energy. The primary use of non-renewable energy sources-combustion leads to enormous emissions of greenhouse gases (CO_2, SO_2, NO_x, etc.) which leads to major climate changes, accompanied by, among other things, an increase in average annual temperature. In order to better, mitigate the disastrous effects of greenhouse gas emissions today there are more serious approach to the use of renewable and other forms of alternative energy sources. In addition to bio-energy, geothermal sources and wind power, one of the most important aspects are the radiant energy of the Sun. In the last ten years, great attention is paid to photoelectrochemical conversion of solar energy due to the simplicity and far lower prices of the photoelectrochemical converters compared to systems based on p-n junction [1, 2].

Photoelectrochemical water splitting is a very promising route for the environmentally friendly production of hydrogen and, for example, simultaneous degradation of various organic waste [3,4]. During a typical photo-water splitting on the photoanode, generated holes oxidize water to oxygen or other oxygen containing species (OH^* radicals, H_2O_2 or HO_2^-). Electrons produced via an external circuit are transferred to e.g. metallic cathode and involved in the hydrogen evolution reaction [5,6]. In the photoelectrochemical cell (PEC), large overpotentials are typically associated with the photoanode, so, in principle, an external bias should be applied [5,6]. External bias also provides the necessary overvoltage on the metallic cathode, required to sustain the current flow, and to increases the band banding in the semiconductor to maintain the charge separation rate [5].

Many different semiconductors are investigated as the anodes in photo-water splitting [7], but due to an easy synthesis, excellent corrosion resistance in solutions of different pH, titanium dioxide is the most widely studied photoanode materials.

Unfortunately, the band gap of ~3.2 eV allows the absorption of only UV light, which is only ~5% of total Sun irradiance. From that reason, different nanostructures are examined in combination with TiO_2 in order to improve absorption characteristics. Numerous efforts are made to improve the design, fabrication and modifications of the nanostructured materials used in the PEC cell. Accordingly, an efficient photoanode based on visible-light-responsive semiconductors can be obtained using various strategies such as: doping, metal ion loading, composites of mixed oxides, bilayered systems, etc. [8, 9]. Among different materials, one of the most widespread metal oxides on Earth, iron oxide, especially hematite, α-Fe_2O_3, was the subject of intense research for several decades. In particular, the combination of a relatively small bandgap of ~2.2 eV, and the related visible light absorption, natural abundance, low cost, and stability under deleterious chemical conditions has made it ideal for many potential applications [10, 11]. Hardee and Bard [12] first investigated hematite (α-Fe_2O_3) as a material for photoelectrochemistry in 1976, reporting that α-Fe_2O_3 responded to light of wavelength ≤500 nm. Since that time, α-Fe_2O_3 has been extensively investigated as a promising photocatalytic material for water splitting [13]. Despite these advantages, the photoactivity of α-Fe_2O_3 suffers from limitations that result in low efficiency. These include relatively low absorptivity in the visible region, short carrier lifetime (~10−12 μs), and short hole diffusion length, 2−4 nm [14]. On the other hand, different iron oxihydroxides showed good catalytic activity for the oxygen evolution reaction [15, 16, 17, 18, 19]. Different methods and procedures are adopted for the synthesis of the iron oxihydroxides by almost all known wet chemical methods, which include precipitation at ambient/elevated temperatures, surfactant mediation, emulsion/micro-emulsion synthesis, electrodeposition etc. [11, 20]. One of the widespread methods is forced hydrolysis under elevated temperatures in the autoclave over a relatively long period of time [21, 22]. This method is also used as chemical bath deposition method, for the modification of TiO_2 surfaces [23, 24].

Successive ion layer adsorption and reaction (SILAR) is one of the simplest ways to obtain metal oxide thin films at room temperature in a relatively short time [25, 26, 27].

To the best of my knowledge, this method has not been employed for TiO_2 surface modification. Hence, the main goal of this thesis, is to investigate the

possibilities for the modification of TiO_2-nanotubes (NT's) with SILAR deposition of iron oxide as a potential anode material for water splitting and urea photooxidation as a model systems for organic wastes.

2. THEORETICAL PART

The photoelectrochemical energy conversion may be based on electrochemical photovoltaic cells, with typical representatives: dye sensitizes solar cell (DSSC) and quantum dots sensitized solar cell (QDSSC) [28, 29], photovoltaic fuel cells, which can be used for simultaneous oxidation of various fuels from biomass or degradation of organic waste product [30, 31]. Also, photoelectrochemical cells can be applied to the photoelectrochemical water electrolysis [32], or for the hydrogen production and simultaneous degradation of organic matter [7], as well as in the photocatalytic reaction [33, 34].

2.1. Basic principles of photoelectrochemical reactions

Unlike conventional electrochemical reactions in a photoelectrochemical reactions are involved pairs of the electrons (e^-) and holes (h^+) generated by photon photoexcitations with energy *hv*, from the lower valence-band (VB) to a higher level of conducting-band (CB), Figure 2.1 [35].

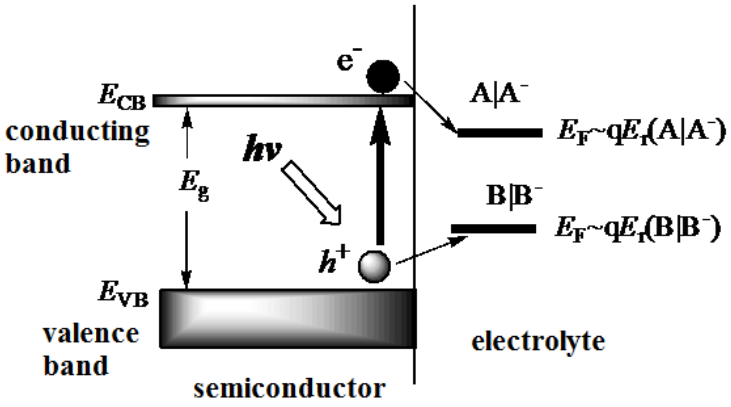

Figure 2.1. Schematic representation of photo-excitation of a semiconductor in an electrolyte [35].

The width of the gap, E_g, which is necessary that an electron jump is called the energy barrier or band gap energy. The electron can reduce species in the electrolyte, while holes (electron acceptor) can oxidize species in the electrolyte. For typical semiconductor ranges from 0.5 to ~ 4 eV (1 eV = 1.60219×10^{-19} J), as shown in Table 1 [36]. Thus, the resulting photoelectrons or holes depending on the type of semiconductors may react with the redox pair contained in the electrolyte, the jump at the Fermi level (E_F), wherein the reaction takes place is called photoelectrochemical reaction [5].

Table 2.1. Typical values of the band gap energy of selected semiconductor [36].

Symbol	E_g / eV	Symbol	E_g / eV
Si	1.12	ZnSe	2.7
Ge	0.67	ZnS	3.54
Se	1.74	ZnTe	2.25
Te	0.33	Cu_2S	1.2
BP	2	PbSe	0.27
BAs	1.5	PbS	0.37
AlP	2.45	PbTe	0.32
AlAs	2.16	SnS_2	2.2
AlSb	1.6	TiO_2 anatase	3.2
GaP	2.26	TiO_2 rutile	3.02
GaAs	1.43	TiO_2 brookite	2.96
InP	1.35	Cu_2O	2.17
InAs	0.36	CuO	1.2
CdSe	1.74	SnO_2	3.7
CdS	2.42	GaSe	2.1
CdTe	1.49	$CuInSe_2$	1
ZnO	3.37	Ag_2S	0.91

In contrast with the conventional photovoltaic cells, which form a p-n junction, photoelectrochemical reactions occurred at the semiconductor-electrolyte interface [5]. The photoelectrochemical behavior is based mainly on the use of p or n semiconductor without forming a p-n junction. Depending on the type of semiconductor, which is determined by the majority charge carriers (electrons for n-type, hole for p-type) will depend on the semiconductors position of the Fermi level. In a n-type semiconductor Fermi level is positioned closer to the conducting zone, while in the p-type semiconductor Fermi level is positioned closer to the valence zone. Figure 2.2 provides a simplified schematic representation of the position of the Fermi level, valence and conduction zone of the n and p type of semiconductor, before contact, after contact with the electrolyte which contain a redox couple in the dark, and after irradiation [5, 37]. In the contact with the electrolyte the balancing of the Fermi level of the semiconductor

and electrolyte occured, whose position is determined by the statistical distribution of the charge state of oxidized and reduced species DOS (density of state). Because the redox reaction are in most cases very fast, balancing the Fermi level is done by moving the Fermi level of the semiconductor, in a relatively thin surface layer. This leads to shifts in the energies of valence and conduction zone (bend alignment), against the local relative positions of the zero vacuum energy. On the side of the electrolyte, there is a small potential drop, $\Delta\psi_H$ ~ 60 mV, in the so-called Helmoltz double layer. After illumination, it comes to the formation of electron-hole pairs (*e*-*h*) as well as to the local separation of the quasi-Fermi level of minority charge carriers, which repulsions re-shift the valence and conductive band. Photoelectrochemical reaction occurs when electrons from the redox couple react with a hole formed in the valence zone of the n-type semiconductor (oxidation), or when an electron from a conductive zone of p-type semiconductor jump on the Fermi level of a redox pair (reduction).

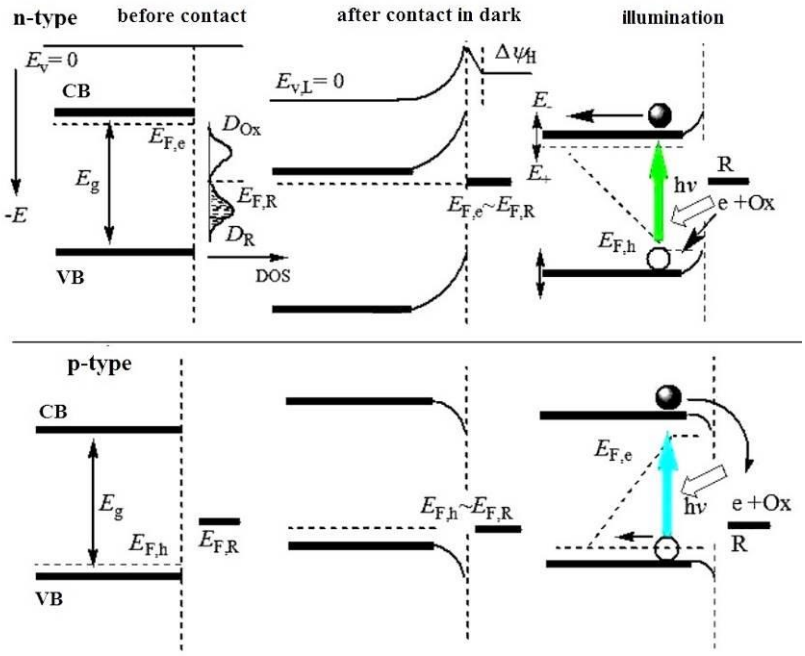

Figure 2.2. Simplified schematic representation of the Fermi level position of valence and conduction band of n-type and p-type of semiconductor, before contact, by contact with the electrolyte that contain a redox couple in the dark and after exposure to light [35].

For the efficient operation of the semiconductor, the most important value is the width of the energy barrier, E_g, and the energy of the photon (E_{ph}) must be greater or equal to the energy barrier. The link between these two values can be established via Einstein-Planck equation [38]:

$$E_{ph} > E_g = h\nu_{min} = \frac{h}{c\lambda_{min}} \tag{2.1}$$

where ν –is a frequency, λ- is a wave length and c- is a speed of light.

By rearranging, it follows:

$$E_g(\text{eV}) = \frac{1240}{\lambda_{min}(\text{nm})} \tag{2.2}$$

- If the $E_{ph} \leq E_g$, the photon does not have sufficient energy to cause a leap of valence electrons to the conduction band.

- If the $E_{ph} \geq E_g$, the photon has enough energy to leap of valence electrons to the conductive band.

From Table 2.1 and using the equation 2.2 can be easily determine the minimum wavelength needed for the excitation of photoelectrons of a semiconductor.

Because, the width of the energy barrier determines the minimum wavelength radiation that can cause photo-excitation, Figure 2.3 shows the dependence of E_g on the wavelength and compared with the spectrum of the solar radiation. From the Figure 2.3 can be concluded that the semiconductors with the energy gap of 1.65-3.0 eV will be active in the visible region of the spectrum (~ 400-750 nm), with E_g> 3.25 in the ultraviolet, UV, and with E_g <1.65 in the infrared, IR spectrum.

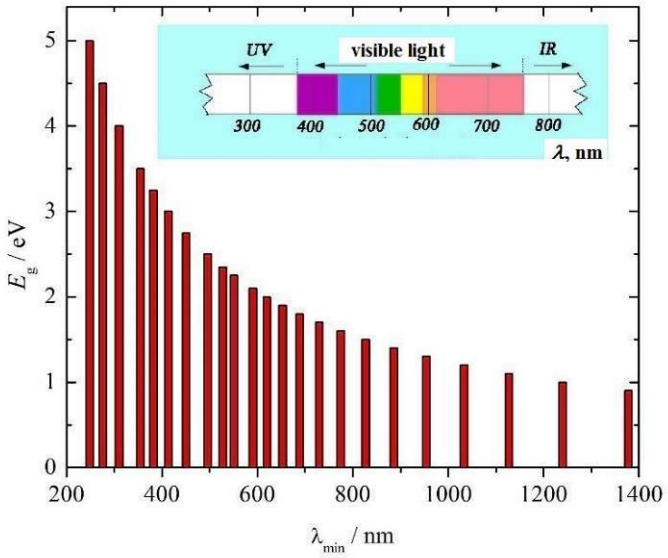

Figure 2.3. Dependence of the energy gap of the semiconductor on the minimum wavelength which can cause photo-excitation [35].

That photoelectrochemical reaction occur, the following rules apply: electron can make the jump to the Fermi level of redox, which has a higher potential value of the conductive zone, where the reduction takes place. Hole can accept electron (recombination) with redox pair (usually with the Fermi level), which has a lower value of the potential of the valence band, wherein the oxidation takes place, as shown in Figure 2.4

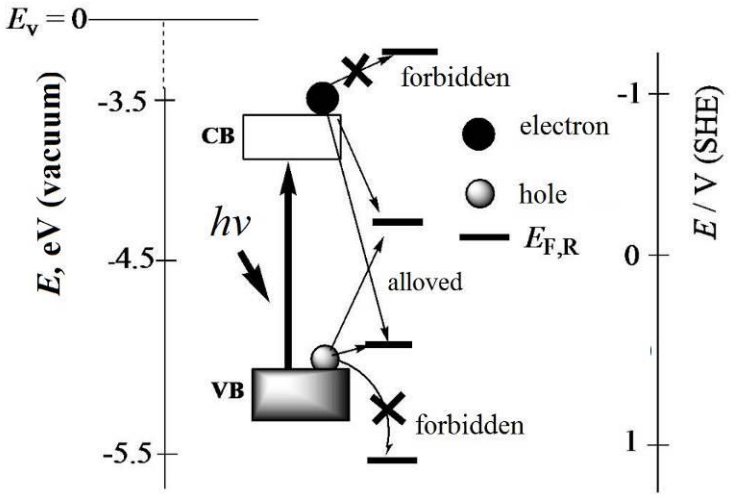

Figure 2.4. Allowed are forbidden passes of photoelectrons and holes during photoelectrochemical reactions in the presence of redox species with different positions of the Fermi level [35].

The equilibrium potential of the redox couple, O|R can be approximately identified with the Fermi levels, so it follows that [5]:

$$E_{\mathrm{F,R}} \sim E_{\mathrm{r}}(\mathrm{O}\,|\,\mathrm{R}) = E_{\mathrm{r}}^{\mathrm{o}}(\mathrm{O}\,|\,\mathrm{R}) - \frac{2.3RT}{nF}\log\frac{a(\mathrm{R})}{a(\mathrm{O})} \tag{2.3}$$

On the other hand the connection between the redox potential in volts, V, according to the standard hydrogen reference electrode (by definition, $E_{\mathrm{SHE}} = 0$) and absolute vacuum scale in eV, is given [39]:

$$E_{\mathrm{F,R}} = -eE\ (\mathrm{abs}) = -eE_{\mathrm{r}}\ (vs.\ \mathrm{SHE}) - 4.44 \pm 0.01\ \ \text{in eV} \tag{2.4}$$

The value of -4.44 eV represents the electrons work function of the standard hydrogen reference electrode. The characteristic values of the energy of the photoelectrochemical cell with the n-type semiconductor and the cathode of, for example platinum, are given in Figure 2.5 [40].

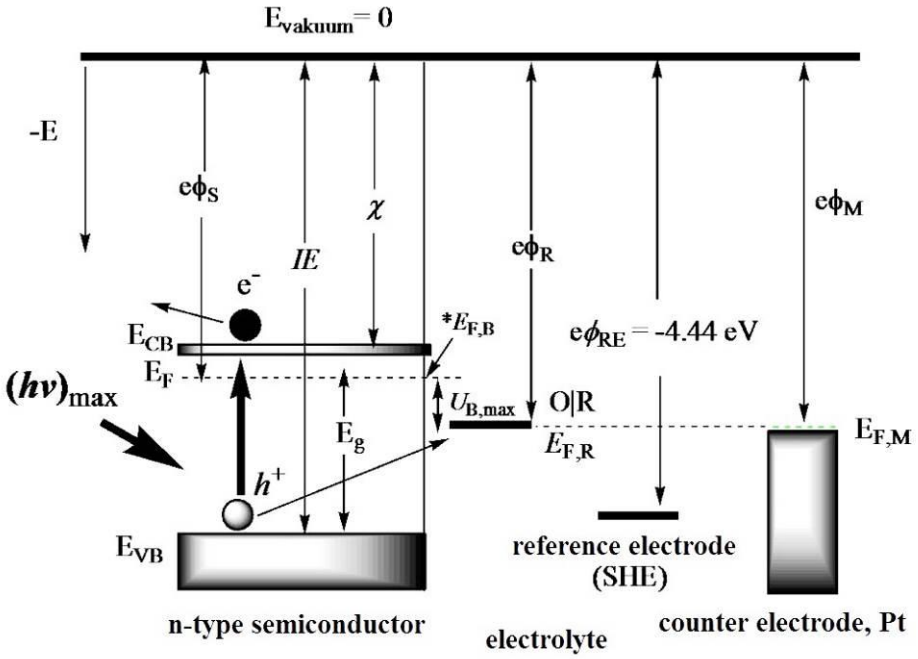

Figure 2.5. Schematic representation of the n-type semiconductor electrode showing the energies in relation to the absolute vacuum scale and their relation to the standard hydrogen electrode. χ -affinity of electrons, IE- ionization energy, ϕ –work function of the electrons, E_{F}-energy of the Fermi level [40].

When the intensity of the radiation is maximal (saturation), a full leveling of the semiconductor zone occurs. The potential corresponding to the Fermi level of fully leveled zones is called flat band potential, $*E_{F,B}$. The difference in the potential of the Fermi levels of redox and flat zones is the maximum voltage, $U_{B,max}$, which a photoelectrochemical cell can produce in theory. Movement of the valence and conductive zone can be performed in addition to the change in the intensity of radiation, and controlled by the external potential versus the reference electrode.

In order for some photoelectrochemical reaction to occur, in conjunction with the width of the energy barrier, the energy positions of the valence and conductive zone are very important. For the most commonly used semiconductors based on oxide and metal sulfide, these positions are shown in Figure 2.6 [41].

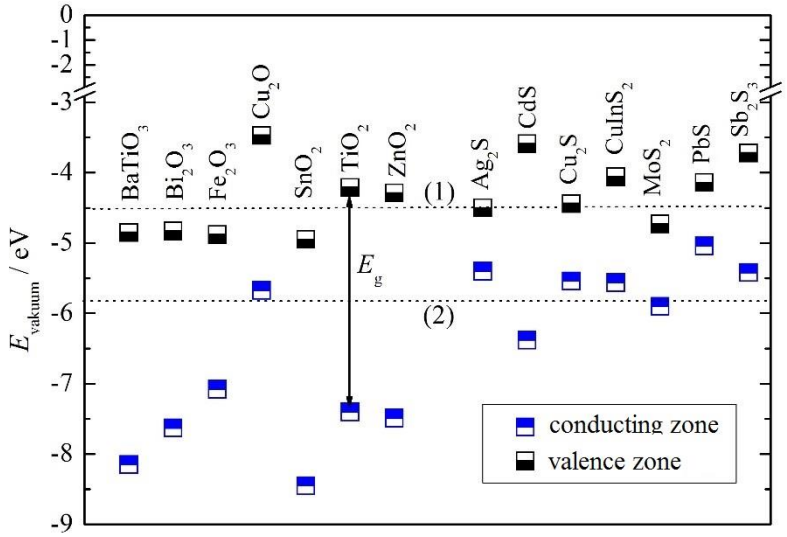

Figure 2.6. Position of valence and conductive zones in relation to the vacuum scale of the most commonly used semiconductor materials at pH = 0 [41].

The dotted line (1) in Figure 2.6 shows the potential for hydrogen reaction:

$$E_r(H^+|H_2) = -0{,}0591pH \sim -4.5 \text{ eV (at pH=0)} \quad (2.5)$$

and the line (2) for the oxygen reaction:

$$E_r(H_2O|O_2) = 1{,}23 - 0{,}0591pH \sim -5.8 \text{ eV (at pH=0)} \quad (2.6)$$

According to the previously designated, formed holes in a semiconductor whose position of the valence zone are below the potential of the oxygen reaction will be theoretically capable of oxidizing water to oxygen. In the case of a semiconductor, whose position of the conductive zone is above the potential of the hydrogen reaction will be theoretically capable of generating photoelectrons to reduce hydrogen ion to molecular hydrogen. Unfortunately, due to the corrosion instability, a short lifetime of formed electron-hole pairs, there is a very small number of semiconductors that can satisfy the application in various photoelectrochemical reactions. The most important representatives of oxide metals are titanium dioxide and barium titanate, cadmium sulfide and lead sulfide.

2.2. Applications of the photoelectrochemical reactions

2.2.1. Photoelectrochemical cell

One of the earliest application of the photoelectrochemical cell was in the photo-water splitting reaction, performed by Fujishima and Honda [42], in the cell shown in Figure 2.7.

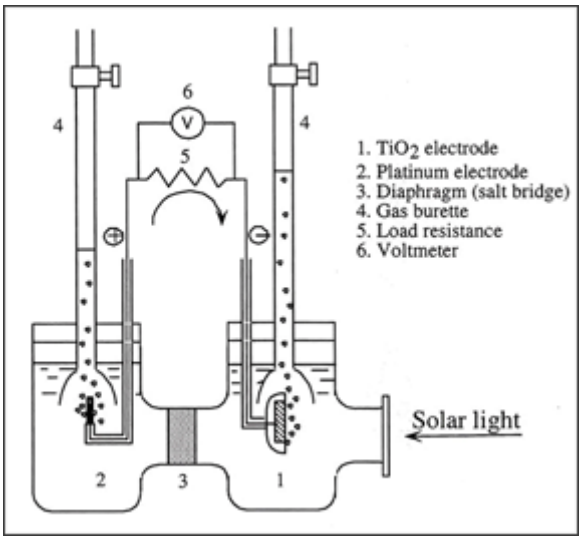

Figure 2.7. The erliest cell for photolitic spliting of watter [42].

However, under this conditions reactions are very slow, due huge overpotentials typically related with the photo anode. Consequently, in principle, an external bias (external power sources) should be applied. External bias also provides the necessary overvoltage on the metallic cathode required to sustain the current flow, and to increases the band banding in the semiconductor to maintain the charge separation rate. Through a typical photo-water splitting on the photoanode, generated holes oxidize water to oxygen or other oxygen containing species (OH^* radicals, H_2O_2 HO_2^-). Electrons produced via an external circuit are transported to metal cathode and involved in the hydrogen evolution reaction. If cell contained some organic matter (OM), holes can react with them in the reaction of oxidation, as schematically shown in Figure 2.8.

In the case of $C_xH_yO_z$-type organic compounds, oxidation potential will vary from one substance to the other. In addition, oxidation of such substances takes place by a series of steps, according to its complexity. For example, for ethanol the following oxidation scheme overcomes [43]:

ethanol → acetaldehyde → acetic acid → CO_2 + H_2O

Absorption of photons generates electrons and holes on the semiconductor S:

$$S + h\nu \rightarrow S(e^- + h^+) \qquad (2.7)$$

Most photogenerated electrons, which escape recombination, flow in the external circuit.

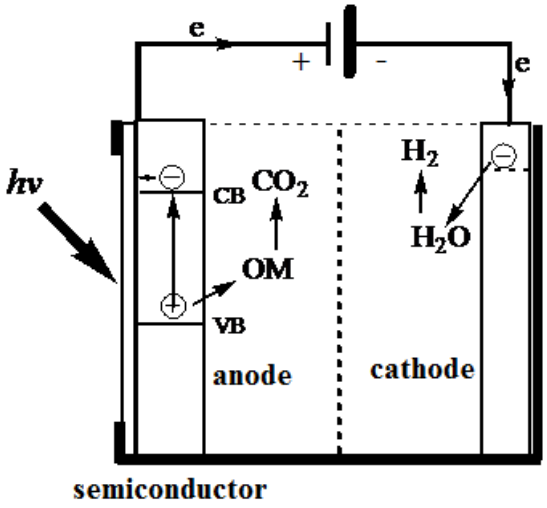

Figure. 2.8. Schematic representation of photoelectrochemical cell for simultaneous degradation of various organic waste (OM) and hydrogen production [35].

The photogenerated holes, which escape recombination, ract with the fuel or water by the following principal reaction schemes [43]. The fuel is represented by $C_xH_yO_z$-type compounds (alcohols, organic acids, carbohydrates *etc.*), since they are the best fuel both for electricity and hydrogen production. Depending on pH of the solution reactions are [43]:

- oxidation of organic compound occurring mainly at low pH:

$$C_xH_yO_z + (2x-z)H_2O + (4x+y-2z)h^+ \rightarrow xCO_2 + (4x+y-2z)H^+, \quad (2.8)$$

-oxidation occurring mainly at higher pH, via producing hydroxyl radicals, OH*:

$$OH^- + h^+ \rightarrow OH^* \quad (2.9a)$$

$$C_xH_yO_z + (4x+y-2z)OH^* \rightarrow xCO_2 + (2x+y-z)H_2O \quad (2.9b)$$

In the absence of fuel, water is oxidized with the produced holes. The following two reactions correspond to two pH extremes [43]:

$$2H_2O + 4h^+ \rightarrow O_2 + 4H^+ \qquad +1.23 \text{ V } \textit{vs.} \text{ SHE at pH} = 0 \quad (2.10a)$$

$$4OH^- + 4h^+ \rightarrow O_2 + 2H_2O \qquad +0.40 \text{ V } \textit{vs.} \text{ SHE at pH} = 14 \quad (2.10b)$$

2.2.2. The photoelectrochemical fuel cells

Important, but not well elaborated application of the photoelectrochemical reactions are in the photoelectrochemical fuel cells, which are still at the stage of laboratory testing and development [43,44,45,46,47,48,49]. The principle of work is similar to photoelectrochemical solar cells, which instead of regenerative electrolytes, usually used dissolves salts, bases or acids. If an electrolyte contains some pollutant or organic matter (OM), the anode reaction (oxidation) represents degradation of the given substance to carbon dioxide. If a cathodic reaction is the oxygen reduction reaction,

Figure 2.9a, such principles gives the principle of conventional fuel cell. However, if a cathodic reaction is the hydrogen ion reduction reaction, Figure 2.9b, simultaneously with anodic oxidation of pollutants, gaseous hydrogen can also be obtained. The schematic principle of the operation of such photoelectrochemical cells is given in Figure 2.9. As a consequence of the electron flow in both cases electric energy is generated.

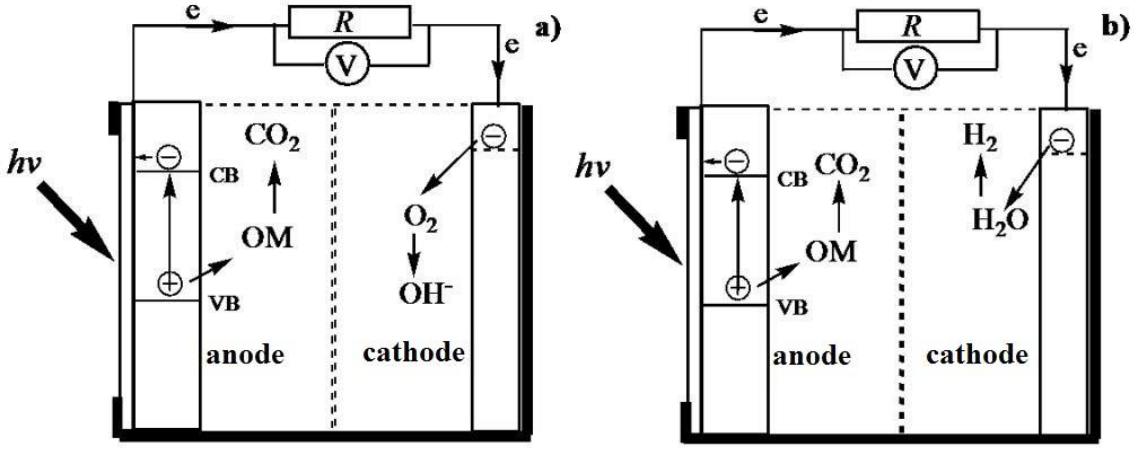

Figure 2.9. Schematic representation of the functioning of photoelectrochemical cells for simultaneous degradation of organic matter and electricity production [35].

Table 2.2 shows, as an example, the laboratory characteristics of the photoelectrochemical fuel cell in 0.1 M Na_2SO_4 with TiO_2 photonode and cathode made with platinum foil, using various organic compounds as fuel [50].

Table 2.2. Laboratory characteristics of the photoelectrochemical fuel cell in 0.1 M Na_2SO_4 with TiO_2 photoanode and platinum film and cathode [50], U_{oc}-open circuit voltage, j_{sc}-short circuit current.

Solution (conc., M)	**Solvent (pH)**	U_{oc} (V)	j_{sc} (mA cm^{-2})
Methanol	/	0.54	0.8
Methanol (50 vol.%)	Water (/)	0.44	0.76
Ethanol	/	0.49	0.52
Amino acids (0.5)	Water (5)	0.64	0.50
Urea	Water (5)	0.60	0.30
Ammonia (10)	Water (12)	0.84	0.53
Acetic acid 2%	Water (/)	0.94	0.47
Glycerin (0.5)	Water (5)	0.76	0.45
Glutaminic acid (0.5)	Water (1)	0.9	0.64
Tyrosine	Water (13)	0.86	0.43

Solution (conc., M)	Solvent (pH)	U_{oc} (V)	j_{sc} (mA cm^{-2})
Phenylalanine (0.5)	Water (13)	0.90	0.61
Agar (0.2 vol.%)	Water (5)	0.60	0.12
Gelatin (2 vol.%)	Water (1)	0.64	0.23
Collagen (3mg ml^{-1})	Water (1)	0.62	0.16
Cellulosic sulfate (2 vol.%)	Water (/)	0.56	0.29
Lignosulfonic acid (0.5 vol.%)	Water (/)	0.57	0.02
Polyethylene glycol (2 vol.%)	Water (5)	0.60	0.28

2.3. Urea as an energy carrier

The production of electricity or hydrogen and electricity from the wastewaters or residues of different industrial processes, is today of enormous interest due environmental issues and needs for alternative energy sources [51]. Urea, also known as carbamide, which molecular structure shown in Figure 2.10, is considered as an ideal energy carrier [52].

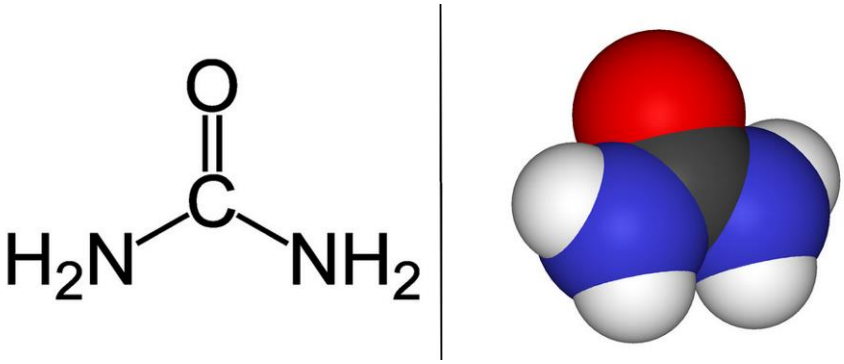

Figure 2.10. Structural formula and model of the urea.

The yearly production of urea for the manufacture of the fertilizers and other chemicals, exceeds hundred millions of tons worldwide [52]. Also, urea is a main component of the human or animal urine, in the concentration range from 0.15 M to 0.4 M, which annual production exceeds many times than market demand, of 0.5 Mt per day [52,53]. Under certain conditions in the nature, urea can decompose to nitrate or nitrite, which is a high environmental risk due possible contaminations of the ground water [54,55]. Thus, the wastewaters containing urea should be purified using different removal processes [55].

In principle, there are two methods for the usage of the urea as energy carriers, hydrogen production via electrolysis of water containing urea [53,56] and as a fuel in the fuel cells [45,57,58].

Theoretically, during the electrolysis of water containing urea under strong alkaline conditions, at pH=14, the following reactions occurred:

at the cathode:

$$2H_2O + 2e \rightleftarrows H_2 + 2OH^- \quad (E_r^o = -0.84\ V) \tag{2.11}$$

and at the anode [53]:

$$CO(NH_2)_2 + 6OH^- \rightleftarrows N_2 + CO_2 + 5H_2O + 6e \quad (E_r^o = -0.46\ V) \tag{2.12}$$

Hereafter, the theoretical decomposition voltage for such cell under standard conditions is as low as 0.38 V. On the other hand, in the urea based fuel cell the following reaction occurred:

at the anode:

$$CO(NH_2)_2 + 6OH^- \rightleftarrows N_2 + CO_2 + 5H_2O + 6e \quad (E_r^o = -0.46\ V) \tag{2.13}$$

and at the cathode:

$$O_2 + 2H_2O + 4e \rightleftarrows 4OH^- \quad (E_r^o = 0.40\ V) \tag{2.14}$$

with the theoretical open circuit voltage under standard conditions of 0.86 V. Because the urea is a very strong catalytic poison for the platinum as the most common catalysts, such reactions are technically possible only in the highly alkaline media to prevent intense corrosion, of for example nickel-cobalt based catalyst [58]. In addition, the one product of the urea degradation is carbon dioxide, which react with used hydroxide electrolyte lowering the efficiency of the processes and pH.

Consequently, the different approaches should be considered for the use of wastewater containing urea as an energy carriers, with typical pH near neutral, for example: in microbial fuel cells [59], or in different photoelectrochemical cells [51,60, 61,62]. In the photoelectrochemical cell as a most common photoanode the titanium dioxide nanotube is typically used [63,64,65,66]. Unfortunately, the band gap of titanium dioxide is ~3.2 eV permitting the absorption of only in the UV light region, which presents a small fraction of ~5% of total Sun irradiance. To improve absorption in a visible range of the Sun spectra, many different surface modification of TiO_2 were examined [7,67,68]. Among others, iron oxide, specifically hematite, α-Fe_2O_3, is the topic of intense investigations [13,23,63,64,69, 70, 71].

2.4. Titanium dioxide as photocatalytic materials

Different metal oxides and sulfides are a theme of extensive investigations in recent years, predominantly for their uses as catalysts in environmental remediation through photo-induced degradations of organic water pollutants [72]. Among different catalysts based on metal oxide, TiO_2 is of particular importance due to its exclusive properties, such as remarkable chemical stability, chemical inertness, large band gap, high refractive index, biocompatibility, non-toxicity, etc.

Titanium dioxide with a chemical formula TiO_2 was first discovered in 1791 from mineral ilmenite. It is also known as titanium (IV) oxide, titania, titanium white or pigment white 6 in building paints, and E171 in food coloring. The titanium oxide occurs in nature as brookite, anatase and rutile. It is commercially manufactured as white pigments since 1916 [73].

As discussed in their review by Lan et al. [73], the photo activity of TiO_2 was first observed in 1929 when it was used as white pigments for buildings. It was found that the TiO_2 building pigments was sun-bleached under long solar irradiation. First scientific report on TiO_2 photoactivity was published in 1932–1934 [73]. It was reported that NH_3 and ammonium salts were photo-oxidized to nitrites when exposed to sunlight in presence of TiO_2 even though the results were questionable. The reliable report on photocatalytic action of TiO_2 was first published in 1938 on the photo-bleaching of

dyes, named photosensitizer at that time. It was reported that UV light absorption produced some active oxygen contained species on TiO_2 surfaces, triggering photobleaching of dyes. The TiO_2 based photocatalyst was first designated in 1956. The oxidation of organic solvents and the formation of H_2O_2 were observed under an UV illumination with a mercury lamp under ambient conditions. The water photolysis was confirmed for the first time in 1972 on TiO_2 semiconductors [42]. Water was splited in oxygen on the TiO_2 photoanode and hydrogen on the platinum black cathode.

2.4.1. Structure and the properties of titanium dioxide

Titanium oxide has many polymorphs [74]. The well-known phases of titanium dioxide are naturally occurred rutile (discovered in 1803), anatase (discovered in 1801) and brookite (discovered in 1825), named after their reddish color, extended crystallographic shape, and a mineralogist, respectively. Different structures of TiO_2 is shown in Figure 2.11 [74]. The metastable forms, anatase and brookite phases can irreversibly convert to stable rutile upon heating.

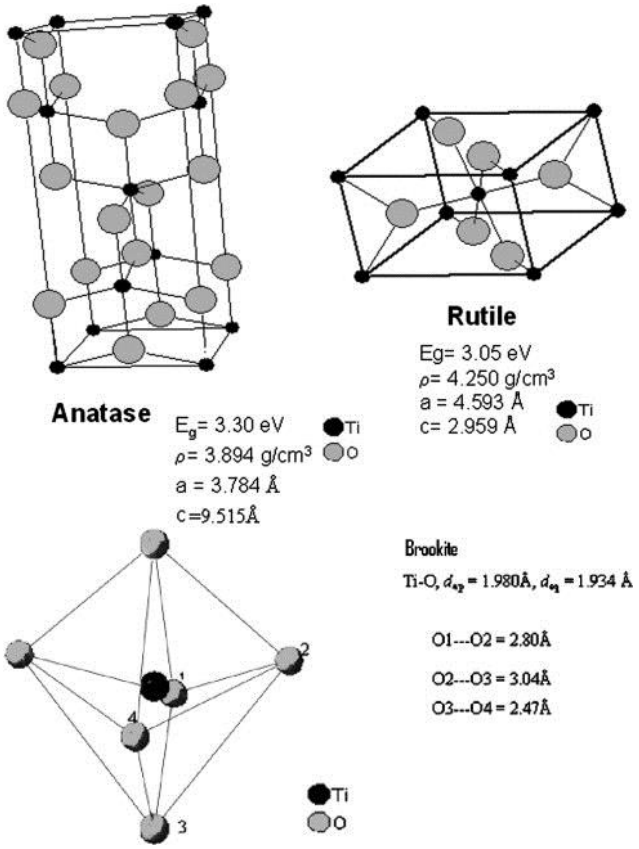

Figure 2.11. Different structures of TiO_2 [74].

Some physical properties of rutile and anatase are summarized in table 2.3 [75].

Table 2.3. Properties of anatase and rutile [75].

Property	Anatase	Rutile
Crystal structure	Tetragonal	Tetragonal
Atoms per unit cell (Z)	4	2
Lattice parameters (nm)	a = 0.3785	a = 0.4594
	c = 0.9514	c = 0.29589
Unit cell volume (nm^3)[a]	0.1363	0.0624
Density (kg m^{-3})	3894	4250
Calculated indirect band gap		
(eV)	3.23–3.59	3.02–3.24
(nm)	345.4–383.9	382.7–410.1
Experimental band gap		
(eV)	~3.2	~3.0
(nm)	~387	~413
Refractive index	2.54, 2.49	2.79, 2.903
Solubility in HF	Soluble	Insoluble
Solubility in H_2O	Insoluble	Insoluble
Hardness (Mohs)	5.5–6	6–6.5
Bulk modulus (GPa)	183	206

The anatase possesses an energy band gap of 3.2 eV with an absorption edge at 387 nm that lies in the near-UV range. The rutile has a narrower energy band gap of ~3.0 eV with an absorption edge in the near-visible range at 413 nm. The typical UV-vis spectra are shown in Figure 2.12 [76].

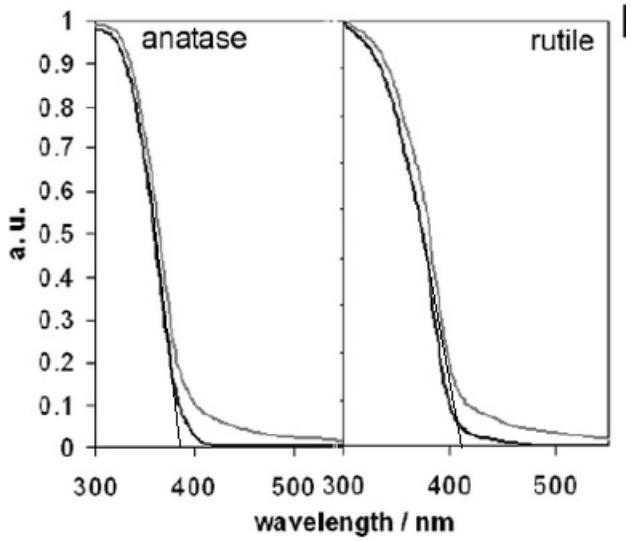

Figure 2.12. UV/vis absorption spectra for anatase and rutile [76].

Both TiO_2 structures (anatase and rutile) are photocatalytically active. The structure of the TiO_2 band gap at pH = 7 is shown in Figure 2.13 [77].

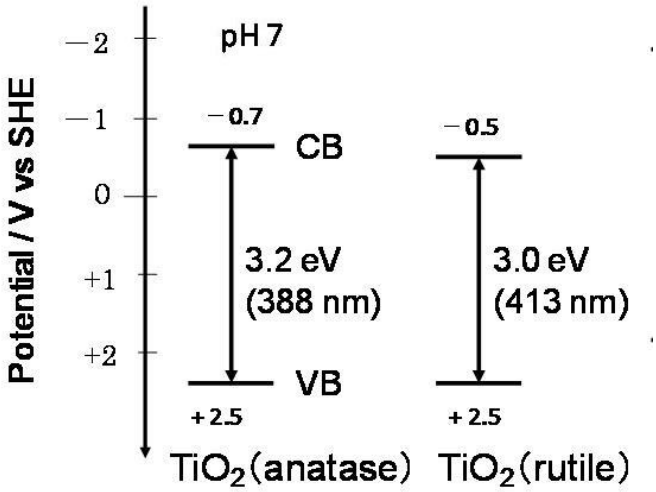

Figure 2.13. The structure of the band gap for anatase and rutile at pH =7 [77].

It can be seen that both structures has the position of the valence band at +2.5 V, which permits that formed holes can oxidize water to oxygen, and many organic materials. In principle, the position of conducting band will allow hydrogen evolution reaction to occur, but due different kinetics limitations in practice, this reaction is very slow.

After a semiconductor is immersed in an aqueous solution, H^+ and OH^- ions in the solution will continuously adsorb and desorb from the surface [78]. A dynamic equilibrium will be established, which can be described by the following protonation and deprotonation reactions:

$$M - OH \underset{}{\overset{k_a}{\rightleftharpoons}} MO^- + H^+_{aq}$$

$$M - OH + H^+_{aq} \underset{}{\overset{k_b}{\rightleftharpoons}} M - OH^+_2 .$$

These reactions changes provoke the shifts in the positions of conducting and valence bands with pH. The positions with respect to pH = 0, moves with pH according to the following equations:

$$E_{VB} \approx +2.78 - 0.0591\ pH \quad (2.15)$$

and:

$$E_{CB} \approx -0.29 - 0.0591\ pH;\ V\ vs.\ SHE \quad \text{for anatase} \quad (2.16)$$

$$E_{CB} \approx -0.09 - 0.0591\ pH;\ V\ vs.\ SHE \quad \text{for rutile} \quad (2.17)$$

When TiO_2 is exposed to UV light with a wavelength of 280–400 nm (4.43-3.10 eV), the UV light will be absorbed by TiO_2 and an electron is raised up from the valence band to the conduction band of TiO_2, leaving behind a hole in the valence band, as shown in Figure 2.14, to form electron–hole pairs [75]. Generally, it is accepted that:

$$TiO_2 + h\nu \rightarrow e^-(CB) + h^+(VB)$$

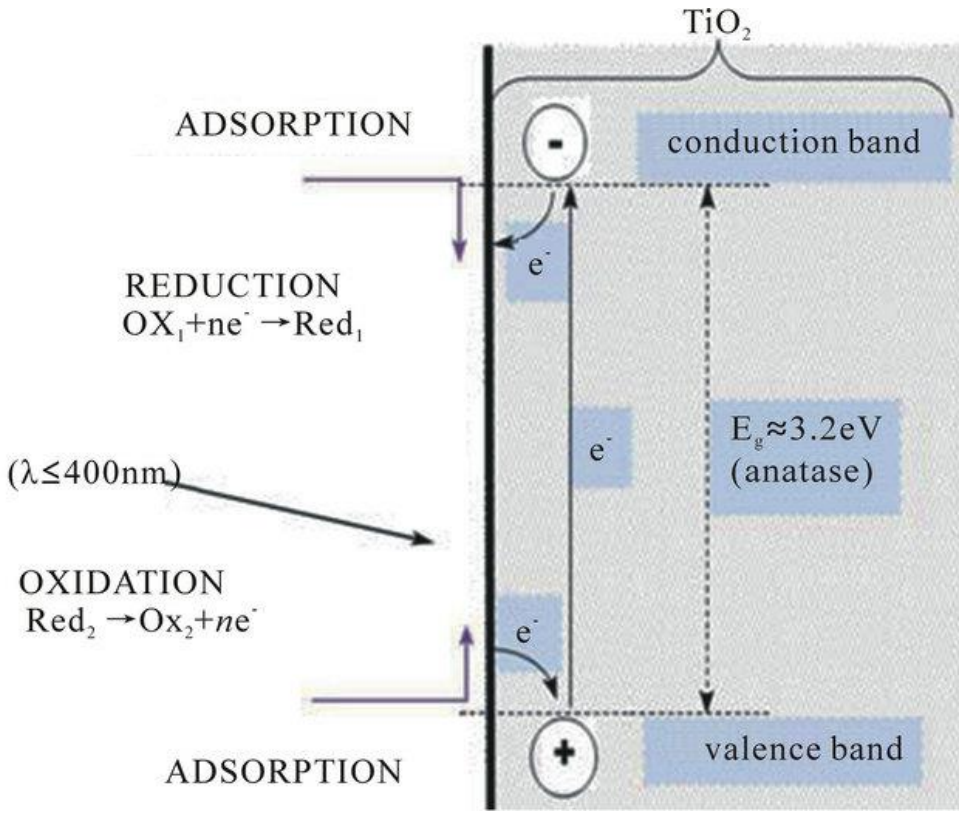

Figure 2.14. Schematic illustration of photo-generation of charge carriers in a photocatalytic TiO_2 [75]. A valence band electron hole is represented by "+" and a conduction band electron is represented by "–".

In comparison with the bulk TiO_2 materials, the different TiO_2 nanomaterials attracted much more attentions. Because of high surface to volume ratio, TiO_2 nanostructures provide increased surface area at which photo-reactions could occur. Moreover, nanomaterials improved light absorption rate, increase near surface photo-induced charge carrier density, improving the photo-reduction rate, and resulting in advanced photoactivity. At the same time, the high surface to volume ratio of the nanomaterials increase the surface absorption of OH^- and H_2O, increasing the photocatalytic reaction rate. There is a large numbers of titanium dioxide morphology, as can be seen from the Figures 2.15-2.17 [79]. Numerous methods for the synthesis of TiO_2 nanostructures are considered and well elaborated in the literature. This includes a sol-gel procedure [80], microwave radiation [81], hydrothermal treatment [82], pattern-synthesis [83], and electrochemical oxidation [84].

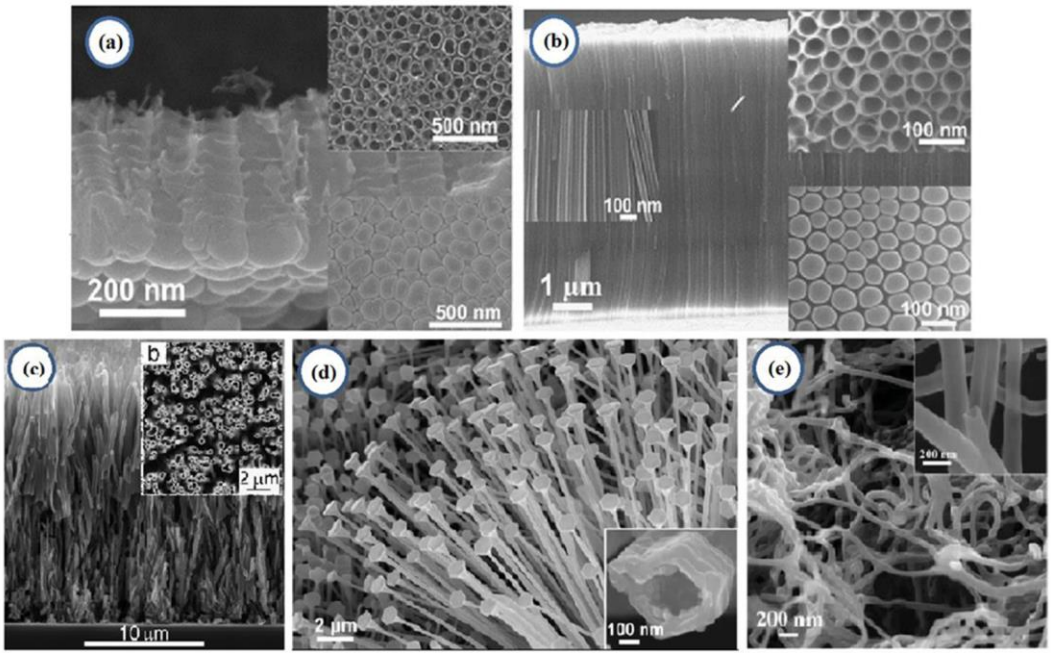

Figure 2.15. TiO_2 tubular nanostructures:
(a) Short TiO_2 nanotube arrays from anodization of Ti. (b) Long TiO_2 nanotube arrays from anodization of Ti. (c) TiO_2 nanotubes from a ZnO template (LPD process). (d) TiO_2 nanotubes from a ZnO template ($TiCl_4$ vapor pulses). (e) Fibrous TiO_2 nanotube network from a cellulose nanofiber template (ALD process) [79].

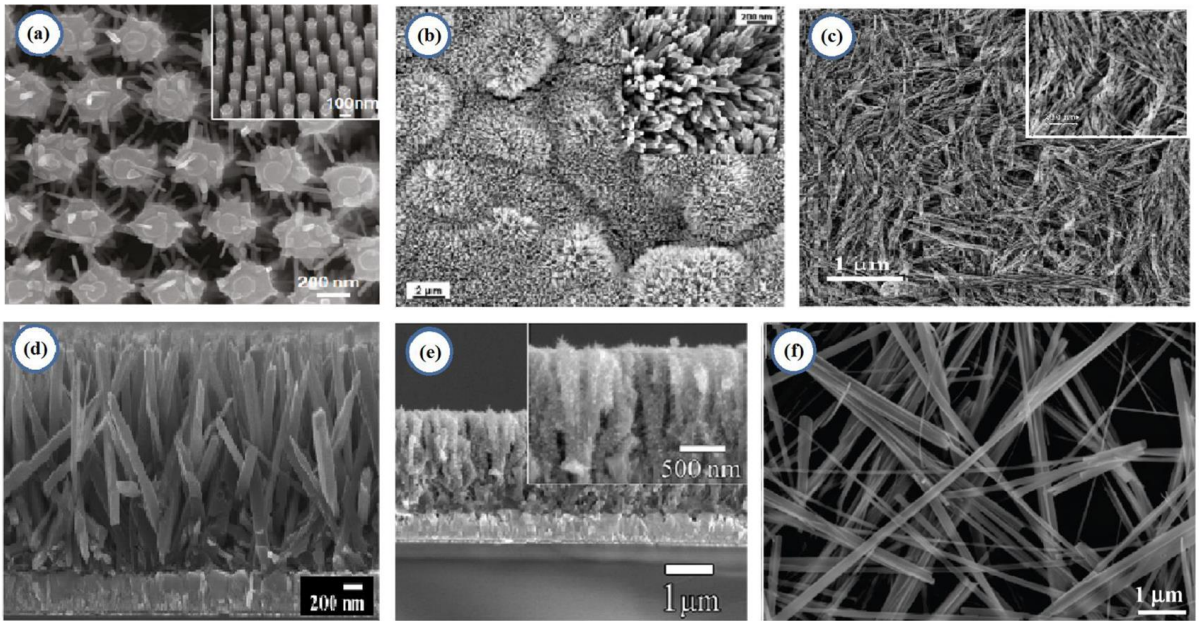

Figure 2.16. (a) TiO_2 nanobelts. (b) TiO_2 nanorods. (c) TiO_2 nanowires. (d) TiO_2 nanorods. (e) Branched TiO_2 nanorods. (f) Hierarchical TiO_2 nanowires [79].

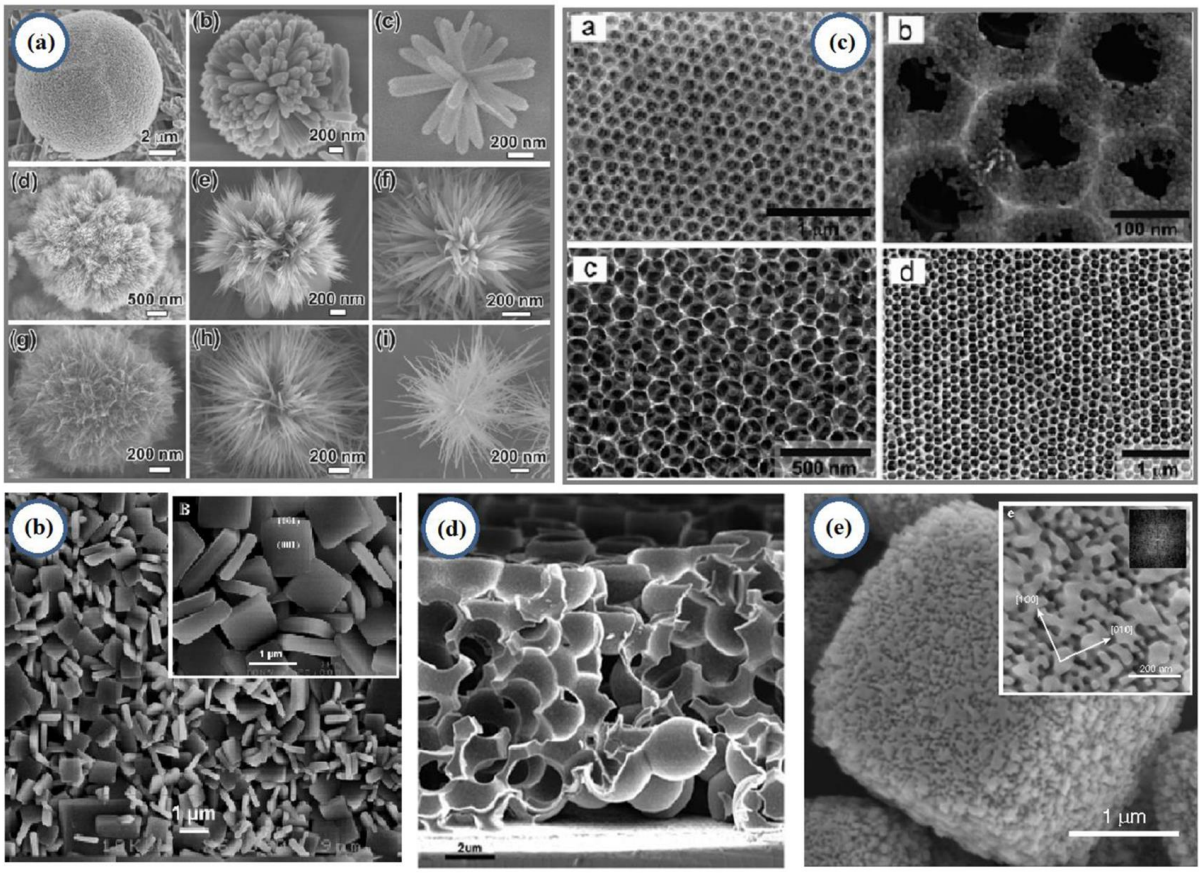

Figure 2.17. (a) 3D dendritic TiO_2 nanostructures. (b) TiO_2 nanosheets. (c) TiO_2 opal. (d) 3D TiO_2 opal. (e) mesoporous TiO_2 single crystals [79].

2.4.2. Titanium dioxide nanotubes

Among different methods for producing titanium dioxide nanostructures, the electrochemical method for fabricating titanium dioxide nanotubes (NT's) are proved to be the simplest and most effective. This method has recently attracted more attention. In essence, TiO_2 nanotubes are formed on the anode surface of Ti film by anodic oxidation in a suitable electrolyte. Several types of inorganic or organic solutions containing fluoride-ions can be used as electrolytes. For example, H_2SO_4 / HF [85,86], H_3PO_4 / HF [87], ethylene glycol / HF [88], glycerol / NH_4F [89,90], ethylene glycol / NH_4F [89,91], NaH_2SO_4 / HF [92] and Na_2SO_4 / NaF [93]. However, it is proved that the most suitable electrolyte is on the basis of H_3PO_4 / HF. In this process, the size of TiO_2 - NT's can be controlled by adjusting the parameters of the electrochemical processing, and above all by the applied voltage. [87,89]

Bauer et al. [87] give one of the best report about the conditions of titanium dioxide nanotubes formation in phosphoric acid - hydrofluoric acid based electrolytes.

In Figure 2.18 characteristic SEM images of the surface morphology on of TiO_2 layers obtained after anodization in 1 M H_3PO_4 with different concentrations of HF at a voltage of 10 V for 2 h are shown [87]. It is obvious that the amount of HF significantly affects the process of pore formation and morphology of the porous surface. Anodization at the concentration of fluoride ions <0.1 mass% results in the formation of a compact oxide layer as shown in Figure 2.18a). At higher concentrations of fluoride (0.1-0.4 mass%), the structures of self-assembled nanotubes can be seen, with a pore diameter of ~ 50 nm, shown in Figure 2.18b). With the addition of 0.5% HF, nanoparticles degrade, as shown in Figure 2.18c). From this results it can be concluded that the optimal conditions for self-forming pore formation is at a concentration of 0.3% by weight of HF [87].

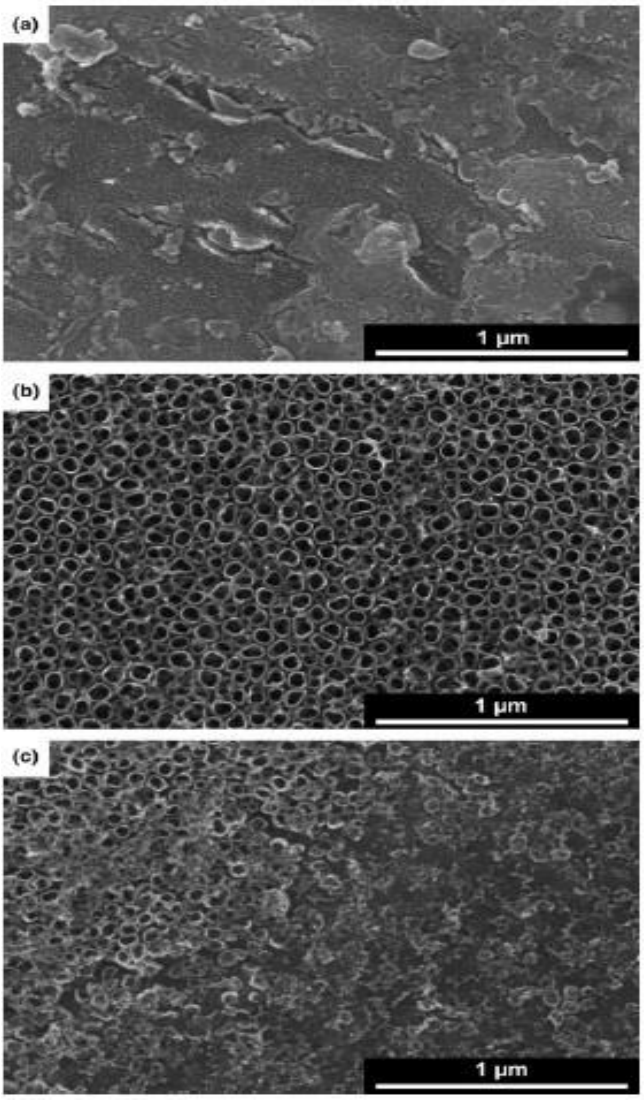

Figure 2.18. SEM images of TiO2 layers formed at 10V for 2h in 1M H_3PO_4 with different additions HF: (a) 0.025 wt%, (b) 0.3 wt%, (s) 0.5 wt% [87].

Thus, all the following experiments were carried out in 1 M H_3PO_4 + 0.3% by weight of HF. For this electrolyte, the influence of various applied potentials on the anodized surface in the range 1 V to 25 V was studied (Figure 2.19). The inserts show the appropriate vertical cross-sections [87]. For potentials greater than 25 V, the anodic layers no longer exhibit self-organized morphology. It is especially important that self-organized structures are obtained even at very low potentials (1 V). Potentials lower than 1 V cause a more or less uniform titanium corrosion due to the fact that these voltages are in the active metal dissolution region. The morphology of tubes formed on 1 V shows the structure of the grid. These tubes are interconnected, while nanotubes

formed at 25 V seem to be isolated from those surrounding them. In principle, there seems to be a tendency to achieve greater separation of high-voltage tubes. However, the results clearly indicate that the voltage determines the diameter of the tubes in the TiO_2 nanotube layers. It is also shown that the H_3PO_4 / HF system provides a high degree of nanometer modification geometry [87].

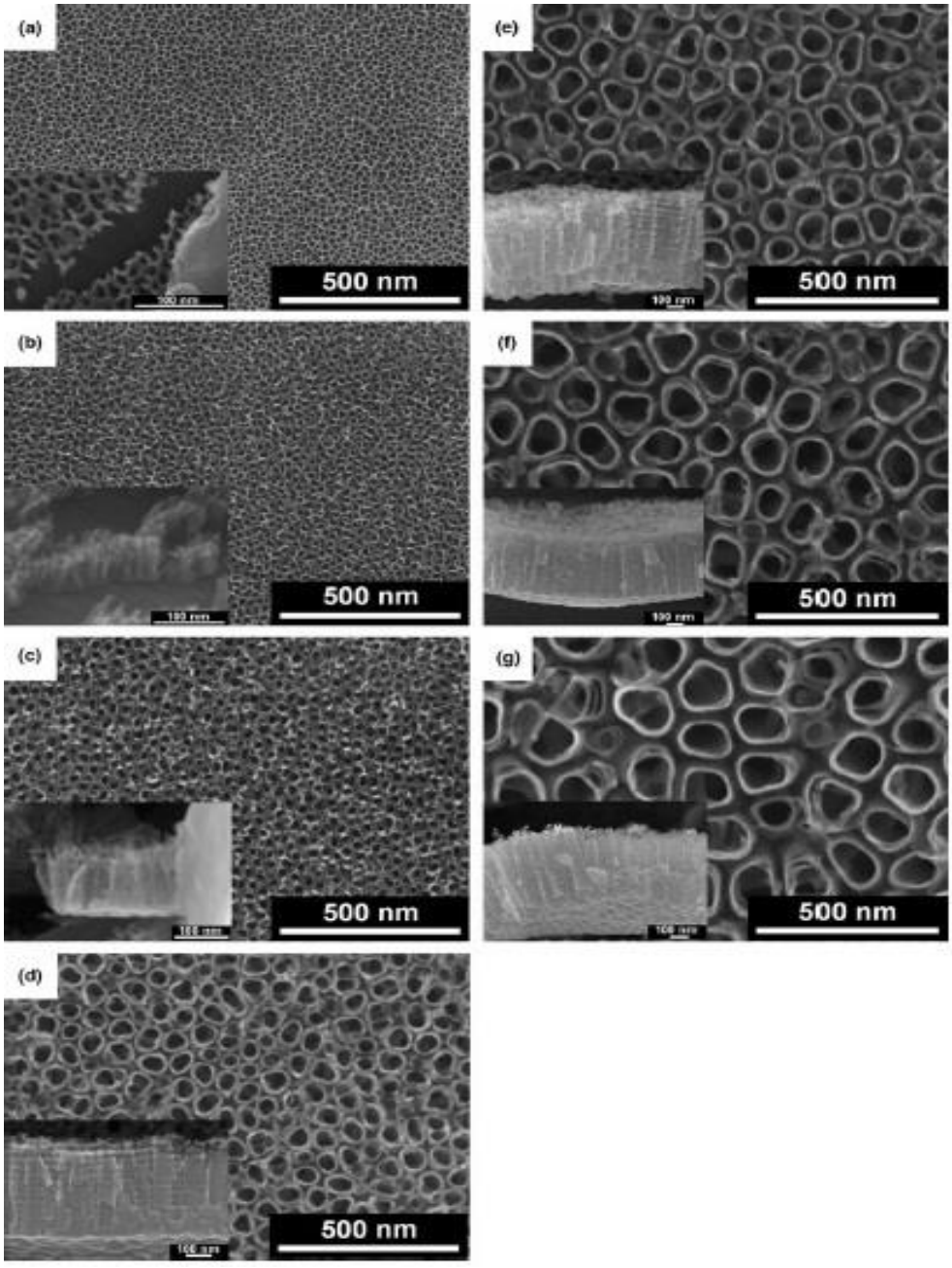

Figure 2.19. SEM images of TiO_2 nanotubes (cross-section and top view) formed in 1 M H_3PO_4 + 0.3% HF to: (a) 1 V, (b) 2.5 V, (c) 5 V, (d) 10 V, (e) 15 V, (f) 20 V and (g) 25 V for 1h [87].

The nanotube diameters obtained under the conditions of self-organization of the tubular layers are dependent on the potential. The results for the diameter and length of the tube are given in Figure 2.20. Obviously, the diameter and length of the tube depend linearly on the voltage. The tube diameters range from 15 to 120 nm, and the tube length is from 20 nm to ~1 μm.

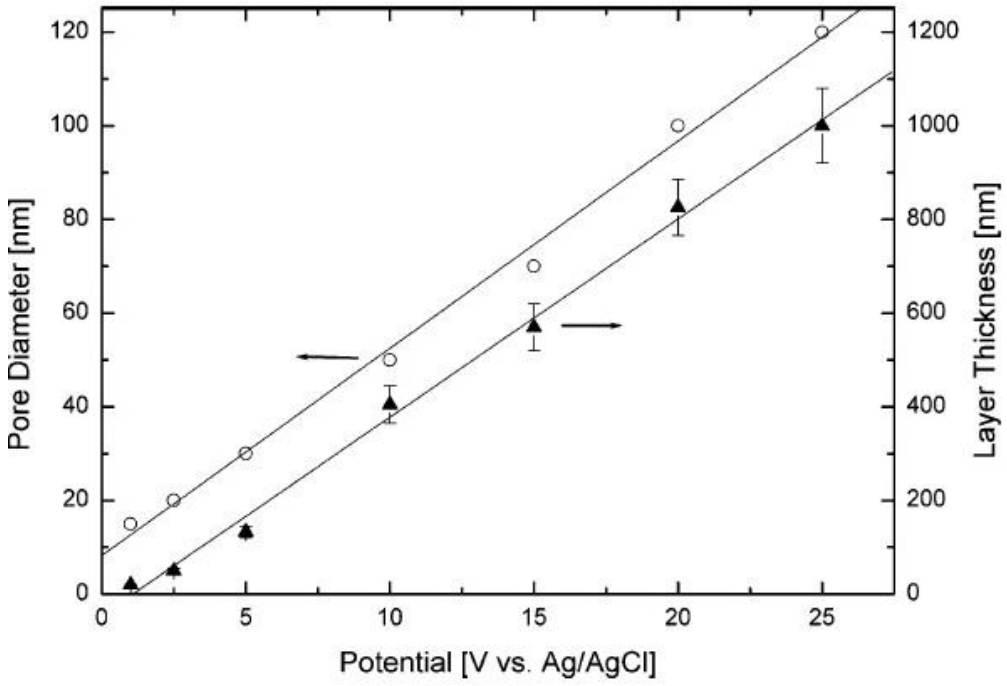

Figure 2.20. Diameters and thicknesses of nanotube layers formed in 1 M H_3PO_4 + 0.3% HF% on different potentials [87].

2.4.2.1. Mechanism of TiO_2 nanotubes formation

Titanium nanotube can be easily prepared by the anodization of metallic titanium in a suitable electrolyte, in an electrochemical cell shown in a Figure 2.21. The cell should be made from plastic materials to avoid interaction of fluoride ions with glass. The cell consist a one or more cathode, usually from an inert metal like Pt. The applied voltage, from external power supply, depends on electrolyte and can vary from few volts to few hundred volts for organic based electrolytes.

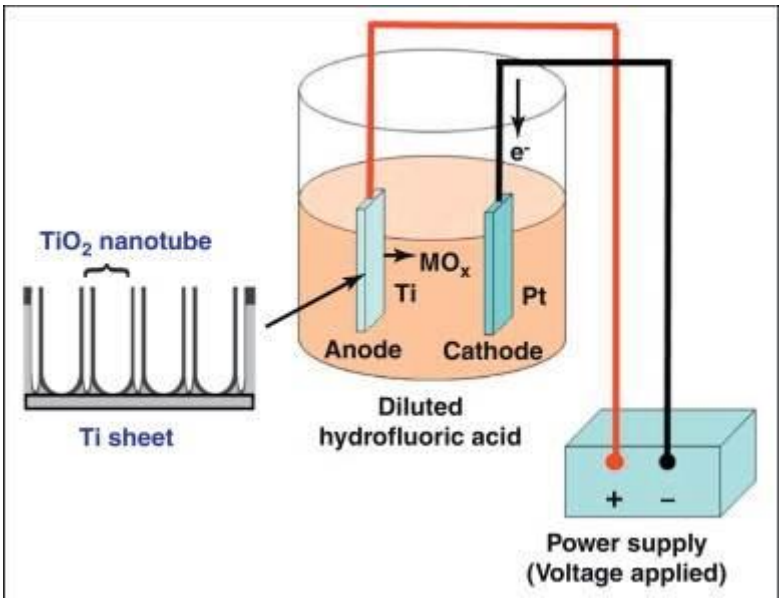

Figure 2.21. Principles of titanium anodization.

It is well established in the literature [94] that the formation and growth of nanotubes in fluoride containing electrolytes depends basically on two processes, as schematically shown in Figure 2.22. 1. the field assisted oxidation of titanium at the metal/oxide interface (reactions 2.18 and 2.19, Figure 2.22a). 2. the field assisted chemical dissolution within the tube at TiO_2/electrolyte interface by producing water soluble complexes which controls the diameter and wall thickness of nanotubes (reactions 2.20 and 2.21, Figure 2.22b). The formation and growth of nanotubes depends on the competition between mechanisms (1) and (2) as shown in Figure 2.22.

$$Ti \rightarrow Ti^{4+} + 4e^{-} \quad (2.18)$$

$$Ti^{4+} + 2H_2O \rightarrow TiO_2 + 4H^{+} \quad (2.19)$$

$$Ti^{4+} + 6F^{-} \rightarrow [TiF_6]^{2-} \quad (2.20)$$

$$TiO_2 + 6F^{-} + 4H^{+} \rightarrow [TiF_6]^{2-} + 2H_2O \quad (2.21)$$

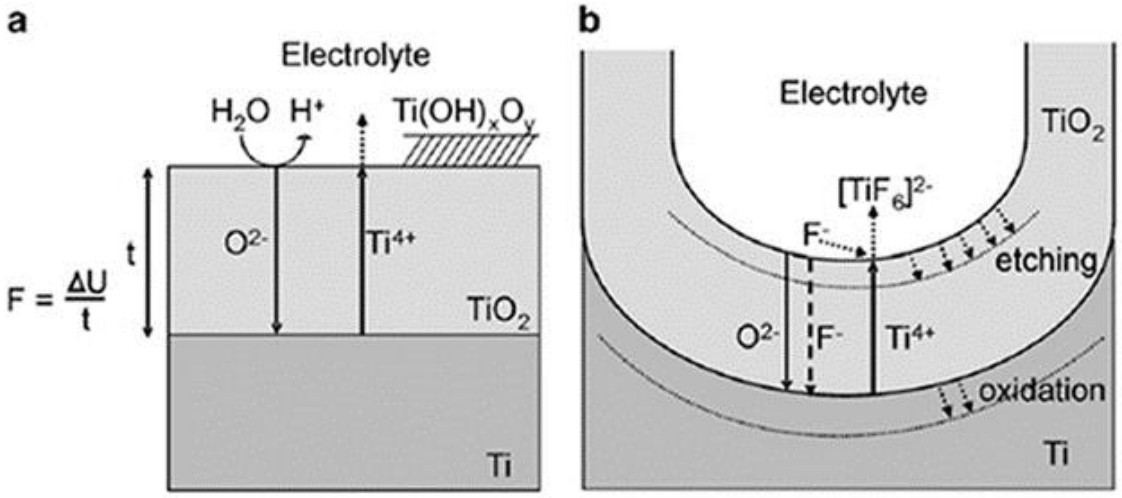

Figure 2.22. Schematic presentation of the mechanism of TiO_2 nanotubular structure formation in the fluoride-containing electrolyte [94].

In Figure 2.23, the growth of the nanotube over the time is represented. Sequences contains the TiO_2 layer formation, pit initiations, followed by formations of nanopores and nanotubes.

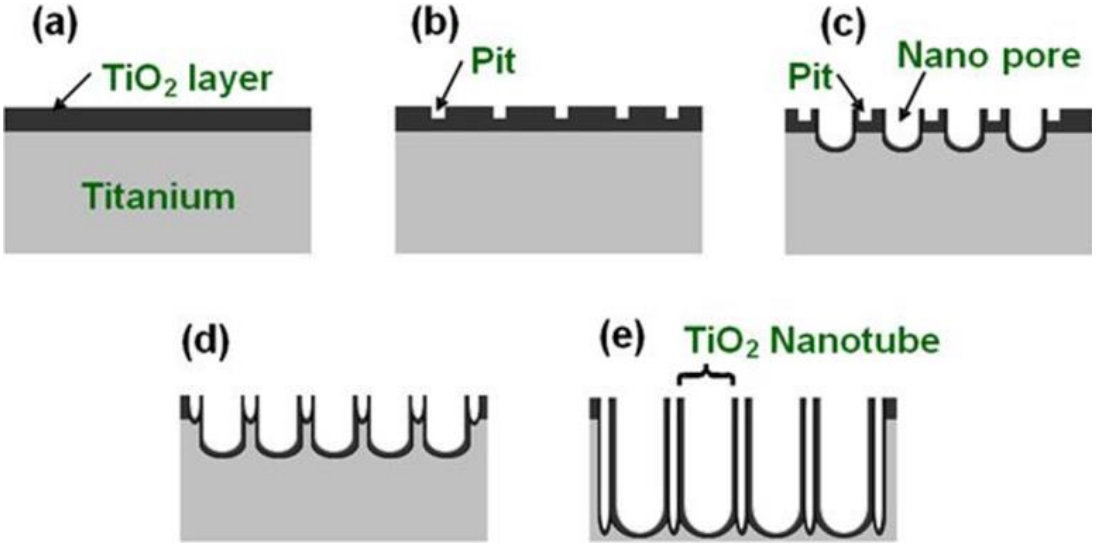

Figure 2.23. Schematic representation of the growth of the TiO_2 nanotube over the time.

2.4.3. Photoelectrochemical behavior of the titanium dioxide

As mentioned above, there is various synthesis routes for fabricating titanium dioxide. Nevertheless, the performances of titanium dioxide in specific device applications are found to be strongly dependent on the synthetic methods used for its production. The majority of such synthetic procedures rely on the hydrolysis of suitable precursors and often produce an amorphous solid, generally referred as the "amorphous" titanium oxide beside the crystalline titania [95].

Figure 2.24, shows the comparisons of as synthetized thin TiO_2 film and sol-gel TiO_2. [96]. It can be seen that as synthetised –amorphous samples shows relativelly small photocurrent in the range of 10 to 50 μA cm^{-2}.

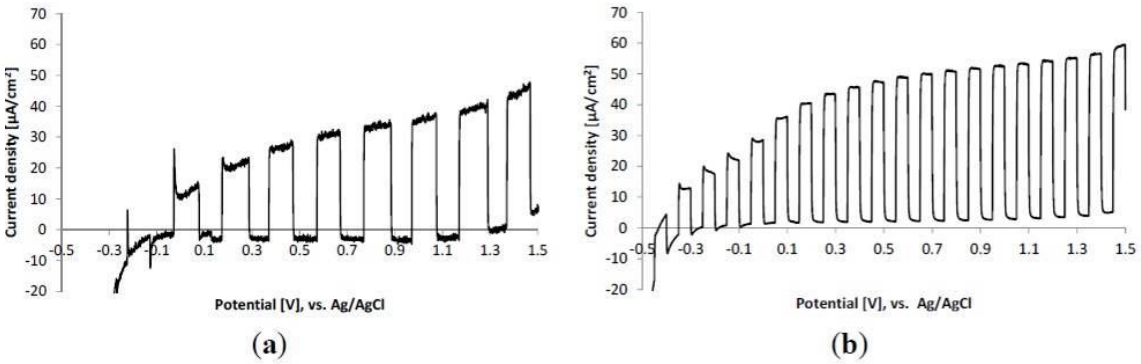

Figure 2.24. Polarization curves for as synthetized samples under pulsating illumination: (a) thin TiO_2 film; (b) sol-gel TiO_2 thin film for wavelength of 365 nm (1.46 mW cm^{-2}), electrolyte 0.1 M Na_2SO_4, sweep rate 5mVs^{-1} [96].

As presented by Lim et al. [97], crystalline nature and stability of the crystalline phase present in nanotubes can be greatly influence their photoelectrochemical response. Consequently, authors measured the phototransients of the as prepared and 500^oC calcinated nanotubes at 1 V versus Ag/AgCl with a ten-seconds light pulse, and results are shown in Figure 2.25. The informations about the electron transport in nanotubes might be revealed from presented phototransients measurement. Relativelly slow upsurge in the photoresponse to a very low photocurrent with the magnitude of about 2 μA cm^{-2} for as-anodized nanotubes, Figure 2.25a, indicates the presence of a high number of defects which can act as traps and recombination centers for the

photogenerated charge carriers. Low photoresponse in as synthetized nanotubes is originated from the tube bottom as photogenerated charge carriers in the tube walls recombine at defects before they reach the tube bottom. Significant improvement in photoresponse, fastlly reaching photocurent of 40 µA cm^{-2}, is observed when nanotubes is exposed to the calcination at 500ºC (Figure 2.25b). This behaviour is explained to the lose of trap filling phenomenon and transformations of the amorphous nanotubes structure to the crystalline anatase or rutile phase [97]. Separately from the enhancement of photoresponse for calcined nanotubes, different phototransient shapes is observed also suggesting that a different electron driving mechanism is involved.

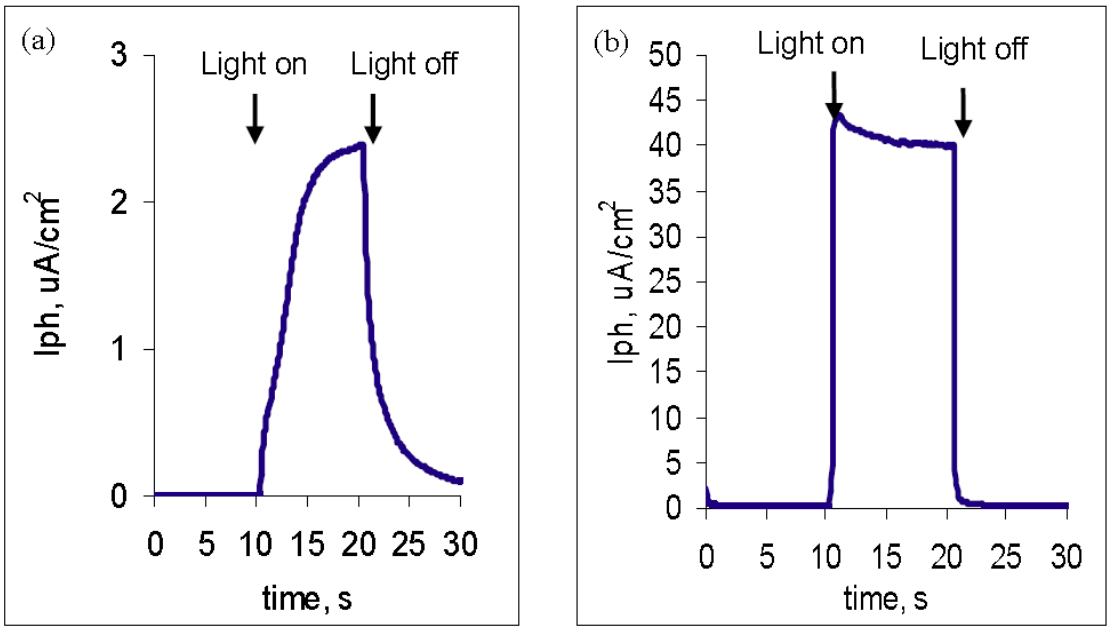

Figure 2.25. Phototransients measurement at 1 V versus Ag/AgCl with 10 s light pulse for a) as-anodized nanotubes and (b) nanotubes calcined at 500 ºC for 2h in open air. Phototransients measurement was done using 10 ppm methyl orange solution in 0.1 M KCl as supporting electrolyte [97].

Ghicov et al. [98], investigated different thermal treatment of nanotube layers formed in 1M H_3PO_4 + 1M NaOH + 0.5 wt% HF, and in all cases the improvment in photo response are observed, as can be seen in Figure 2.26. The best photoresponce is obtained after annealing at 450 °C for 1 s in air.

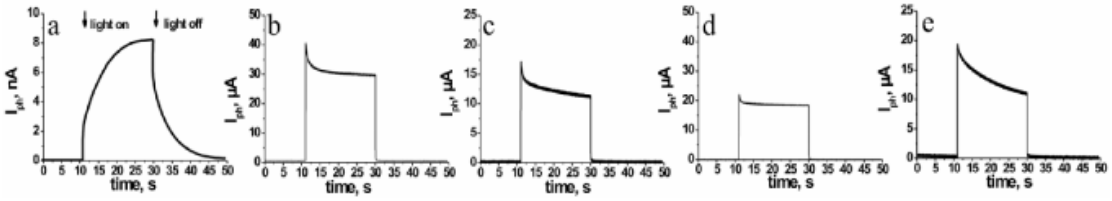

Figure 2.26. Curren phototransient with the light wavelength 350 nm and duration pulse of 20 s at 500 mV vs. Ag/AgCl applied bias of the "as prepared" TiO_2 nanotube layer (a), after annealing at 450 °C for 1 s in air (b), in dry Ar (c), extended annealing at 450 °C for 1 h in air (d) and in dry Ar (e) [98].

2.5. Iron oxide as photocatalytic materials

There is a meny varied forms of the iron oxides due different oxidation states of iron and possibility to forms a mixed nonstochiometric structures [99, 100,101].
Depending on the oxidation states iron oxide can be divided to:

a) Oxide of Fe(II):

FeO: iron(II) oxide, **wüstite**

b) Mixed oxides of Fe(II) and Fe(III):

Fe_3O_4: Iron(II,III) oxide, **magnetite**

c) Oxide of Fe(III) or Fe_2O_3: iron(III) oxide

α-Fe_2O_3: alpha phase, **hematite**

β-Fe_2O_3: beta phase

γ-Fe_2O_3: gamma phase, **maghemite**

ε-Fe_2O_3: epsilon phase

Iron(III) oxide or ferric oxide is the inorganic compound with the formula Fe_2O_3. It is one of the three main oxides of iron, the other two being iron(II) oxide (FeO), which is rare, and mixed iron(II,III) oxide (Fe_3O_4) that also occurs as the mineral magnetite. As the mineral known as hematite, Fe_2O_3 is the main source of iron for the steel industry. Fe_2O_3 is ferromagnetic, dark red, and readily attacked by acids. Iron(III) oxide is often called rust, and to some extent this label is useful, because rust shares

several properties and has a similar composition. To a chemist, rust is considered an ill-defined material, described as hydrated ferric oxide [99,100].

Fe_2O_3 can be obtained in various polymorphs. In the main ones, α and γ, iron adopts octahedral coordination geometry. Namely, each iron center is bound to six oxygen ligands [100].

Alpha phase

α-Fe_2O_3 has the rhombohedral, corundum (α-Al_2O_3) structure and is the most common form. It occurs naturally as the mineral hematite that is mined as the main ore of iron. It is antiferromagnetic below ~260 K (Morin transition temperature), and exhibits weak ferromagnetism between 260 K and the Néel temperature, 950 K. It is easy to prepare using both thermal decomposition and precipitation in the liquid phase. Its magnetic properties are dependent on many factors, e.g. pressure, particle size, and magnetic field intensity [100,101].

Gamma phase

γ-Fe_2O_3 has a cubic structure. It is metastable and converted from the alpha phase at high temperatures. It occurs naturally as the mineral maghemite. It is ferromagnetic and finds application in recording tapes, although ultrafine particles smaller than 10 nanometers are superparamagnetic. It can be prepared by thermal dehydratation of gamma iron(III) oxide-hydroxide, careful oxidation of iron(II,III) oxide. Another method involves the careful oxidation of Fe_3O_4. The ultrafine particles can be prepared by thermal decomposition of iron(III) oxalate.

Hydrated iron(III) oxides

During the many wet chemical synthesis, like hydrothermal, usually iron hydrates are obtained. Several hydrates of iron(III) oxide exists. When alkali is added to solutions of soluble Fe(III) salts, a red-brown gelatinous precipitate forms. This is not $Fe(OH)_3$, but $Fe_2O_3 \cdot H_2O$ (also written as Fe(O)OH). More than a few forms of the hydrated oxide of Fe(III) exist as well. The red **lepidocrocite** γ-Fe(O)OH, occurs on the outside of rusticles, and the orange **goethite**, which occurs internally in rusticles. When $Fe_2O_3 \times H_2O$ is heated, it loses hydration water. Further heating at 1670 K converts

Fe_2O_3 to black Fe_3O_4 ($Fe^{II}Fe^{III}_2O_4$), which is known as the mineral magnetite. Fe(O)OH is soluble in acids, giving $[Fe(OH_2)_6]^{3+}$. In concentrated aqueous alkali, Fe_2O_3 disolvs producing $[Fe(OH)_6]^{3-}$. Different hydrated structures depending on synthesis conditions can be obtained []:

- goethite (α-FeOOH),
- akaganéite (β-FeOOH),
- lepidocrocite (γ-FeOOH),
- feroxyhyte (δ-FeOOH),
- ferrihydrite, with approximate compositions: $Fe_5HO_8{\cdot}4H_2O$; $5Fe_2O_3.9H_2O$; or $FeO(OH)\ 0.4H_2O$.

The typical XRD spectra of the ferrihydrite synthetized from 0.2 M ferric nitrate $Fe(NO_3)_3$ ×·$9H_2O$, with 1.0 M sodium hydroxide (NaOH) [102], is shown in Figure 2.27.

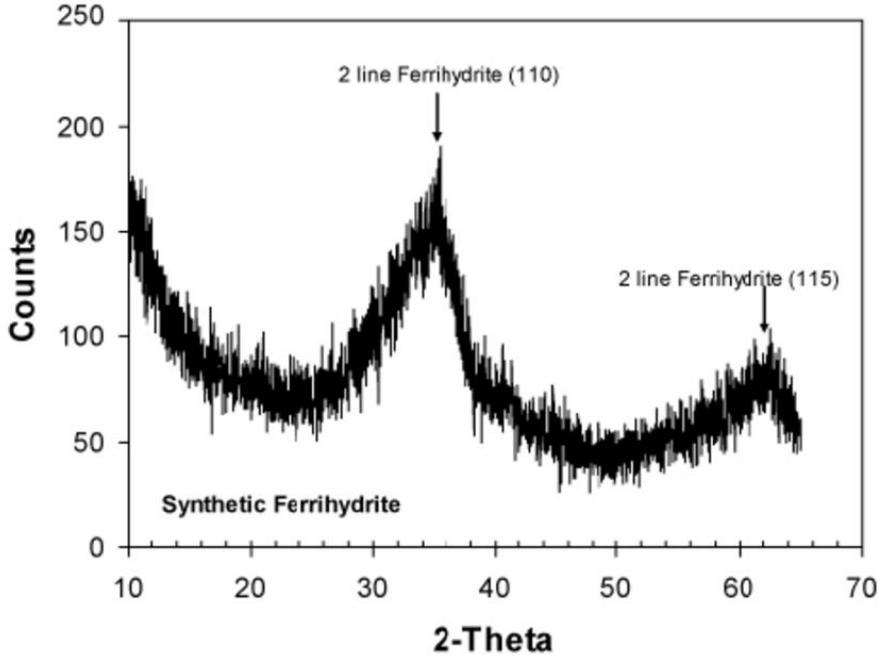

Figure 2.27. XRD pattern for the synthetic low crystalline ferrihydrite [102].

For the further evaluation of possible iron oxide structure, the XRD patterns as the very reliable of most common iron oxides is shown in Figures 2.28-2.2.31 [103],

while table 2.4 provides the structure and XRD widths of most intensive XRD diffraction peaks [103].

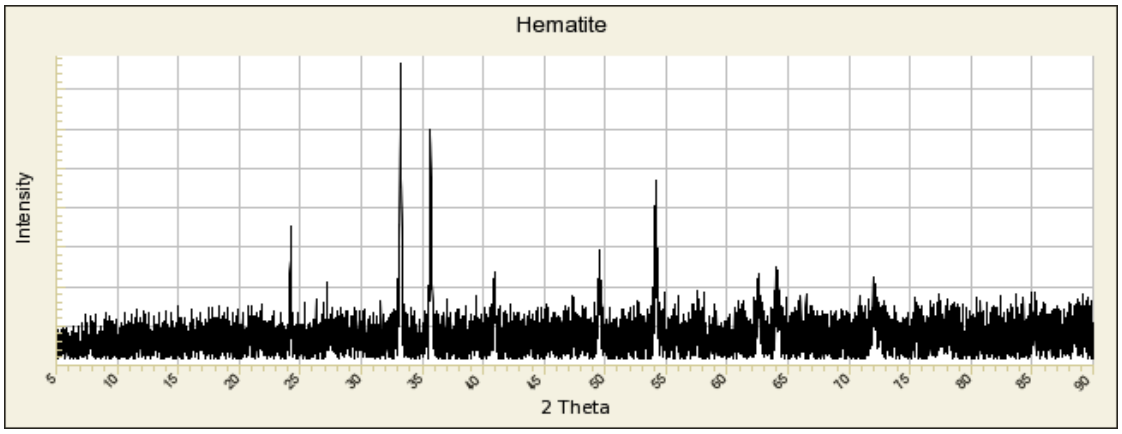

Figure 2.28. XRD of hematite [103]. Unit cell parameters: a: 5.0329(3)Å, b: 5.0329(3)Å, c: 13.743(2)Å

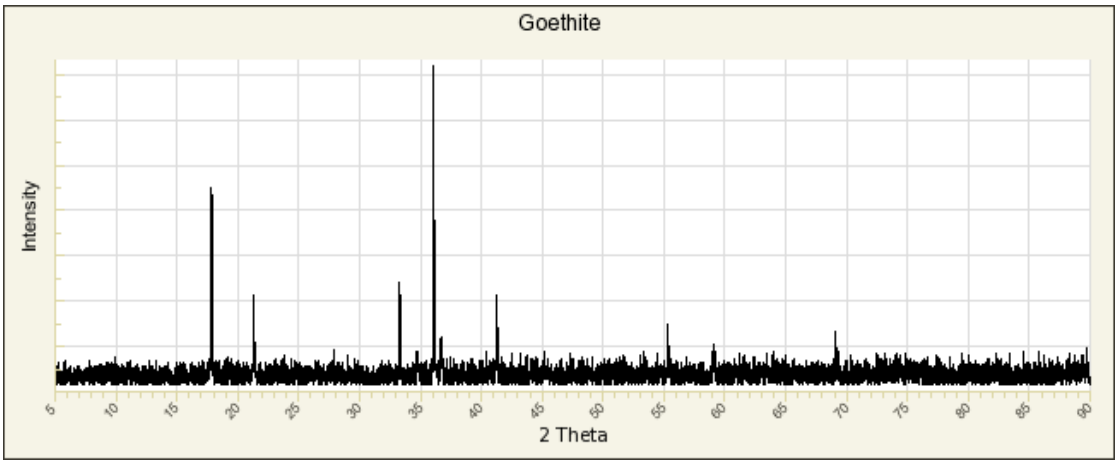

Figure 2.29. XRD of geothite [103]. Unit cell parameters a: 9.9613(2)Å, b: 3.0226(2)Å, c: 4.6017(3)Å.

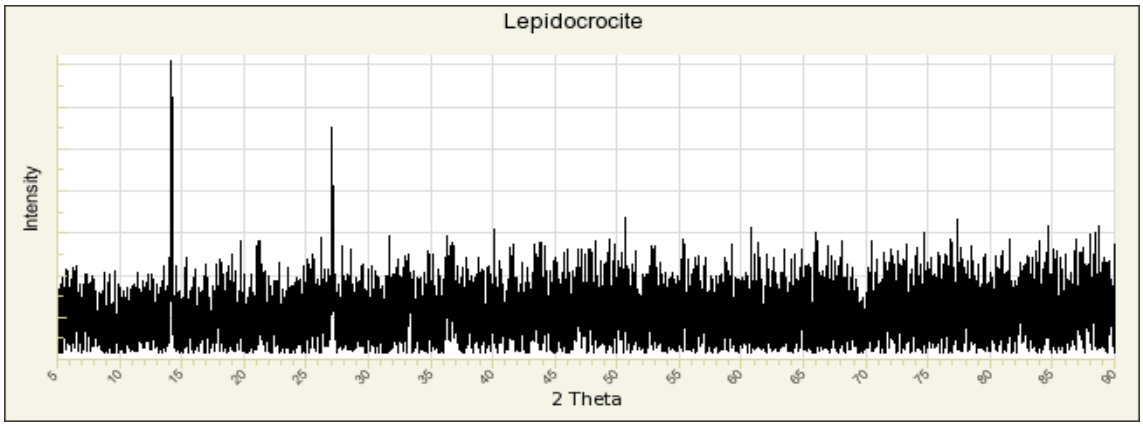

Figure 2.30. XRD of lepidocrocite [103]. Unit cell parameters: a: 12.4682(7)Å, b: 3.8584(5)Å, c: 3.064(1)Å.

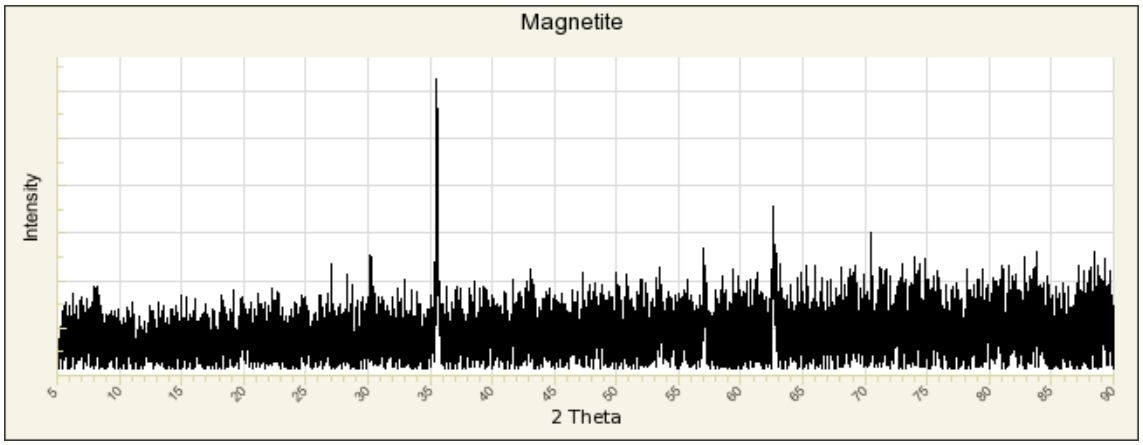

Figure 2.31. XRD of magnetite [103]. Unit cell parameters: a: 8.3961(5)Å, b: 8.3961(5)Å, c: 8.3961(5)Å.

Table 2.4. Crystal structure and strongest XRD peaks for various iron oxides [104].

Mineral name/formula	Hematite α-Fe_2O_3	Maghemite γ-Fe_2O_3	Goethite α-FeOOH	Akaganeite β-FeOOH	Magnetite Fe_3O_4
Crystal system	Trigonal	Cubic or tetragonal	Orthorhombic	Monoclinic, β = 90.24°	Cubic
Most intense XRD spacings, nm	0.270, 0.368, 0.252	0.252, 0.295	0.418, 0.245, 0.269	0.333, 0.255, 0.7467	0.253, 0.297

2.5.1. Photoelectrochemistry of hematite

From the photoelectrochemical point of view, the α-Fe_2O_3 or hematite is a dominant structure. Hematite by means of a photoanode material for photoelectrochemical water oxidation has attracted substantial attention owing to its suitable bandgap for light absorption, excellent chemical stability, natural abundance, and environmental compatibility [104]. The working mechanism of a photoelectrochemical cell using α-Fe_2O_3 photoanode is illustrated in Figure 2.32 [104]. n-type hematite is used as the photoanode where water oxidation occurs; simultaneously, water reduction take place on the cathode. At the semiconductor–electrolyte interface, a space charge layer (depletion layer) is formed due to ion absorption. The position of valence band is around 1.8 V SHE (~ –6.5 eV), which is

suitable positions for interaction of holes with electrons from water to be oxidized. The position of conducting band is near 0 V SHE (~ –4.5 eV), so the electrons theoretically could reduce protons to hydrogen but due kinetics limitations this reaction is only theoretically possible. After illumination, photoexcited electrons (e^-) are separated at the space charge layer and further transferred to a counter electrode to reduce proton or water, resulting in the hydrogen gas evolution. At the same time, fotmed holes (h^+) travel to the photoanode surface which are driven by a space charge field to oxidize water, thereby resulting in oxygen evolution [104]:

Counter cathode: $2H^+ + 2e^- \rightarrow H_2$

Photoanode: $2H_2O + 2h^+ \rightarrow 4H^+ + 2e^- + O_2$

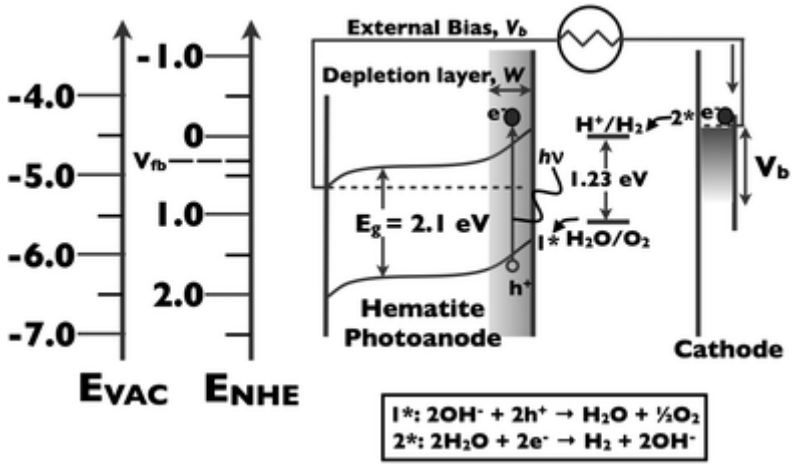

Figure 2.32. Energy diagram of n-type hematite photoanode and schematic illustration of photoelectrochemical water splitting on photoanode and cathode [104].

Hematite band-gap is typically between ~2.0–2.2 eV due to its combination of sufficiently broad visible light absorption, up to 590 nm, and excellent stability under alkaline operating conditions. The theoretical solar energy conversion efficiency is 14–16.8%. Nevertheless, the reported solar-to-hydrogen efficiency of α-Fe_2O_3 is significantlly lower than the theoretical value, mainly due to its very short excited state lifetime (<10 ps) and short hole diffusion length (~2 to 4 nm) [104]. The majority of

photoexcited electrons in α-Fe_2O_3 are typically lost via different electron–hole recombination processes within the first few picoseconds, and only holes created close enough to the semiconductor/electrolyte interface can be used for water oxidation. In this regard, very thin α-Fe_2O_3 films are required to be used for facilitating transport/collection of electrons and holes. Nanostructures with small grain sizes provide large surface areas and short hole diffusion distances, which can potentially address short hole diffusion limitations.

Some Authors pointed out the crucial role of the accumulation of holes at the surface, at so-called surface states, Figure 2.33 [105], of hematite electrodes under visible light irradiation. This leads in decreasing the photocurrent [106,107]. So far, a clear discrimination of recombination and charge transfer rates, as well as the role of the applied voltage, has not yet been elucidated.

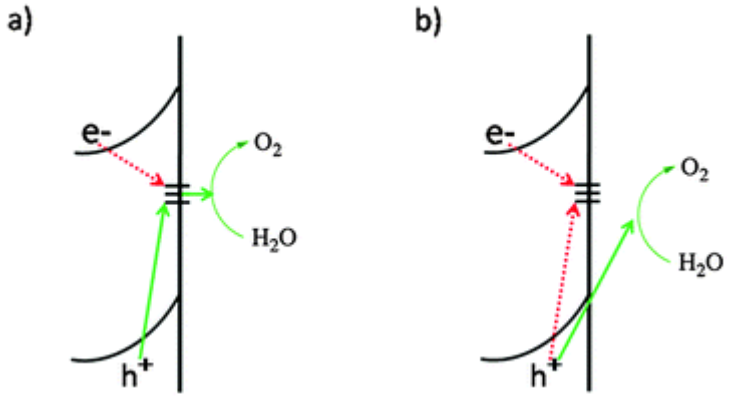

Figure 2.33. Relative energy diagram for water oxidation at hematite where (a) the surface states are involved in the mechanism through an innersphere mechanism and (b) surface states only serve as a recombination pathway where hole transfer occurs through an outer sphere mechanism [105].

Scheme 2.1 illustrates the complications arising from the fact that the oxidation of water is a 4-electron process, so that holes need to be 'stored' in intermediate or surface states [108]:

$$h\nu \rightarrow h^+ + e^-$$
$$Fe(III)_{surf} + h^+ \rightarrow Fe(IV)_{surf}$$
$$Fe(IV)_{surf} + h^+ \rightarrow Fe(V)_{surf}$$
$$2Fe(V) + 2\ H_2O \rightarrow 2\ Fe(III) + O_2 + 4H^+$$

Scheme 2.1.

The Fe(IV) and Fe(V) intermediates in this scheme can also act as electron acceptors, so that surface recombination reactions of the kind shown in Scheme 2.2 are probable to take place [108]

$$Fe(IV) + e^- \rightarrow Fe(III)$$
$$Fe(V) + e^- \rightarrow Fe(IV)$$

Scheme 2.2.

The Fe(IV) and Fe(V) states can also be thought of as 'surface-trapped holes', which may have sufficient surface mobility to allow second order reactions of the type illustrated by the last step shown in Scheme 2.1.

In Figure 2.34 a polarization curve of pulsating illumination for sol-gel hematite thin films is shown [96]. The response to the light pulse is fast and after the initial photocurrent jump decreases due to the significant recombination of the electron-holes pairs, whereby fast responses (peaks, sparks or overshoting) are formed, which means that thin Fe_2O_3 saffers from very fast recombination processe.

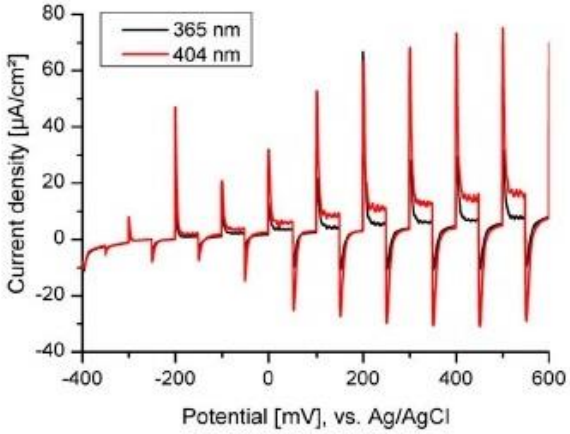

Figure 2.34. Polarization curve of pulsating illumination for sol-gel hematite thin. Wavelength radiation of 365 nm and 404 nm [96].

Annealing treatment at 650 and 750ºC improve the photocurrent characteristics, Figure 2.35 [96], but still overshooting is present indicating number of recombination centers.

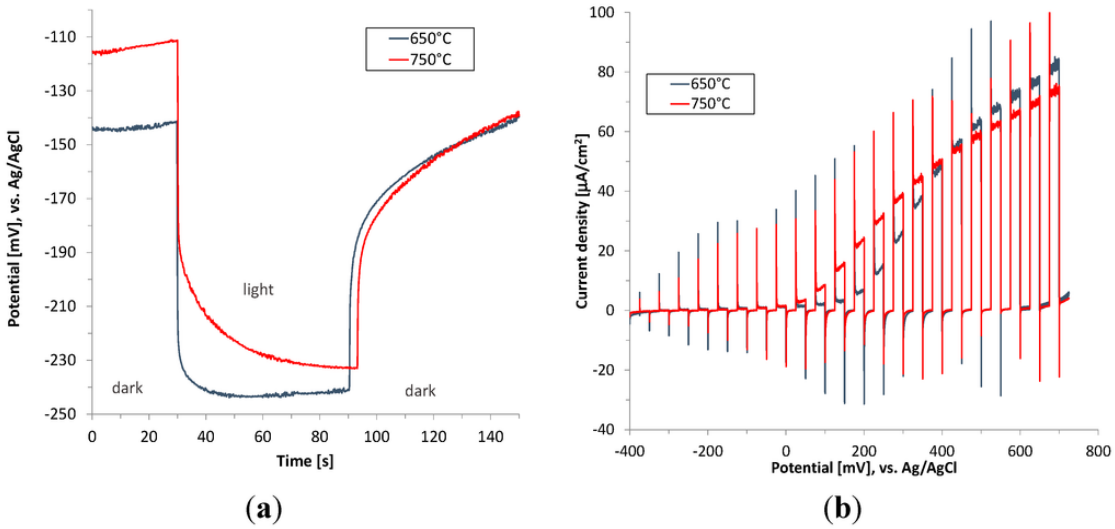

Figure 2.35. Open circuit potential (OCP) (**a**) and chopped light polarization curve (**b**) for hematite thin films calcined at 650 °C and 750 °C (on conducting glass FTO electrode). Irradiation wavelength 365 nm (1.46 mW cm^{-2}) [96].

Cummings et al. [109] obtained similar results on thin mesoporous films of α-Fe_2O_3 prepared on conducting glass substrates using layer-by-layer self-assembly, as can be seen in Figure 2.36.

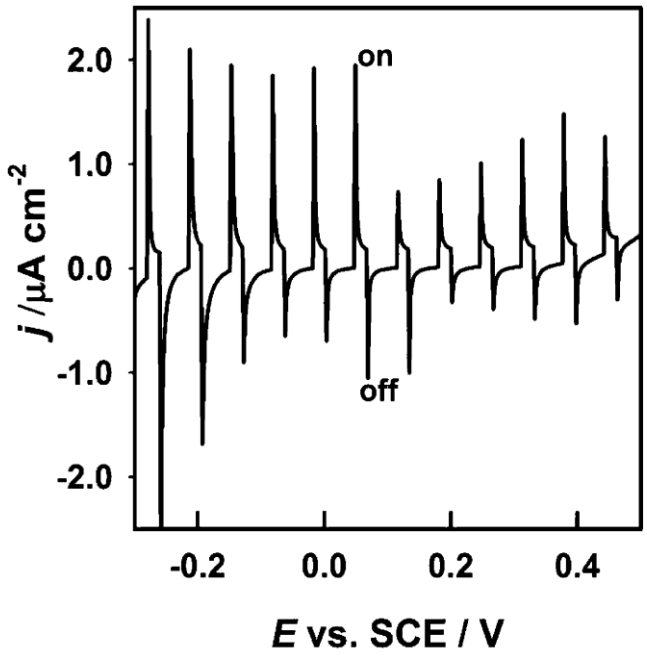

Figure 2.36. Photo-voltammogram of 40 layer α-Fe_2O_3 film under chopped monochromatic illumination. Sweep rate 10 mV s−1. Illumination 365 nm, 10 mW cm^{-2} in 0.1 M NaOH [109].

Wanga et al. [110] investigated the photo activity of the hematite nanorods thermally grown on Fe–Ti alloys. Authors observed that annealing treatment influenced the photoactivity and recombination rate. Samples annealed in mixture of air and argon practically did not show characteristics transients (sparks) of recombinations, as can be seen in Figure 2.37.

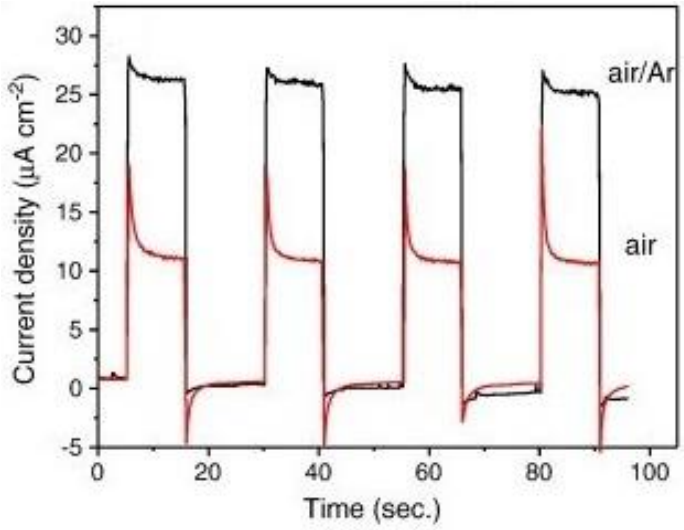

Figure 2.37. The photocurrent at 360 nm at 1.5 V_{RHE} in 1 M KOH for Fe2Ti alloy annealed in air and air + Ar conditions, photocurrents are excited to AM 1.5, 100 mW cm^{-2} simulated sunlight [110].

2.6. Successive ion layer adsorption and reaction method (SILAR)

The solution-based method is a facile and scalable method to fabricate nanostructures. α-Fe2O3, with different morphologies such as nanoparticles, nanowires, nanotubes, hollow spheres, and nanoflowers, has been fabricated via solution-based methods such as hydrothermal, solvothermal and sol–gel routes [104]. All of these methods are time consuming and relatively complicated.

Successive ion layer adsorption and reaction (SILAR) is one of the simplest ways to obtain metal oxide thin films at room temperature in a relatively short time [25, 26, 27].

The SILAR procedure consists mainly of four steps designed to allow the production of thin films in the water of insoluble materials on the selected substrate. The substrate on which a thin film is desired is treated with two different solutions: one containing metallic ions that are adsorbed on the surface and another containing an anion which reacts with adsorbed metal ions giving a hard soluble salt. Rinsing can be done between the two steps. These steps are repeated constantly in order to obtain the coating of the desired characteristics.

For example, Jayram et al. [111] and Sonia et al. [112] prepared copper oxide using SILAR procedure. In a typical procedure, $CuSO_4 \times 2H_2O$ is dissolved in diluted NH_3 to form a copper ammonia complex solution that represented a cationic precursor. The SILAR growth process is a deposition cycle involving the alternate immersion of the substrate in cationic and anionic solutions interspersed with a rinse in double distilled water kept at room temperature. The substrate is first immersed in a beaker containing the cationic precursor for 40 s, resulting in the adsorption of the copper ammonia complex [$(Cu(NH_3)_4)^{2+}$] onto the substrates due to the Van der Waals forces. Following immersion of the substrate in DD water for 20 s resulted in the conversion of the adsorbed copper ammonia complex to copper hydroxide ($Cu(OH)_2$). The $Cu(OH)_2$ coated substrate is immersed in the anionic precursor (DD water at 80 ^oC) for 60 s to convert the copper hydroxide molecules to CuO. Then the substrates are dipped into DD water to detach the loosely bonded molecules. A drying period of 20 s is used between each deposition cycle. Uniform CuO nanostructures are obtained by repeating the deposition (20, 40 or 60 cycles). Figure 2.38 shows a schematic diagram of the preparation of the CuO nanostructures. The detailed chemical reactions involved in the SILAR growth process are as follows:

$$[Cu(NH_3)_4]^{2+} + H_2O = Cu^{2+} + 4NH_3 + OH^-$$

$$Cu^{2+} + 2OH^- = Cu(OH)_2$$

$$Cu(OH)_2 = CuO\ (s) + H_2O$$

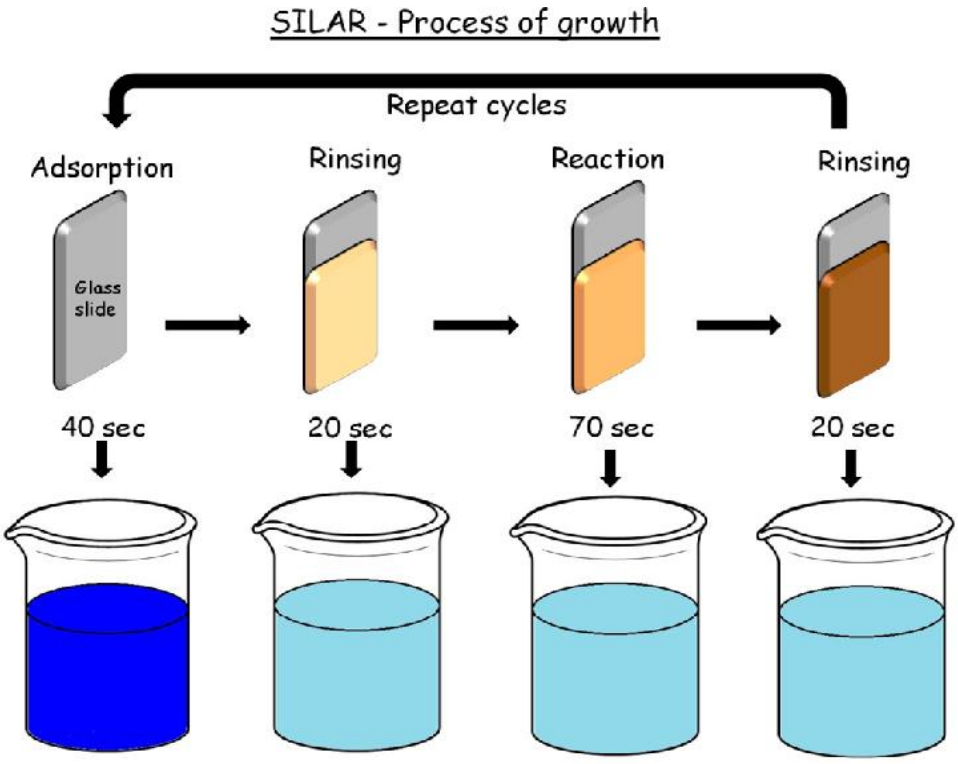

Figure 2.38. Schematic illustration of growth of CuO thin films by SILAR [111].

Advantages of SILAR method:

- It can be applied to produce any hard soluble coating by simple selection of precursor ions and solutions;
- The film thickness can be controlled by changing the time between the cycle;
- The coating can be applied at room temperature;
- *The substrate can be coated at room temperature;*
- The substrate can be of any shape.

The SILAR method of hematite synthesis and applications has not well elaborated in the literature. For example, Ubale and Belkhedkar [113] used the SILAR method for the thin film deposition of nanostructured α-Fe_2O_3, onto glass substrates with thickness of 156, 203 and 251 nm using $FeCl_3$ and NaOH as cationic and anionic precursors for antibacterial applications. Using the X-ray diffraction, they concluded that, α-Fe_2O_3 thin films are nanocrystalline in nature with rhombohedral structure. The thermo-emf measurements established that α-Fe_2O_3 exhibits n-type semi conductivity. In addition, Authors determined that synthetized samples has a band gap near 2 eV, as can be seen in Figure 2.39.

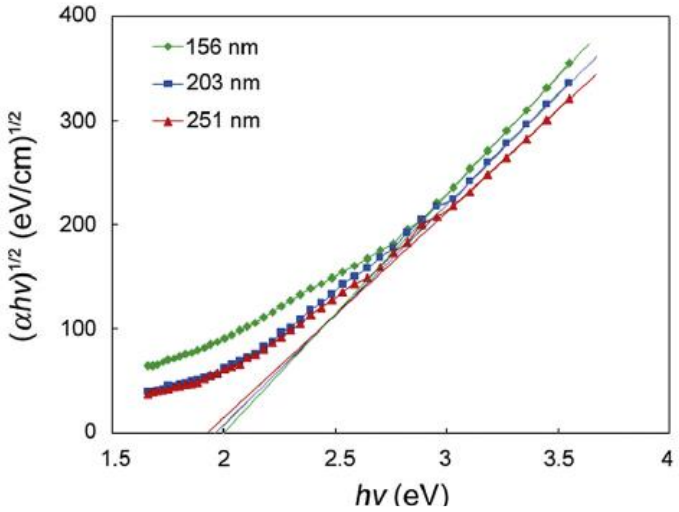

Figure 2.39. Plots of $(\alpha h\nu)^{1/2}$ vs $h\nu$ for α-Fe2O3 thin films [113]

Cristino et al. [114] modified ITO-glass surfaces of a triple-junction photovoltaic cell with SILAR. They also investigated massive precipitation of hydrous iron oxide using 50 mM of $FeCl_3$ in ethanol as cationic, and 1 M sodium hydroxide or 2.5 M sodium hypochlorite solutions as anionic precursors. In both cases amorphous hydrous Fe(III) oxides are obtained, generically indicated as $Fe_2(O)_{3-x}(OH)_x \cdot xH_2O$. Analyzing bulk and annealed bulk materials by XRD, UV-vis, FTIR, and Raman spectroscopy, they found that from sodium hypochlorite solutions mainly hematite, and from sodium hydroxide solution mainly magnetite phase is obtained. They also reported, based on the XPS measurement, that annealing treatment (100-300^oC) does not affect phase structure.

Authors also conducted massive precipitation of hydrous Fe(III) oxides by dropping 2.5 M NaClO (or 1 M NaOH) in a saturated $FeCl_3$ aqueous solution [114]. Then, the

precipitate is collected by filtration on a sintered glass frit, washed with water (in order to eliminate the remains of the salts) and dried under vacuum overnight. The dried oxide are then annealed at different temperatures for 1 hour. From the XPS spectra, shown in Figure 2.40, the Authors concluded that in all cases, iron oxide samples, heated in the 20–200 ^{o}C range, are essentially amorphous in morphological structure. The formation of a crystalline phase is induced only upon heated treatment at 300^{o}C of the sample precipitated from NaClO. The peaks at 2θ = 24.1, 33.2, 35.7, 40.92, 49.42, 54.08, 62.56, 64.06 are consistent with the presence of hexagonal hematite.

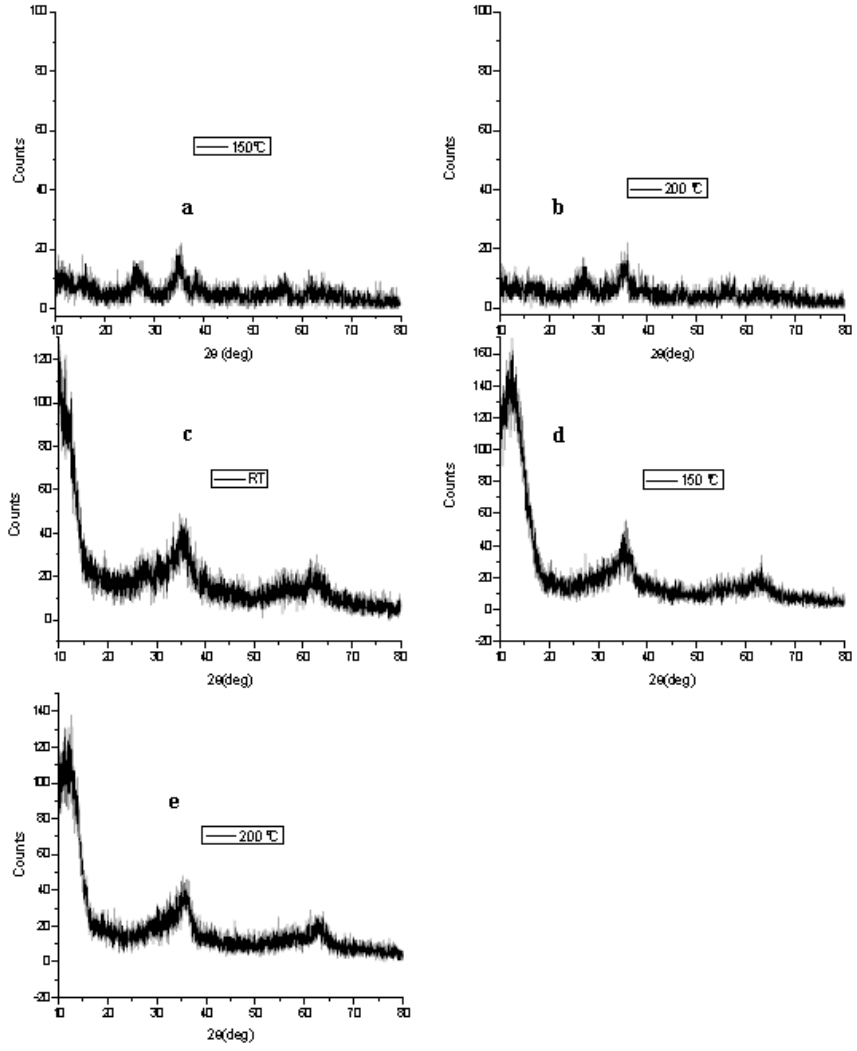

Figure 2.40. X-ray diffractograms of Fe(III) oxide powders precipitated from 2.5 M NaClO annealed at different temperatures in air: 150°C (a); 200°C (b). X-ray diffractograms of Fe(III) oxide powders precipitated from 1 M NaOH annealed at different temperatures in air: RT = 20°C (c), 150°C (d); 200°C (e) [114].

The FTIR spectra of all Fe(III) oxide samples, obtained by precipitation from either NaClO or NaOH solutions, share similar features (Figure 2.41a–f) [114].

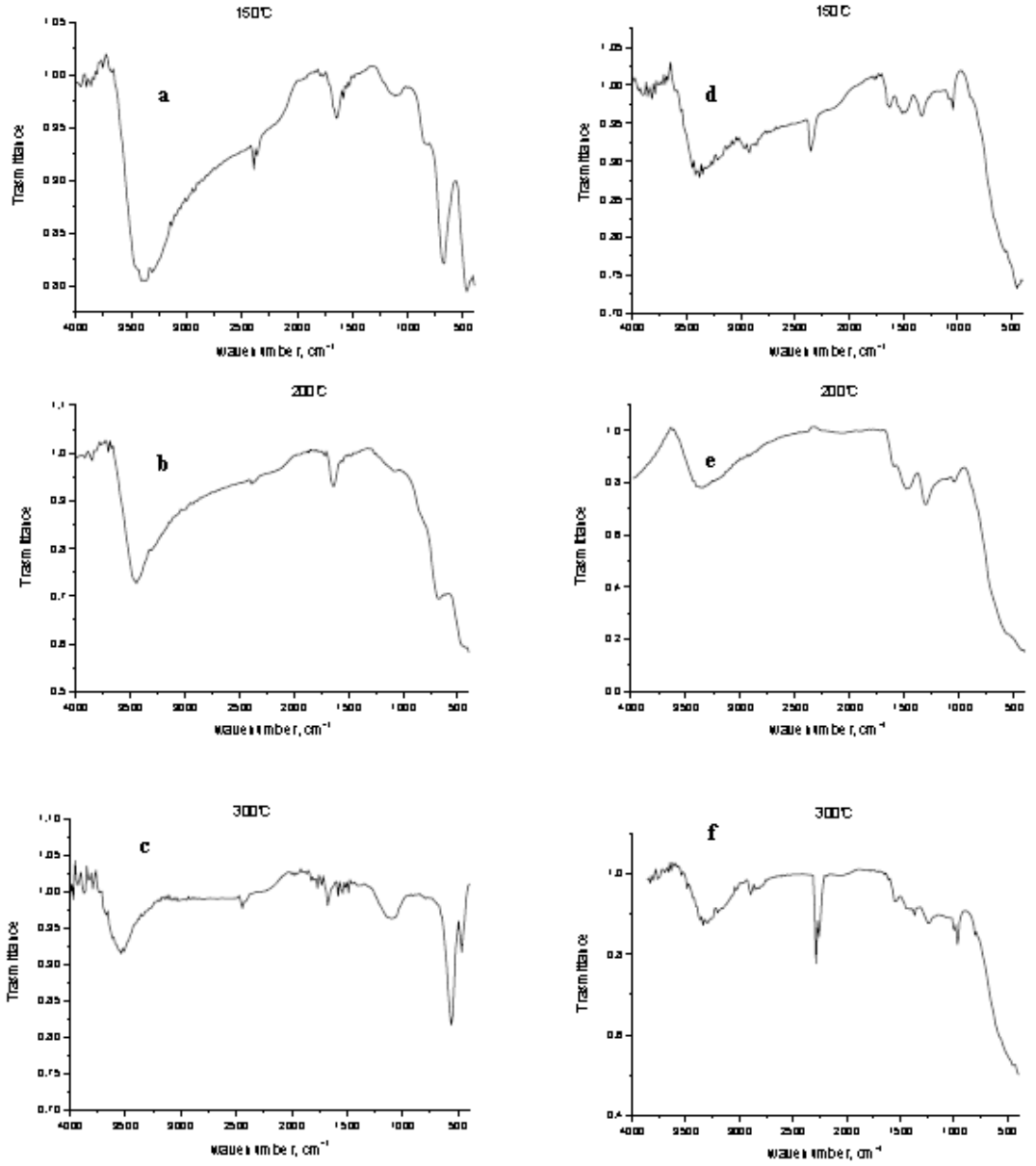

Figure 2.41. FTIR spectra of ferric oxide powders precipitated by addition of 2.5 M NaClO solution (a-c) and of 1 M NaOH solution (d-f) recorded in transmission mode in KBr pellet. Samples annealed at various temperatures: 150°C (a, d); 200°C (b, e); 300°C (c, f) [114].

In the high frequency region, a main broad band is observed at about 3500 cm^{-1} corresponding to OH stretching. The band at ~1650 cm^{-1} can be assigned to the scissoring mode of surface bound water molecules. Starting from 1000 cm^{-1}, a number of overlapping vibrational bands contribute to the intense absorption, which prolongs up to 500 cm^{-1}. These bands bear the main contribution of Fe–O and Fe–O–Fe deformation modes (Figure 2.41a–c). Author also reported that, the observed IR bands could be predicted rather well using density functional theory (DFT) calculations. Minimal Fe(III) oxide fragments, where two Fe(III) ions are singly or doubly bridged by oxygen atoms and are terminated with OH groups and water molecules, representing various local coordination environments of Fe(III) in the amorphous oxide materials. Each of these minimal fragments may contribute to the experimental spectrum.

From the XPS (X-ray photoelectron spectroscopy) analysis, Authors [114] concluded that samples of ferric oxide powder precipitated from both NaClO and NaOH solutions exhibited overall similar surface compositions. As expected, iron and oxygen are the main surface constituents, showing analogous concentration and binding energies in both samples. The Fe and O binding energies were consistent with ferric oxide. Thermal annealing does not alter their binding energy but improves the relative surface percentage of iron. This is due to a concomitant decrease of the percentage of carbon that is present both as an environmental contaminant and as adsorbed carbonate. A minor fraction of chloride is also observed, due to conglomeration of chloride anions during the precipitation stage, which could not be completely removed during the repeated washings of the precipitate.

2.7. Nanostructures of TiO_2-nanotubes and Fe_2O_3

Modification of the TiO_2 structures with different iron oxides are widely investigated, as reported by Kment et al. in their excellent review paper [115]. Few of the paper reported modification of the TiO_2 nanotubes with iron oxides using different methods.

For example, Kontos et al. [116] modified TiO_2 nanotubes using the coprecipitation method. Authors prepared a fine dispersion of the iron oxide nanoparticles coated with dextrin in the reaction of ferric chloride and ferrous chloride in the presence of ammonium hydroxide. In order to perform the surface modification, TiO_2-nanotubes obtained by electrochemical oxidation, is dipped in the sonicated aqueous suspensions of nanometric size iron oxide, shown in Figure 2.42a, with different concentrations in the range of 1-10 mg cm^{-3}. The iron deposits on TiO_2-nanotubes, which SEM images is shown in Figure 2.42b, strongly depend on iron oxide particle concentrations. For the lower concentrations, ~5 mg cm^{-3}, mainly the top of the TiO_2-nanotubes are covered, Figure 2.42c, while for higher concentrations practically all nanotubes are covered with iron oxides, Figure 2.42d.

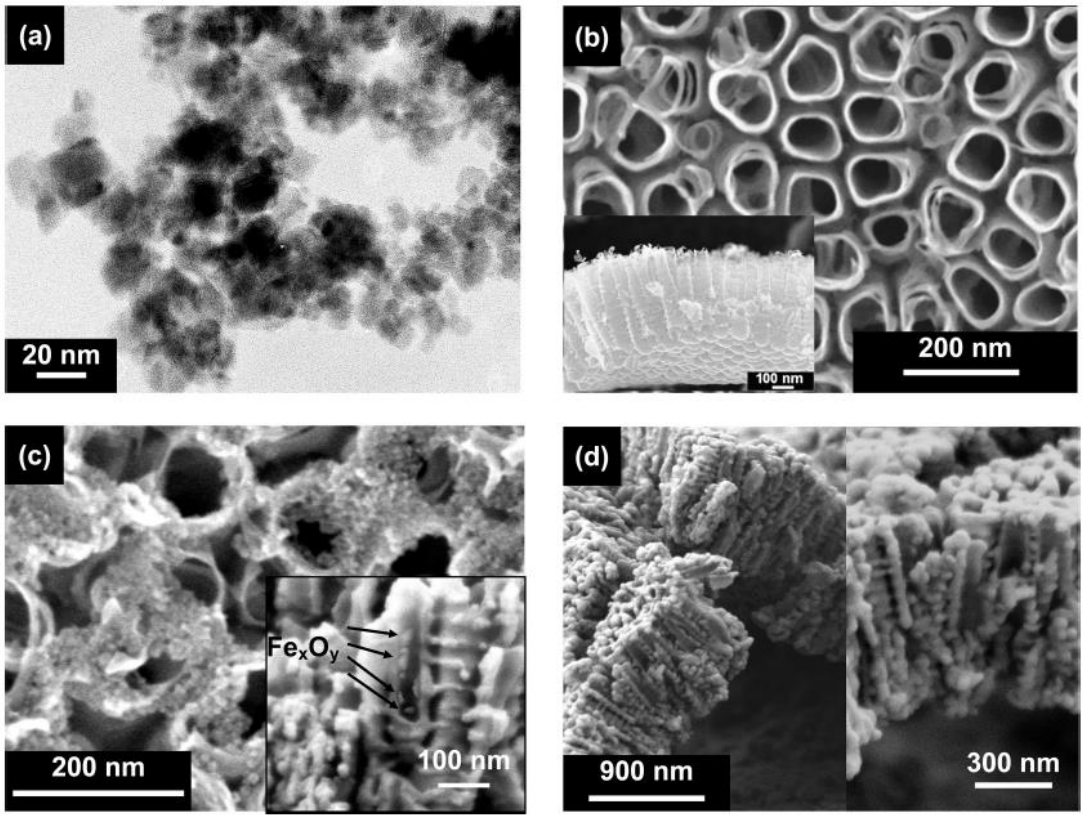

Figure 2.42. a) Low-magnification HRTEM micrograph of the Fe_xO_y nanoparticles. b) Top and side (inset) view SEM images of the unmodified TiO_2-nanotubes. c) Top and side (inset) view SEM images of the TiO_2-nanotubes after deposition of the iron oxide nanoparticles (5 mg cm^{-3}). Arrows indicate iron oxide clusters. d) SEM images of modified TiO_2 NTs after deposition of the iron oxide nanoparticles at high concentrations (10 mg cm^{-3}) [116].

Similar result are obtained by Jeon et al. [117] using an electrodepozition method for a hematite synthesis. They obtained TiO_2-nanotubes by anodization of Ti foil in a solution contained 0.5 M H_3PO_4 and 0.14 M NaF, in the assistance of ultrasound, at 20 V over 45 minutes. In order to produce hematite particles on TiO_2-nanotubes, shown in Figure 2.43c and d, they applied electrodeposition method. The as-prepared TiO_2-nanotubes are first immersed in a aqueous solution contained 0.5 mM NaF, 0.1 M NaCl, 1M H_2O_2, and 5 mM of $FeCl_3$ for different times 1 h and 24 h). After initial immersion times, they applied 50 potential cycles at a sweep rate of 0.1 V s^{-1} from –0.52 V to –0.41 V *vs* saturated calomel electrode. Finally, the hematite/ TiO_2-nanotubesis annealed at 500 ^oC for 30 min in the air atmosphere. From the presented STM images, Figure 2.43, it is obvious that TiO_2-nanotubes pre-immersed for 1 h in aqueous ferric ions (Fe^{3+}) contained solutions are covered only at the mouth of the TiO_2-nanotubes, Figure 2.43e, while TiO_2-nanotubes pre-immersed for 24 h are completely covered Figure 2.43e.

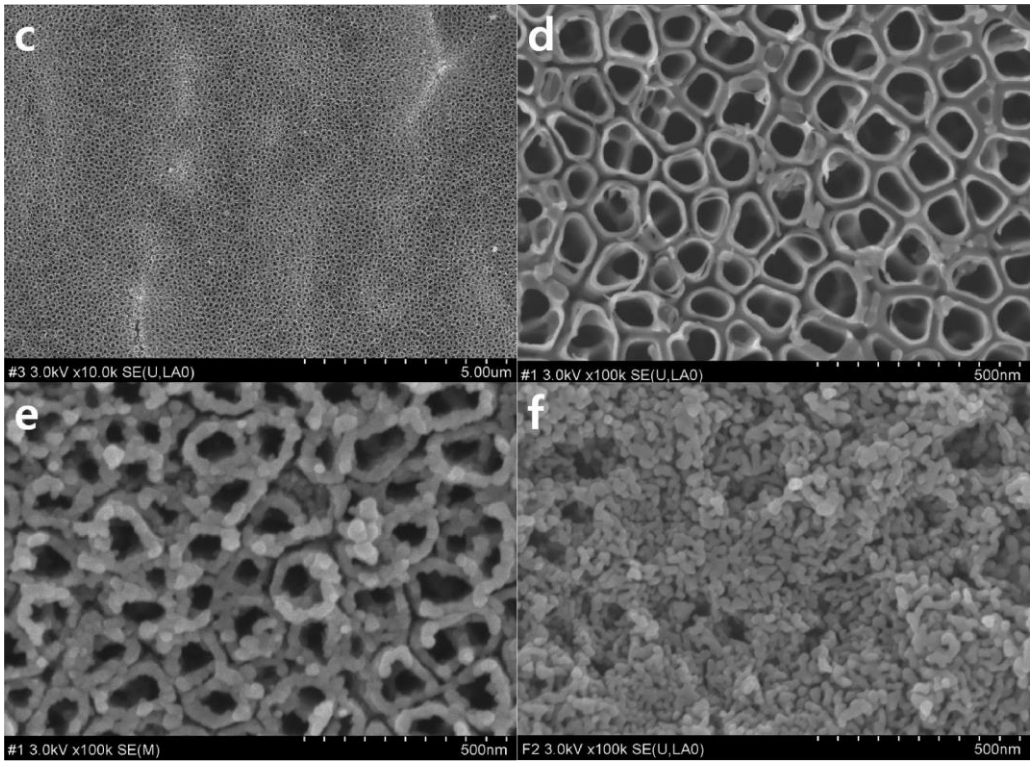

Figure 2.43. SEM images of (c, d) TiO_2-nanotubes under different magnifications, (e) hematite@1 h- TiO_2-nanotubes, and (f) hematite@24 h- TiO_2-nanotubes. 1 h and 24 h refer to pre-contact times of Fe(III) to TiO_2-nanotubes substrates for 1 h and 24 h, respectively, before electrodeposition [117].

Based on the SEM images analysis Authors schematically shown the deposited hematite on TiO_2-nanotubes, Figure 2.44. The short pre-contact time (1 h) of aqueous ferric ions (Fe^{3+}) on TiO_2-nanotubes resulted in formation of hematite particles selectively on the mouth surface of TiO_2-nanotubes, while the long pre-contact time (24 h) resulted in complete filling of the TiO_2-nanotubes inside and an even full covering of the top surface with the hematite nanoparticles [117].

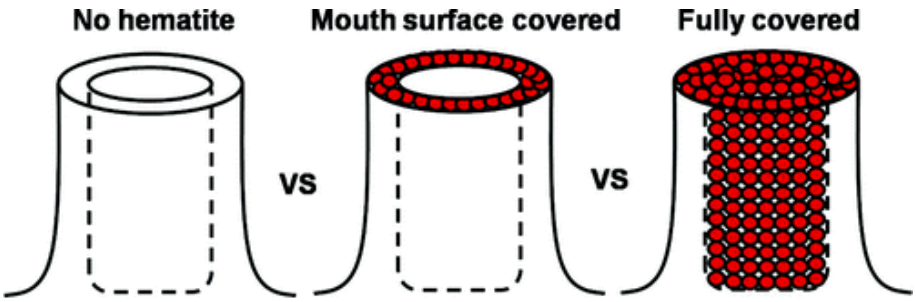

Figure 2.44. Schematic representation of electrodeposited hematite on TiO_2-nanotubes for 1 h of pre-immersion (middle) and 24 of pre-immersion (right) before electrodeposition [117].

The pre-immersion time, or obtained structures of TiO_2-nanotubes (TiNT) or nanoparticles (TiNP) with hematite also influence the photoactivity. Figure 2.45 shows the comparison of the photocurrent response of the investigated structures [117].

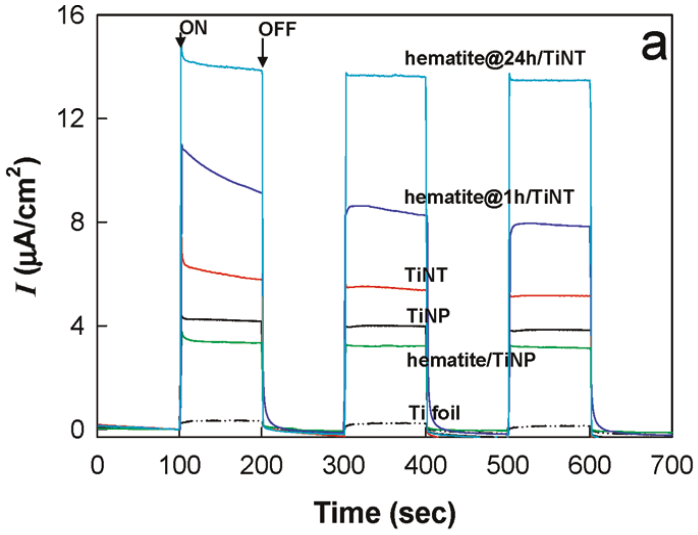

Figure 2.45. Comparison of photocurrent generations among samples under visible light ($\lambda > 420$ nm), AM 1.5-light source at E = 1.0 V SCE in 0.1 M Na_2SO_4 [117].

From Figure 2.45 it can be seen that TiO_2-nanotubes at potential of 1.0 V SCE in 0.1 M Na_2SO_4 reached stable photocurrent of ~5 μA cm^{-2}, TiO_2-nanotubes covered with hematite (1 h pre-immersed) ~8 μA cm^{-2}, while TiO_2-nanotubes covered with hematite (24 h pre-immersed) ~15 μA cm^{-2} [117].

Mohapatra et al. [118] synthetized hematite (α-Fe_2O_3) nanostructures on a titania (TiO_2) nanotubular template using a pulsed electrodeposition technique. The 1 dm^{-3} deposition bath are prepared from 60 g ferrous sulfate, 1.5 g ascorbic acid ($C_6H_8O_6$), 0.5 g amidosulfonic acid (H_2NSO_3H) and 15 g boric acid (H_3BO_3). The SEM images of the investigated systems is shown in Figure 2.46.

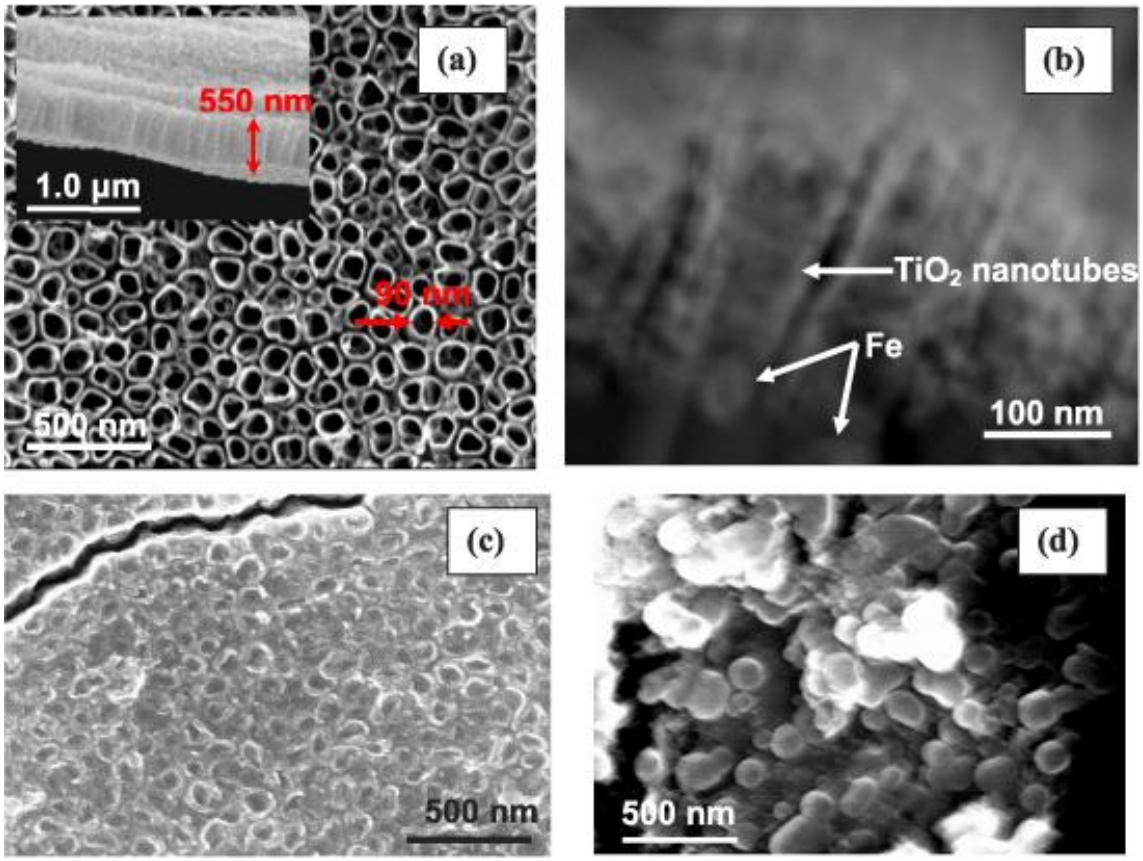

Figure 2.46. SEM image of (a) TiO_2 nanotube arrays; (b) a cross sectional image of Fe_2O_3 deposited at the bottom of the TiO_2 nanotube after 30 s deposition; (c) a surface view of the TiO_2 nanotube arrays filled with Fe_2O_3 deposited for 3 min; and (d) overgrowth of the deposited Fe_2O_3 comes out of the TiO_2 nanotubes in 5 min [118].

The Authors also observed improvement in the light absorption, heterostructure showed absorption in both the visible (due to Fe_2O_3) and UV region (due to TiO_2), as presented in Figure 2.47 [118].

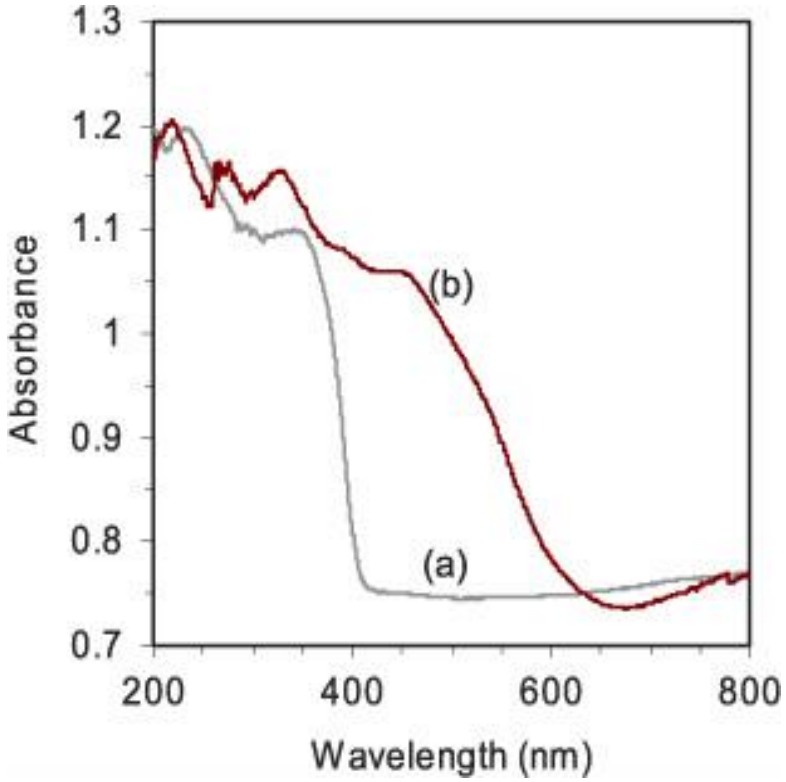

Figure 2.47. UV–vis spectra of: (a) TiO_2-nanotubes and (b) Fe_2O_3/TiO_2-nanorod–nanotube heterostructures. The heterostructure showed absorption in both the visible (due to Fe_2O_3) and UV region (due to TiO_2) [118].

Li et al. [119] showed that the ultrathin hematite film deposited on Ti foil has superior PEC performance than deposited on TiO_2 or FTO substrate. The photocurrent density of the α-Fe_2O_3/Ti photoanode synthetized at 450°C under 9 mW cm^{-2} Xenon light illumination at 0.6 V vs. SCE is approximately 80 μA cm^{-2}, Figure 2.48a. At low applied bias (−0.4–0.5 V), the transient current spikes are obvious, which could be the result of a rich surface defects. When the films were prepared at higher temperature, namely 550 °C in Fig. 2.49b, the spikes are reduced and photocurrent is enhanced from 40 μA cm^{-2} to 60 μA cm^{-2} at lower bias (0.4 V). The higher temperature improves the

crystallinity of the hematite thin films, which might indicate a lower level of surface defects, as can be concluded from Figure 2.49c.

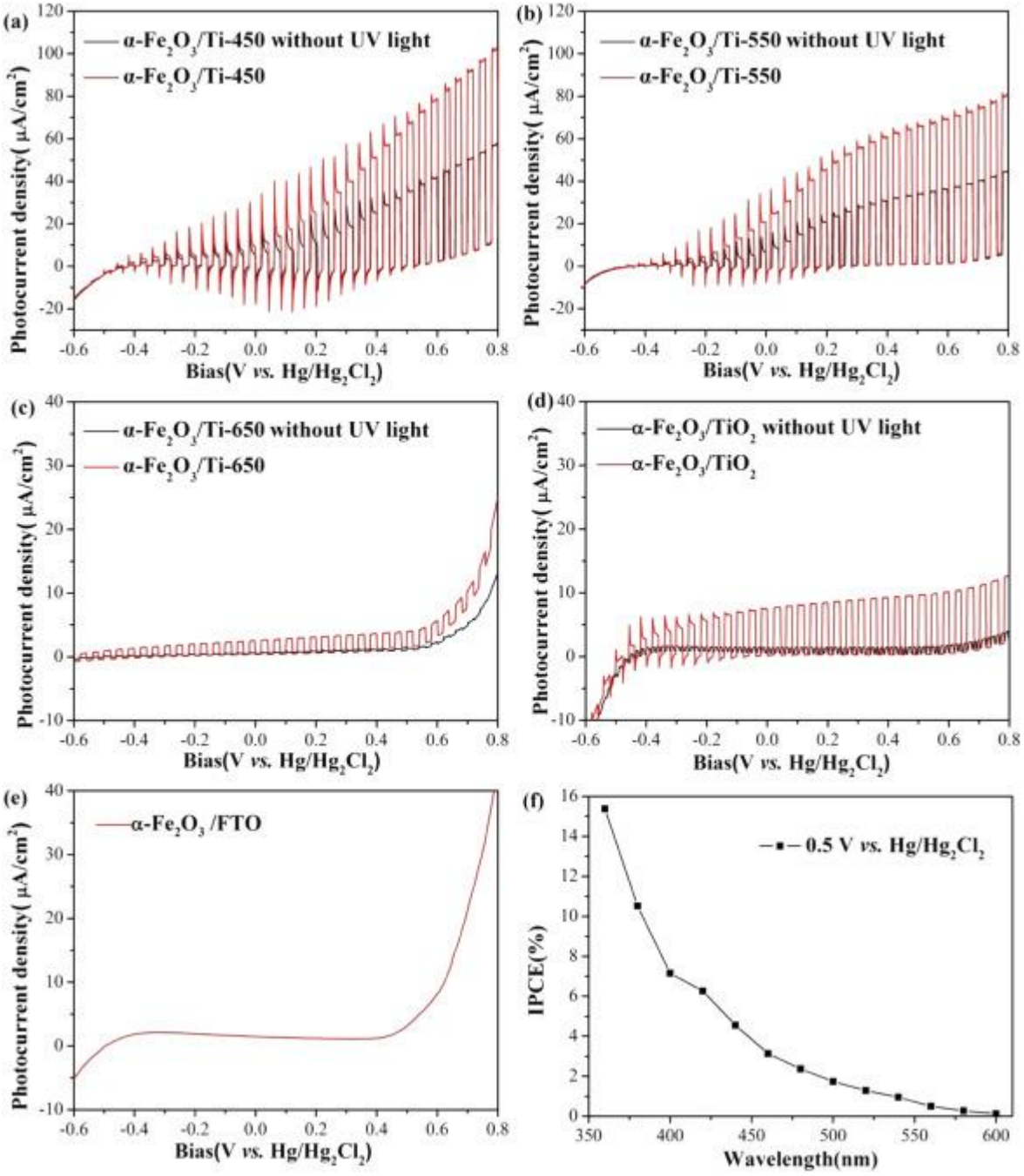

Figure 2.49. Chopped I–V curves of (a) α-Fe_2O_3/Ti-450, (b) α-Fe_2O_3/Ti-550, (c) α-Fe_2O_3/Ti-650 and (d) α-Fe_2O_3/TiO_2 with and without UV light. (e) Chopped I–V curves of α-Fe_2O_3/FTO. (f) IPCE performance of α-Fe_2O_3/Ti-450 at 0.5 V Ag/AgCl [119].

2.8. The band gap structures of hetero-junction of TiO_2 and Fe_2O_3

The positions of conducting and valence band of pure titanium dioxide and pure iron oxide for different pH values are shown in Figure 2.50 [adopted from 41] It can be seen that TiO_2 is theoretically capable to oxidize and reduce water, while hematite can only oxidize water.

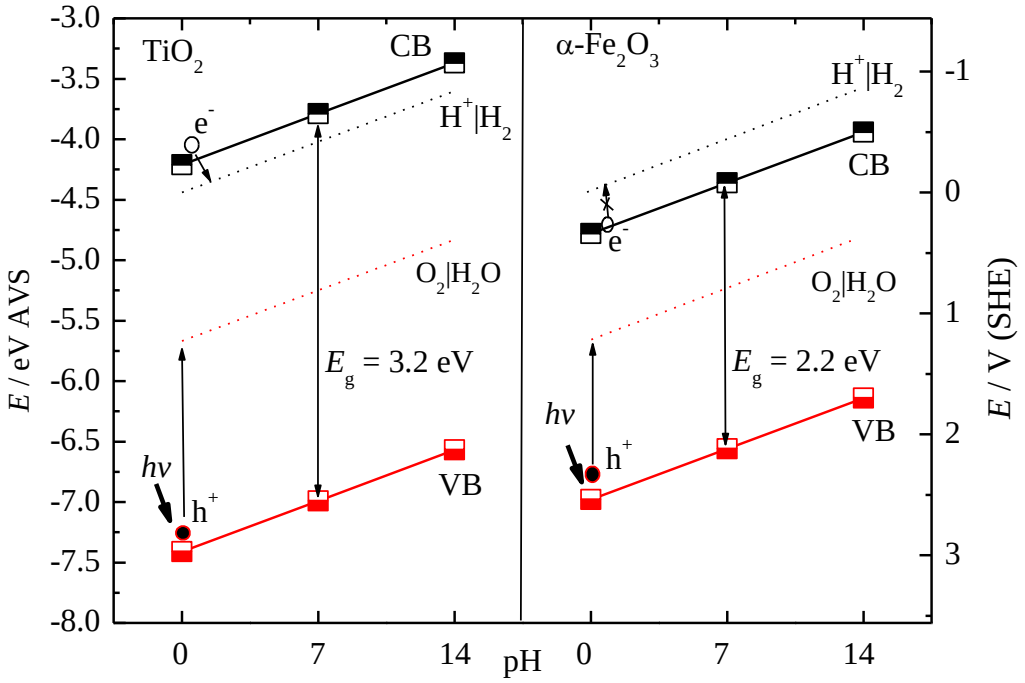

Figure 2.50. The positions of conducting and valence band of pure TiO_2 and α-Fe_2O_3 for different pH values of the electrolyte.

In the hetero-junction of TiO_2 and Fe_2O_3 situations is more complicated [120]. The main disadvantages related to the usage of Fe_2O_3 photoanodes include the great concentration of the surface states, short hole mobility, tiny charge-carrier life, and slow oxygen evolution kinetics [120]. Conversely, even TiO_2 photoanodes undergo from different drawbacks, in particular from reduced solar light collecting. Up to now, some researchers demonstrated that functionalization of Fe_2O_3 with TiO_2 results in inferior PEC performances with respect to bare iron(III) oxide. In a different way, the very high photocurrents shown by the present Fe_2O_3/TiO_2 photoanodes, along with the decreased

onset voltages and the absence of significant saturation at high-applied potentials, highpoint the advantage obtainable by Fe_2O_3/TiO_2 heterojunctions in giving promising photoactivity increases. Due to the related positions of Fe_2O_3 and TiO_2 conduction band edges, photogenerated electrons in TiO_2 could be simply relocated to Fe_2O_3 and added into the FTO substrate, and can subsequently transfer over the external electric circuit to reduce water or proton at the cathode, suppressing thus detrimental recombination effects. The different possible photo processes and corresponding time-scale is shown in Figure 2.51 [120], without and with the use of a positive external bias.

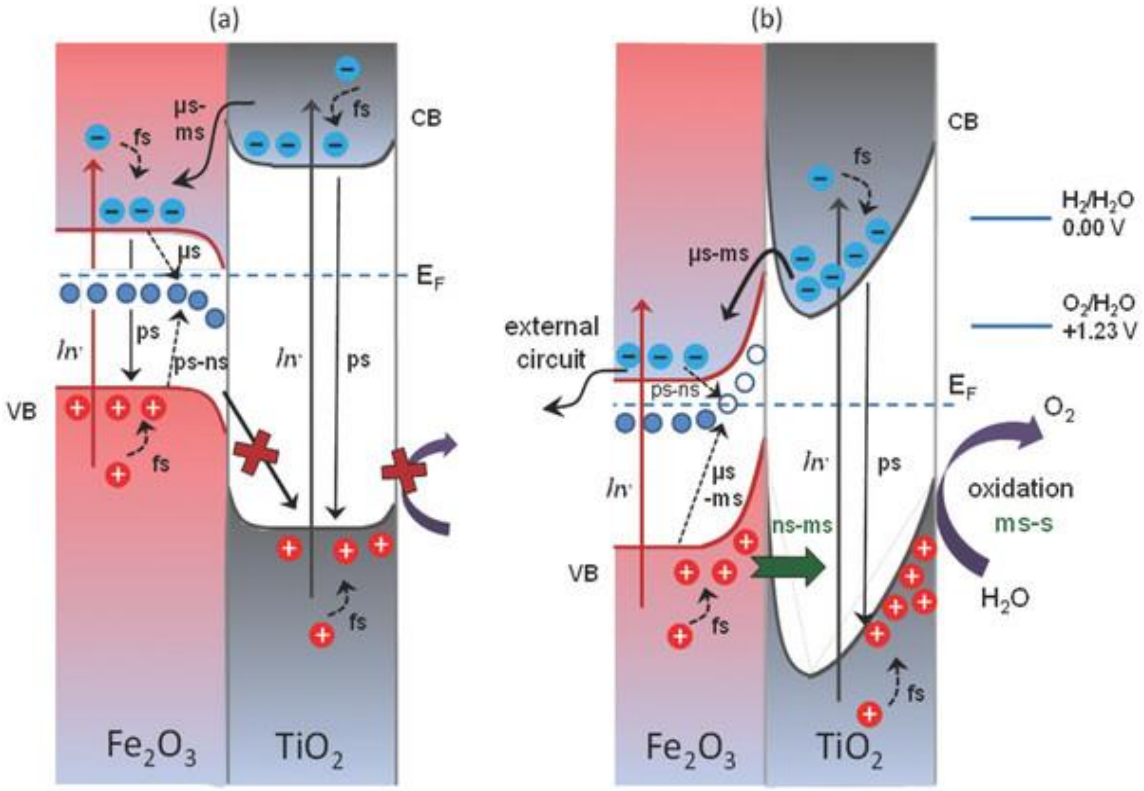

Figure 2.51. Schematic energy level diagrams illustrating the photoactivated charge transfer processes and related timescales: a) without and b) with the application of a positive external bias to Fe_2O_3 –TiO_2 photoanodes. The intraband electron-trap states, located a few 100 mV below the conduction band edge of hematite, are also shown (CB: conduction band, VB: valence band, E_F: Fermi level, fs: femtosecond, ps: picosecond, ns: nanosecond, μs: microsecond, ms: millisecond) [120].

Zhang et al. [121] investigated one-dimensional mesoporous Fe_2O_3@TiO_2 core–shell nanocomposites and presented different photo excitation under visible and UV iradiation, Figure 2.52. Under visible light the electrons from hematite is transferred to TiO_2 higher energy valence band that is unlikely, while under UV-light the opposite.

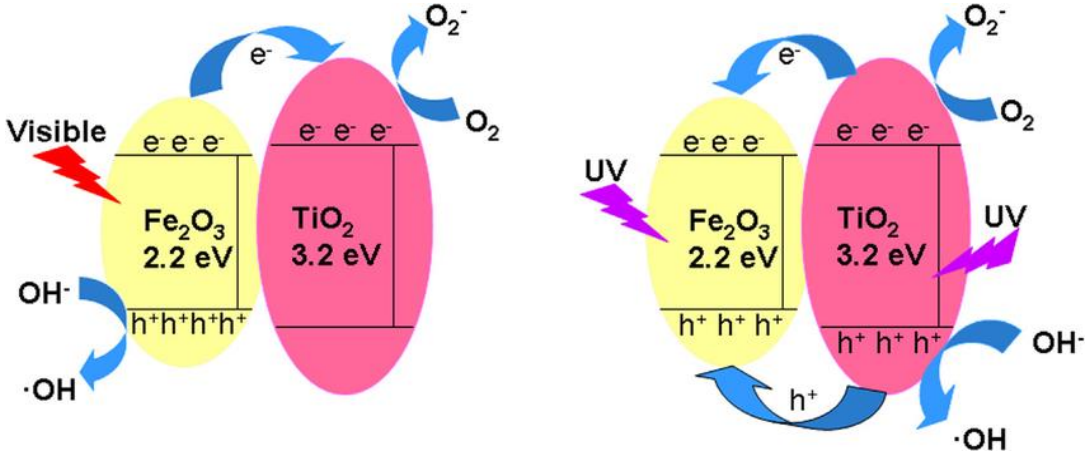

Figure 2.52. Schematic illustration of electron transfer between Fe_2O_3 and TiO_2 under visible and UV irradiation [121]

Ling et al. [122] proposed schematic band configuration and electron–hole separation at the interface of TiO_2 nanotubes - γ-Fe_2O_3 composites under ultrasonic irradiation, Figure 2.53. In their scheme Fe_2O_3 serves as electron acceptor, and hole donor to TiO_2.

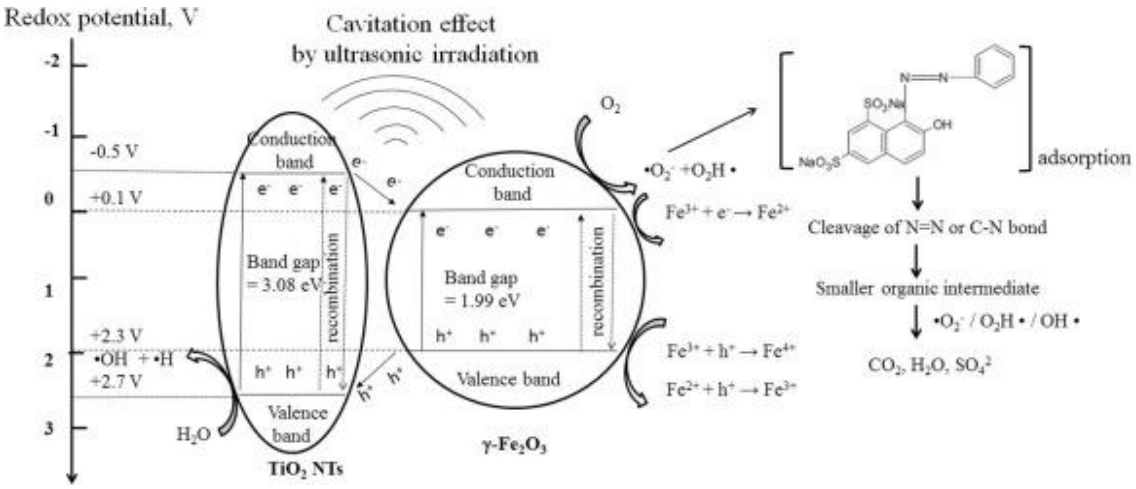

Figure 2.53. Proposed schematic diagram of band configuration and electron–hole separation at the interface of TiO2 NTs/γ-Fe_2O_3 composites under ultrasonic irradiation, with respect to the normal hydrogen electrode (NHE) at pH = 7 [122].

Fe_2O_3 heterostructure on TiO_2 nanorod arrays are investigated by Cao et al. [123]. Authors proposed scheme, Figure 2.54, that under visible light both materials forms electron-hole pairs, and electrons are transferred from CB of Fe_2O_3 to CB of TiO_2, and hole are transferred from VB of TiO_2 to VB of Fe_2O_3.

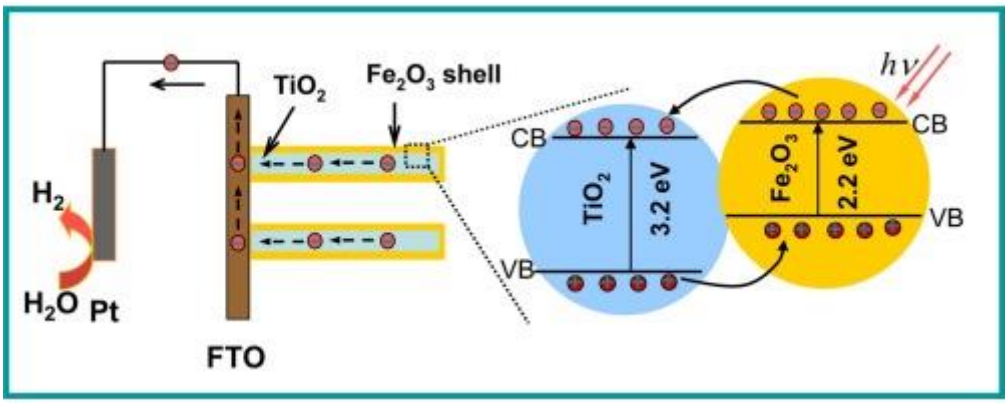

Figure 2.54. Schematic diagram shows band configuration and electron–hole separation at interface of Fe_2O_3@TiO_2 NRs heterostructure under visible light irradiation [123].

Investigating dendritic α-Fe_2O_3/TiO_2 nanocomposites, Li et al. [124] proposed that under visible light electrons in Fe_2O_3 are transferred to higher energy state orbitales, Figure 2.55, making preferable positions for transfer to TiO_2 conducting band.

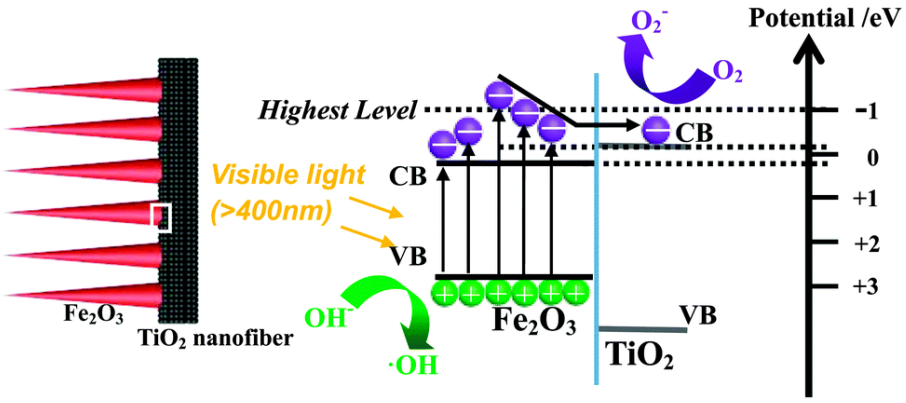

Figure 2.55. A schematic representation of interfacial charge carrier generation, transfer and separation between TiO_2 and Fe_2O_3 in the α-Fe_2O_3/TiO_2 heterostructure under visible light [124].

With respect to the above given schemes, the Authors did not consider the surface states in Fe_2O_3 surfaces, which must be included in the photocatalytic behavior of nanostructures, as explained in previous sections 2.5.1, and will be discussed in section results and discussion. However, presented schemes indicates that the differences of excitation exist under UV and visible light. This can be explained by the following schemes, Figure 2.56. The situation is purely indicative, but what occurs is probably that during UV-vis illumination the electron/hole pairs are formed on both phases (situation A); probably more charge is accumulated on Fe_2O_3 since it can benefit from absorption of both Vis and UV light and, consequently, one expects a negative shift of the bands and these should, rigorously speaking, be flatter than showed in (B). In situation (B), participation of TiO2 is negligible and should work as a sink of electrons as in dye-sensitized solar cells.

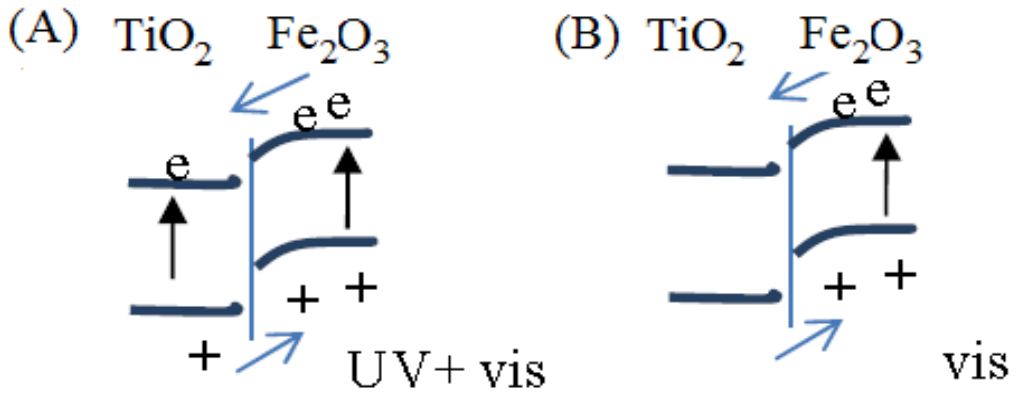

Figure 2.56. Schematic presentation of TiO_2-Fe_2O_3 nanostructures excitation under UV+visible light (A) and only visible light (B)

3. EXPERIMENTAL

Titanium dioxide nanotubes are formed by anodic oxidation of titanium in 1 M H_3PO_4 with the addition of 0.3 wt.% HF (based on the pure HF from 38 wt.% HF–water solution, p.a. Merck) using the well-established procedure reported by Bauer et al. [87]. A titanium foil, (Alfa Aesar, 0.127 mm thick), with the dimensions of 1 cm × 2 cm, is degreased in acetone and DI water in an ultrasonic bath. The electrochemical treatment, consisted of a voltage ramp from 0 V to 20 V with a sweep rate of ~0.5 V s^{-1}, followed by holding the voltage at 20 V for one hour. All anodization experiments are carried out using a Pt plane cathode, with an electrode distance of 3 cm, at room temperature in a plastic cell with the volume of 100 cm^3. For anodization, constant current-voltage DC Power Supply HY3003 (Mastech, Germany), is used. After the electrochemical treatment, the samples are rinsed with DI water and then dried.

The modification of the TiO_2 surface with iron oxide was made using the successive ion adsorption and reaction (SILAR) procedure. The iron ion precursor is 0.05 M $Fe(NO_3)_3 \times 9H_2O$ (p.a. Merck) in methanol, and the reaction medium was a 3.5 wt.% sodium hypochlorite solution (Centrohem, Serbia) with a pH~10.5. In a typical procedure, the anodized Ti electrode is immersed for 30 s in the ion precursor solution, dried with hot air, and exposed to the reaction medium for 60 s. Before repeating the cycle, the electrode is washed in pure methanol. SILAR consisted of five cycles, with the last immersion in HClO for 15 min, is performed. The electrode is then washed with DI water, methanol and dried in the air.

For the characterization, iron oxide in powder form is prepared as follows: 8 mmol of $Fe(NO_3)_3 \times 9H_2O$ are dissolved in 20 cm^3 of methanol, and slowly added (during 5 min) to 200 cm^3 of 3.5 wt.% HClO. After 15 min, the mixture is filtrated using a Büchner funnel and a water vacuum pump. After thorough rinsing with DI water and methanol, iron oxide is dried at room temperature. The product was black, crystal

like in appearance, but after grinding in an agate mortar, the color of the powder is orange-brown.

For the UV-vis study of the colloidal (Fe_2O_3 and TiO_2 modified with Fe_2O_3) water solution, a similar procedure is applied. Namely, 0.1 mmol of iron nitrate are dissolved in 1 ml of methanol and added to 10 ml of HClO, or ~1 mg anatase TiO_2 (Merck) powder is added to the iron nitrate solution and after 10 min, the suspension is added to 10 ml of HClO. After 15 minutes, the reaction mixture is centrifuged, and the solid phase is properly washed with DI water and methanol. The solid product is added to 10 ml of DI water, sonicated in an ultrasound bath for 30 min, and finally, after the precipitation of larger particles that lasted one hour, 3 ml of the solution is analyzed with an UV-vis LLG uniSPEC 2 spectrometer.

The chemical composition and morphology of the samples is analyzed using an Energy Dispersive Spectrometer (EDS) Isis 3.2, with a SiLi X-ray detector (Oxford Instruments, UK) connected to a scanning electron microscope (JEOL 5800 JSM, Japan) and a computerized multi-channel analyzer. High-resolution SEM images are taken by field emission SEM, MIRA3 TESCAN at 10 kV. The FTIR-spectra of the samples are recorded using a Bomen FTIR Spectrophotometer, MB-Series, in the form of the KBr pellets, and the XRD pattern of the samples is recorded with an Ital Structure APD2000 X-ray diffractometer in a Bragg–Brentano geometry using CuKα radiation and the step-scan mode (range: 10−80° 2θ, step-time: 0.50 s, step-width: 0.02°).

For the photoelectrochemical oxidation experiments the 100 cm^3 rectangular shaped Plexiglas box, from one side equipped with a quartz disk with a diameter of 3 cm is used as photoelectrochemical cell (PEC). The cell is connected via a Luggin capillary with an external glass reference electrode compartment. Saturated calomel electrode is served as a reference, and a Pt plate of 1 cm^2 as a counter (or working) electrode. All experiments are performed in 0.1 M Na_2SO_4 buffered to pH = 9.2 with 0.05 M $Na_2B_4O_7 \times 10H_2O$ (borax), and with a urea concentration in the range of 5 to 30 g dm^{-3}. To simulate voltage during electrolysis of water contained urea, stainless steel cathode (A=1 cm^2) is used, while for the fuel cell simulation, polarization curve of the oxygen reduction from the air at Pt cathode (A=1 cm^2) is used.

A homemade dark chamber equipped with an electromagnet-controlled blind, and a fan cooler are used, Figure 3.1.

Figure 3.1. Photographs of the dark chamber and light sources used in the photoelectrochemical experiments.

The light source is a polychromatic 300 W Osram Ultra-Vitalux light bulb that had a sun-like spectral distribution between 280 nm to 780 nm, and an IR region, Figure 3.2, without a cutoff filter.

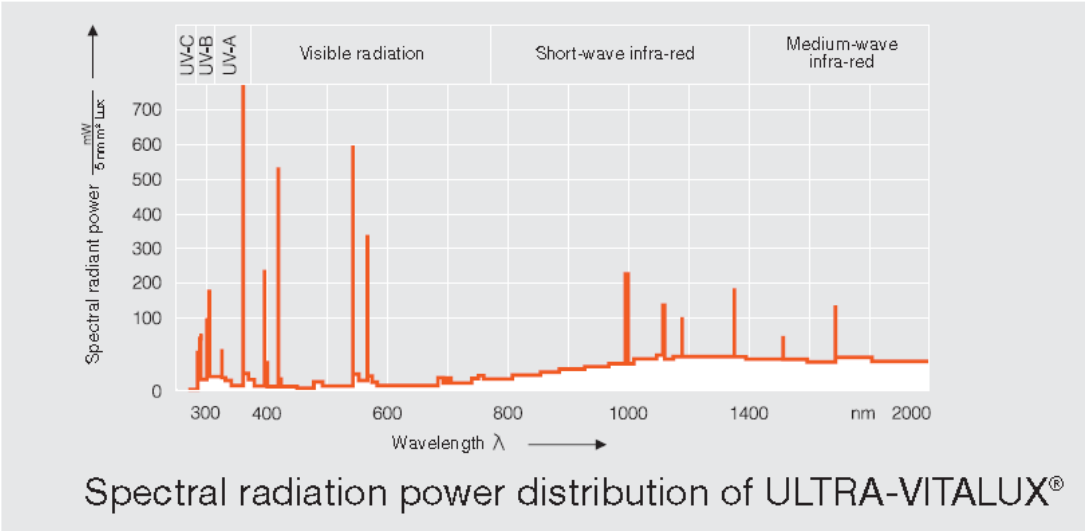

Figure 3.2. Distribution of the radiation energy of the lamp OSRAM ULTRA-VITALUX.

The light intensity is adjusted by changing the distance between the PEC and light source. The integral light intensity is measured by an Amaprobe SOLAR-100 Meter.

Electrochemical experiments are performed using a Gamry PC3 potentiostat/galvanostat, and the cell voltage was acquired with a digital voltmeter ISO-Tech IDM 73, interfaced to a PC via RS-232.

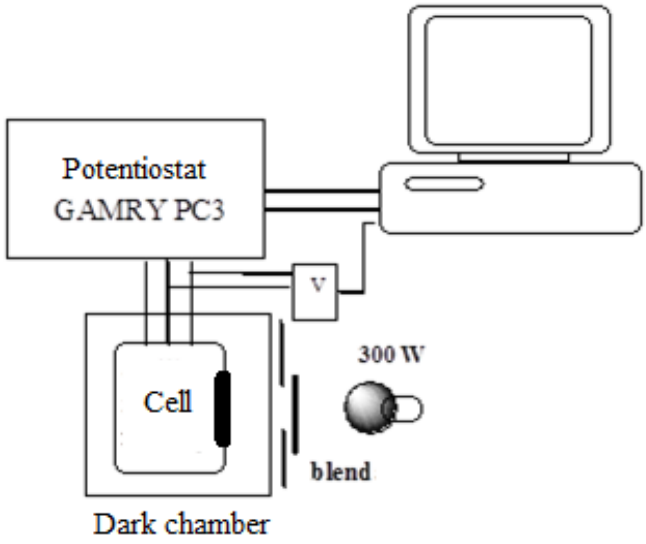

Figure 3.3. Block diagram of the measuring system connection.

4. RESULTS AND DISCUSSION

4.1. Synthesis and characterization

In Figure 4.1. the dependence of current and voltage on electrochemical oxidation of the titanium plate in a solution of 1 M H_3PO_4 with the addition of 0.3% by weight of HF are shown. The voltage is gradually increased up to a value of 20 V for two minutes to avoid significant dissolution, after which a constant value of 20 V was maintained. The current density is increased to ~ 17 mA in the initial period, to be stationed at about 3 mA.

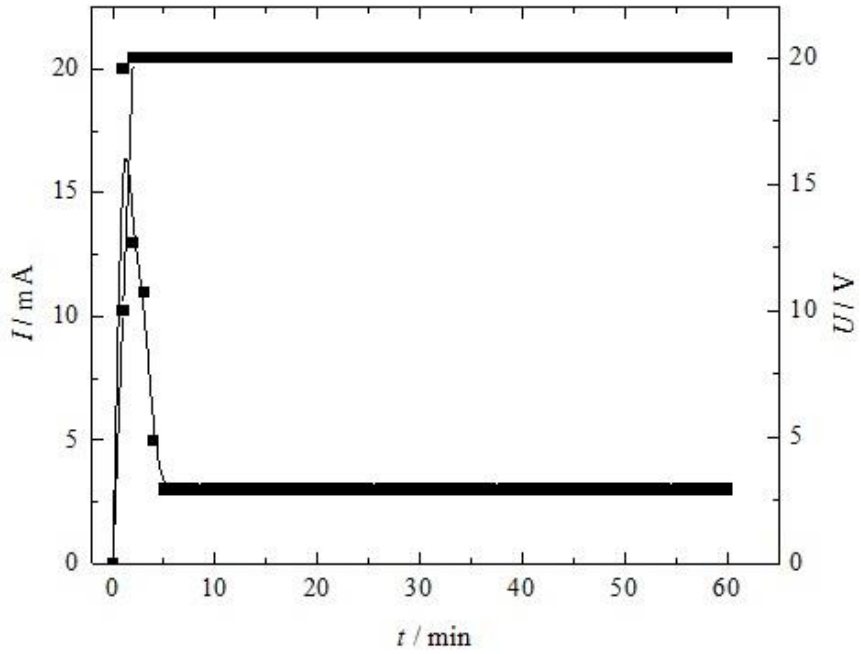

Figure 4.1. Dependence of current and voltage during electrochemical oxidation of titanium plate in a solution of 1 M H_3PO_4 with the addition of 0.3% by weight of HF.

Figure 4.2 shows high resolution SEM images of the as synthesized TiO_2 under different magnifications. In Figure 4.2b-d, it can be seen that TiO_2 is in the form of nanotubes (NT's). The diameter of TiO_2 nanotubes is estimated to be ~80 to 100 nm, which is in excellent agreement with the data reported by Bauer et al. [87].

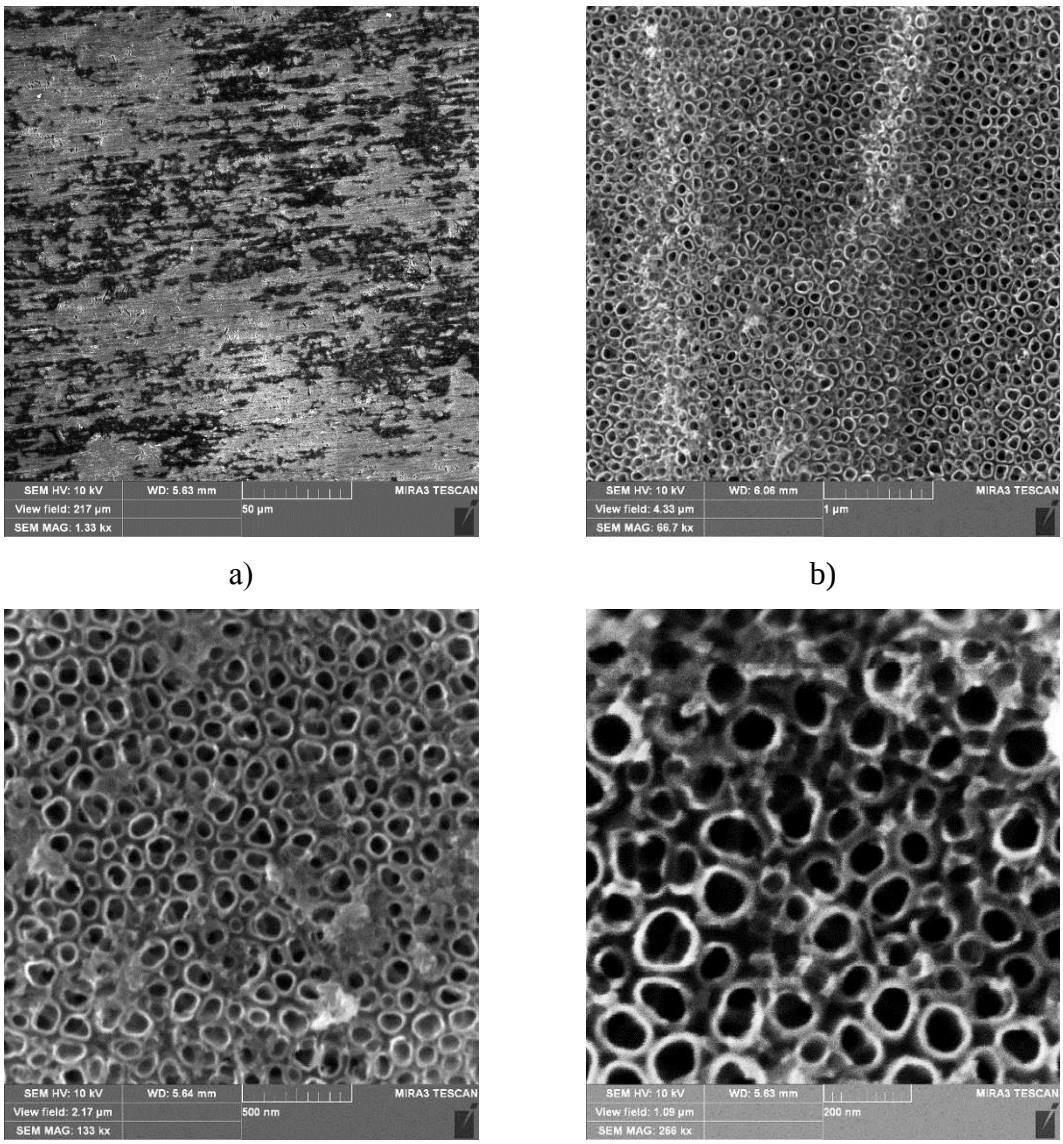

a) b)

c) d)

Figure 4.2. High-resolution SEM image of the prepared TiO_2 surface.

The EDX spectra of the anodized Ti foil, shown in Figure 4.3, reveals that the atomic Ti to O ratio was 36.6 : 63.6 corresponding to the pure TiO_2 phase.

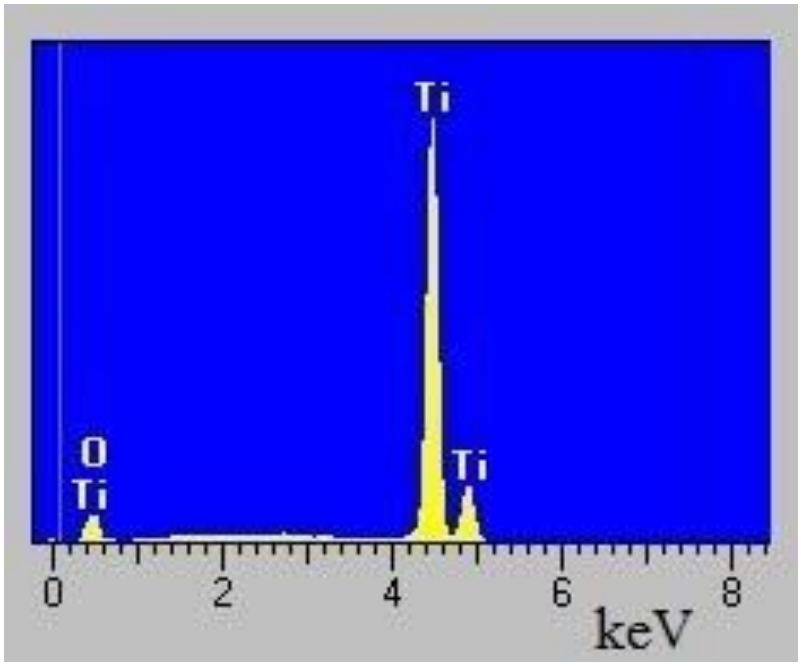

Figure. 4.3. The EDX spectra of as synthetized TiO_2.

The SEM image of SILAR deposited iron oxide on the synthesized TiO_2 substrate, are shown in Figure 4.4 (*note:* in the following text TiO_2-nanotubes structure will be denoted as TNT's and SILAR deposited iron oxide on TiO_2 as TNTF's). The average dimensions of the iron oxide deposits, which form practically isolated 2D islands, are between several μm and ~20 μm, while the thickness was estimated to be >1 μm, inset in Figure 4.4.

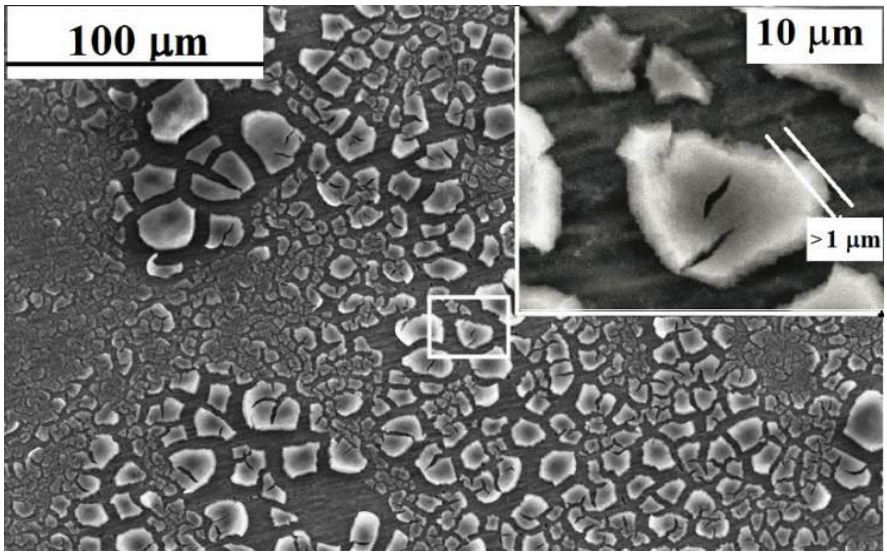

Figure 4.4. SEM image of SILAR depozited Fe_2O_3 on TiO_2-NT.

From the high-resolution SEM images, Figure 4.5, it can be concluded that TiO_2 nanotubes are not filled with iron oxides during the deposition processes. Although there is no clear evidence, it may be assumed that exposed TiO_2 NT's were also covered with the thin iron oxide film.

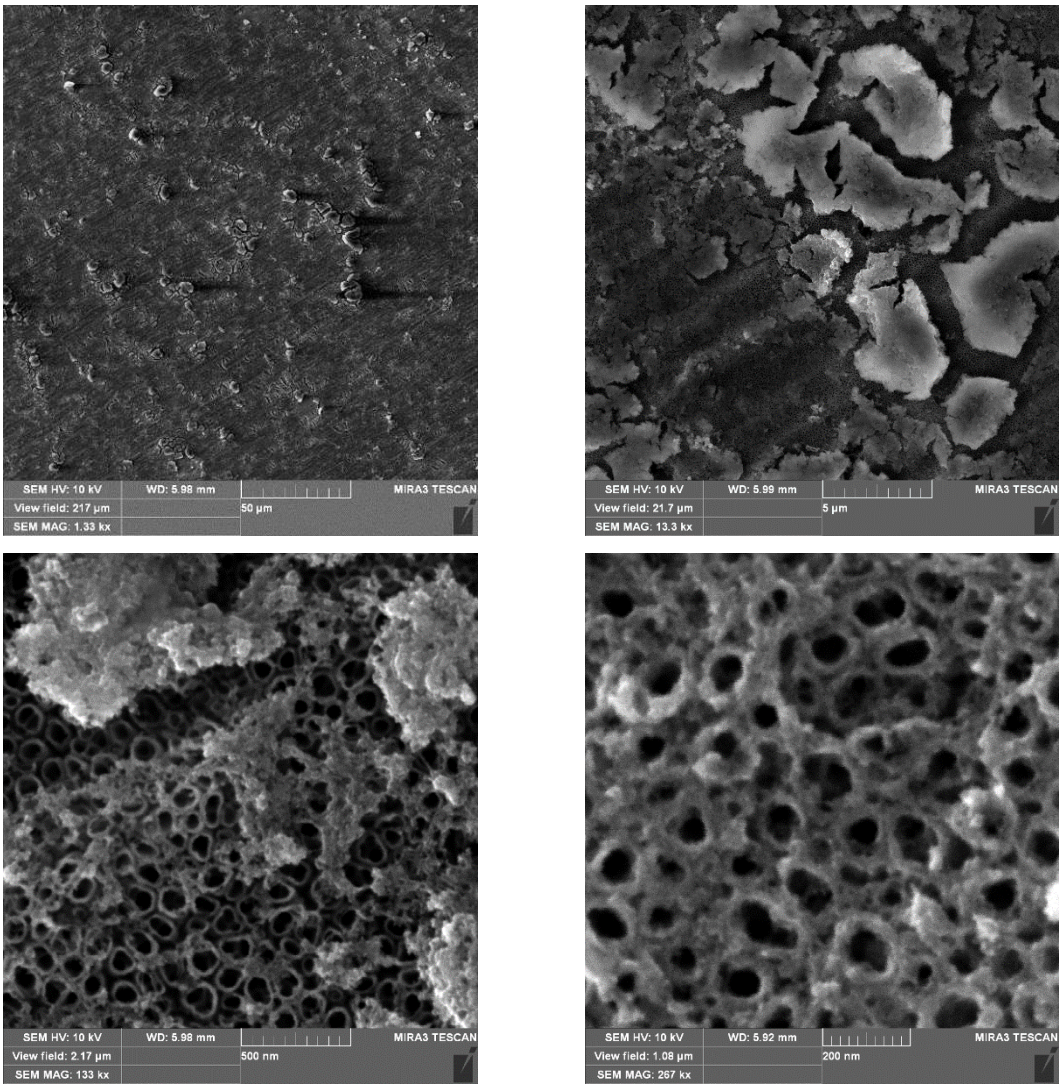

Figure 4.5. High resolution SEM imafes of SILAR deposited iron oxide on TiO_2

The EDS spectra of the TiO_2 modified with iron oxide, shown in Figure 4.6, had the following elemental composition: Ti- 39.68 wt.% (19.96 at.%); O- 50.28 wt.% (75.71 at.%) and Fe- 10.04 wt.% (4.33 at.%). Hence it can be concluded by comparing data with pure TiO_2 EDX spectra, that atomic iron to oxygen ratio is approximately 1:7, corresponded to hydrous iron oxide, ferrihydrite [114, 125].

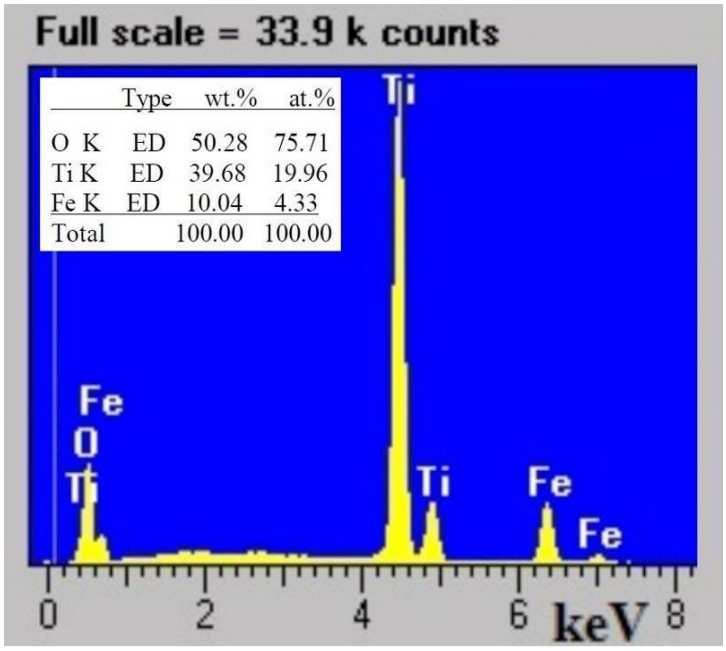

Figure 4.6. EDS spectra of the TiO_2 surface modified with iron oxide.

Figure 4.7 shows the XRD diffraction pattern of the synthesized iron oxide in powder form. The XRD spectra correspond to poorly crystalline, almost amorphous ferrihydrite [114,125]. After FFT-filtering and smoothing (thick black line), comparing the XRD pattern with standard cards of: goethite α-FeO(OH) (ICSD 28247), hematite α-Fe_2O_3 (ICSD 161294) and lepidocrocite γ-FeO(OH) (ICSD 247035), it might be carefully concluded that the product is a mixture of α(γ)-FeO(OH) and α-Fe_2O_3.

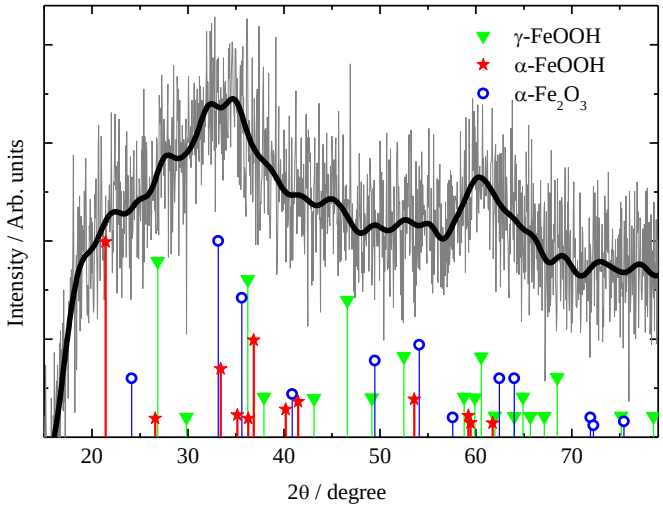

Figure 4.7. XRD spectra of the synthesized iron oxide sample, with corresponding standard intensities for γ-FeOOH (▼), α-FeOOH (★) and α-Fe_2O_3 (○).

Figure 4.8 shows the comparisons of XRD diffraction patterns of the as synthesized iron oxide, and after annealing treatment at the 450 ^{o}C for one hour. After annealing treatment in order to increase crystallinity (spectra b), and keeping in mind that annealing treatment does not disturb the original phase structure [114], few well defined XRD peaks appear. Using the program PowderCell [126], $_{i}$t is determined that sample contained ~99 wt.% of α-Fe_2O_3 phase. Using the Scherrer formula the mean crystallite size of α-Fe_2O_3 of 32.9 nm is valued. It should be mentioned that strong sample fluorescence is also detected. It is well known that fluorescence greatly contributes to the high intensity of the background of the diffractogram.

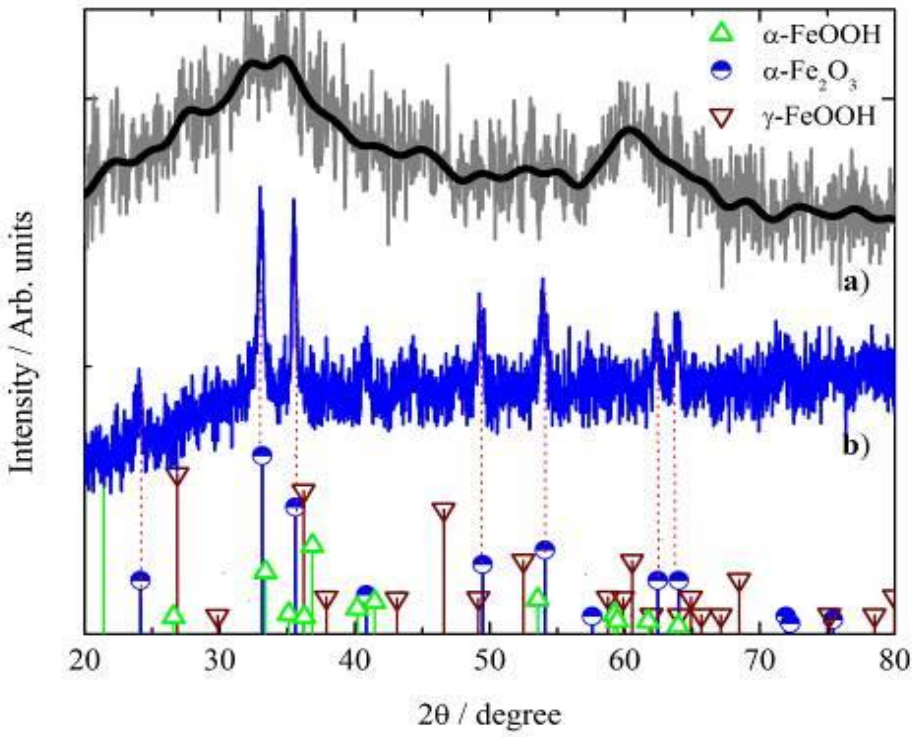

Figure 4.8. XRD pattern of the as synthetized bulk sample (a) and after annealing at 450 °C for one-hour (b).

The FTIR spectra of the synthesized powder sample are shown in Figure 4.9. Three intense absorption bands observed at 3440, 2923 and 1633 cm^{-1}, correspond to asymmetrical stretching vibration, symmetrical stretching vibration and deformation vibration of physically adsorbed H_2O molecules in the sample [125]. Traces of

unwashed nitrates from the precipitates were still visible at 1382 cm^{-1} [127]. The presence of a band at ~1460 cm^{-1} indicates that carbonate species were present on the surface, while the band at 1740 cm^{-1} can be associated with residues of methanol used for sample washing.

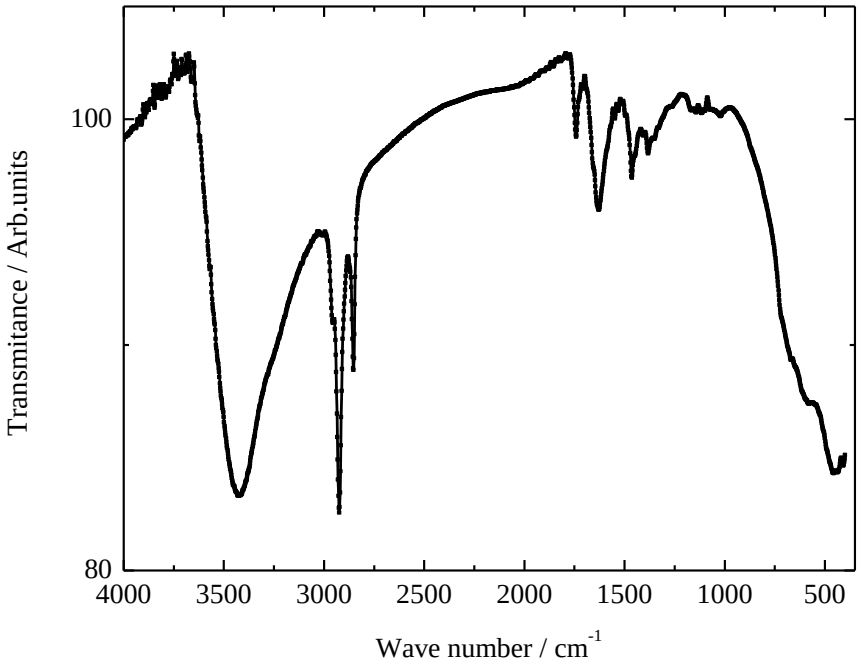

Figure 4.9. FTIR spectra of the synthesized iron oxide.

The magnified spectra, Figure 4.10, shows the IR band at 1147 cm^{-1}, 1019 cm^{-1}, and the shoulder at 729 cm^{-1}. The bands at 1147 cm^{-1} and 1019 cm^{-1} correspond to the γ -OH in-plane bending mode vibration, while the shoulder at 729 cm^{-1} corresponds to the out-of-plane bending vibration of Fe-O-O-H of lepidocrocite γ-FeO(OH) [127,128]. Two IR bands at 895 and 798 cm^{-1} characteristic for Fe–O–H bending vibrations in goethite, α-FeO(OH), structure were missing [125 129]. The presence of bends below ~700 cm^{-1} can be associated with the presence of hematite, α-Fe_2O_3. Iglesias and Serna [130] recorded IR bands at 575, 485, 385 and 360 cm^{-1} for α-Fe_2O_3 spheres, while the IR bands at 650, 525, 440 and 300 cm^{-1} were recorded for α -Fe_2O_3 laths.

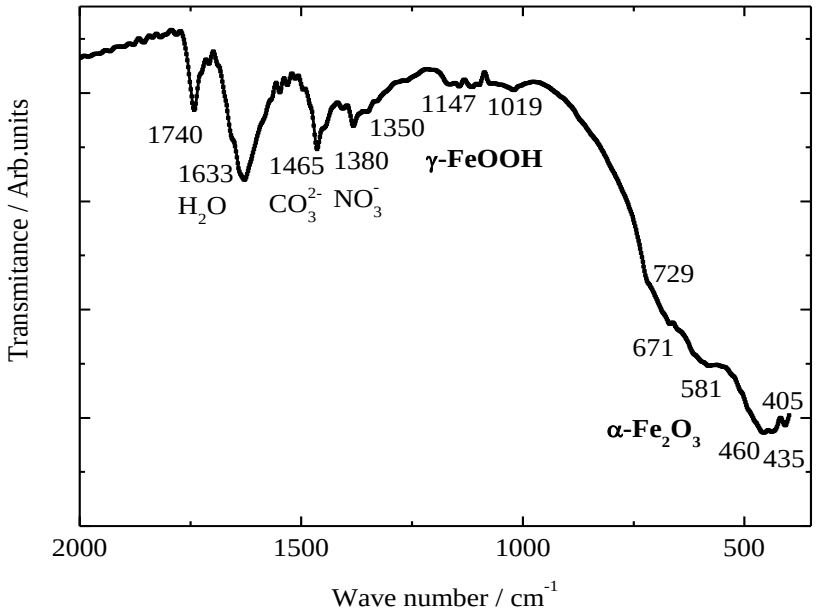

Figure 4.10. Magnified FTIR spectra of the synthesized iron oxide.

Hydrolysis of iron(III) solutions at ambient temperatures results in an amorphous precipitate of iron(III) hydroxide. This amorphous compound is, as all other amorphous precipitates, thermodynamically unstable and may gradually transform to goethite, α–FeO(OH), lepidocrocite, γ-FeO(OH) and hematite, α-Fe_2O_3. Time, temperature, pH [131], and in particular iron(III) concentration [128, 132], are the main parameters governing the rates of transformation to different crystalline phases. γ-Fe_2O_3 structure is metastable and converted from the alpha phase only at elevated temperatures. Goethite is formed at high pH values, while hematite is formed at medium to low pH values [132]. Based on the FTIR and XRD analysis, the main iron oxide species formed during these procedures at our pH~10 can be hematite. Cristino et al. [114] obtained similar results. The mechanism of the iron nitrate forced hydrolysis in the hypochlorite solution can be described by the following reactions:

$$Fe^{3+} + 3OH^- \rightarrow Fe(OH)_3 \quad (4.1)$$

$$Fe(OH)_3 \rightarrow \gamma(\alpha)\text{-}FeOOH + H_2O \quad (4.2)$$

$$2\gamma(\alpha)\text{-}FeOOH + 2OCl^- \rightarrow \alpha\text{-}Fe_2O_3 + O_2 + 2Cl^- + H_2O \quad (4.3)$$

4.2. Photoelectrochemical behavior

Figure 4.11 shows the photo-polarization curve of TNT's and TNTF's. TNT's show typical photo-response of a thermally untreated sample [96,133,134,135,136,].

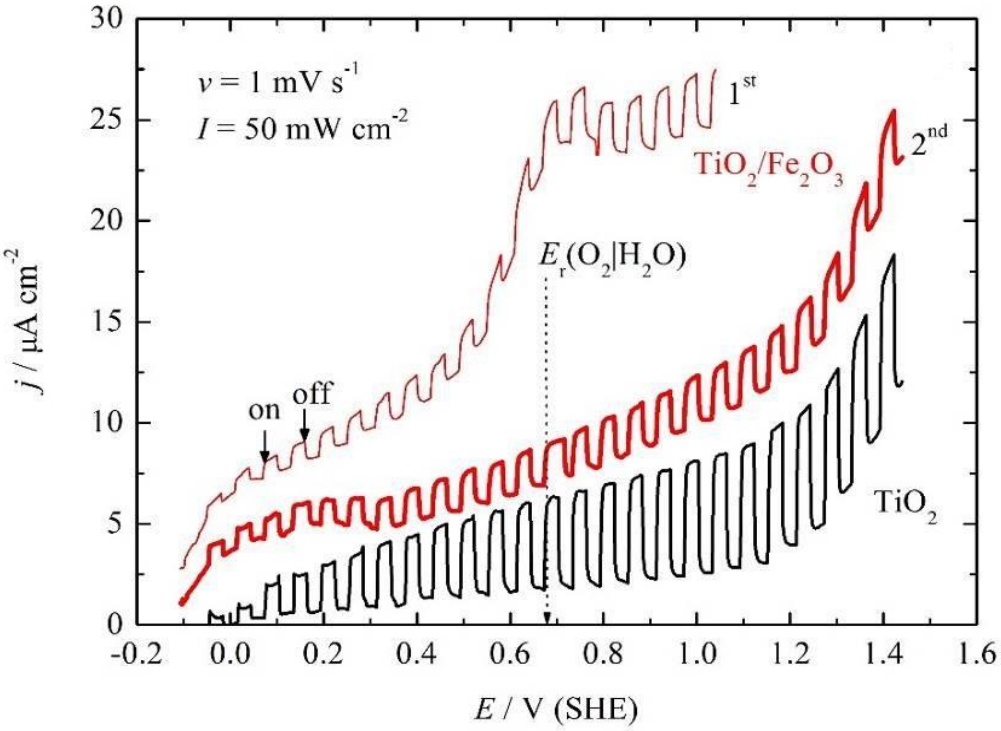

Figure 4.11. Pulse photo-polarization curve of TNT's and TNTF's electrode;

The TiO_2 nanotubes prepared according to the described procedure were amorphous in nature, but after annealing (under oxidizing conditions in air or O_2), they could be transformed to anatase or rutile, which significantly improved their photoelectrochemical activity [63]. In the first sweep, as synthesized TNTF's showed a considerably higher current density than the unmodified electrode. This could be associated with the phase transformations, probably dehydration, of the as deposited ferrihydrite onto surfaces, by so called electrochemical annealing. In the second, and the following sweeps, the reproducible polarization curves, under photo-pulsed Figure 3a) and steady state conditions, Figure 4.12 are obtained. From Figure 4.12 it can also be seen that the stable photocurrent on TNTF's is two times higher than on TNT's.

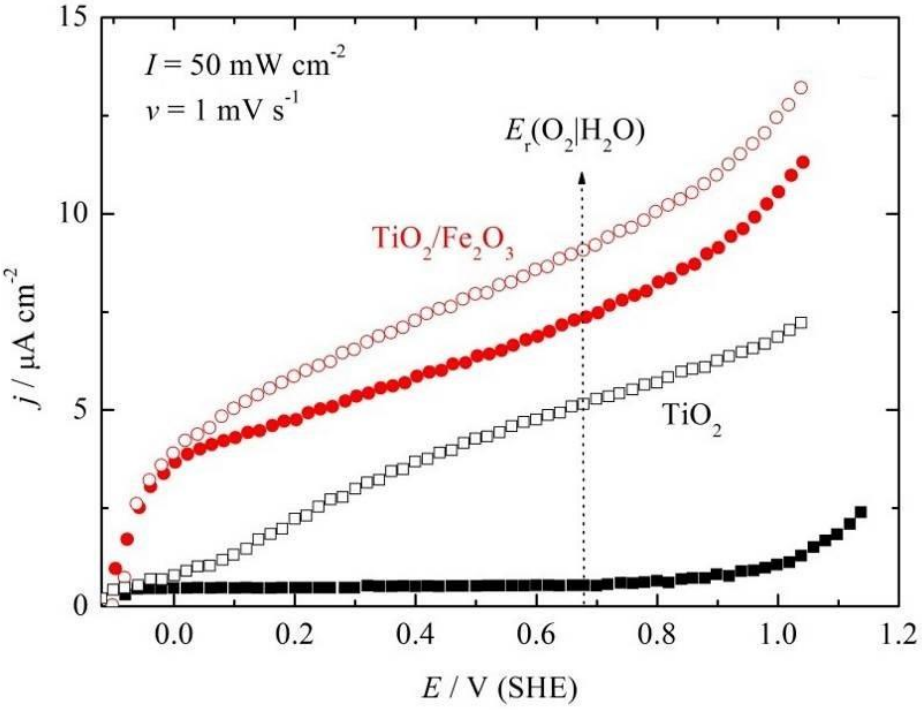

Figure 4.12. Potenciodynamic (v = 1 mV s^{-1}) polarization curves of TNT's and TNTF's electrode under dark (closed symbols) and pulsed light, 50 mW cm^{-2} (open symbols).

Figure 4.4 shows that the TiO_2 substrate is highly covered with iron oxide. Therefore, the photoelectrochemical measurements indicate that the deposited iron oxide film behaved as a semiconductor. At the same time, the dark current component was significant. This could be explained by the high density of defects and imperfections in the iron oxide structure, the formation of different surface states, and, accordingly, a high degree of the electron-hole pair recombination [137]. On the other hand, overshooting, which appears as a sparks during the light on-off switching, characteristics for the recombination process [138] is observed only on the TNT's in the low potential region, e.g. E<0.3 V, Figure 4.11. Hence, it can be concluded that the dark current density component, observed on TNTF's originated from the slow electrochemical oxidation reaction according to the following scheme [15]:

$$S + OH^- = S\text{-}(OH)_{ads} + e \quad (4.4)$$

$$S\text{-}OH_{ads} + OH^- = S\text{-}(H_2O_2)_{ads} + e \quad (4.5)$$

$$S\text{-}(H_2O_2)_{ads} + OH^- = S + HO_2^- + H_2O \quad (4.66)$$

where S represents the active surface centers.

In order to investigate steady state photo-response, electrodes are held at a potential of 0.75 V, Figure 4.13, where the oxygen evolution reaction is thermodynamically possible. When switching light on and off, both electrodes show typical n-type behavior, with very fast photoresponse without overshooting. The photocurrent density of ~4 μA cm^{-2} for TNT's and ~10.5 μA cm^{-2} for TNTF's, but with the dark current component of 8 μA cm^{-2}, were observed.

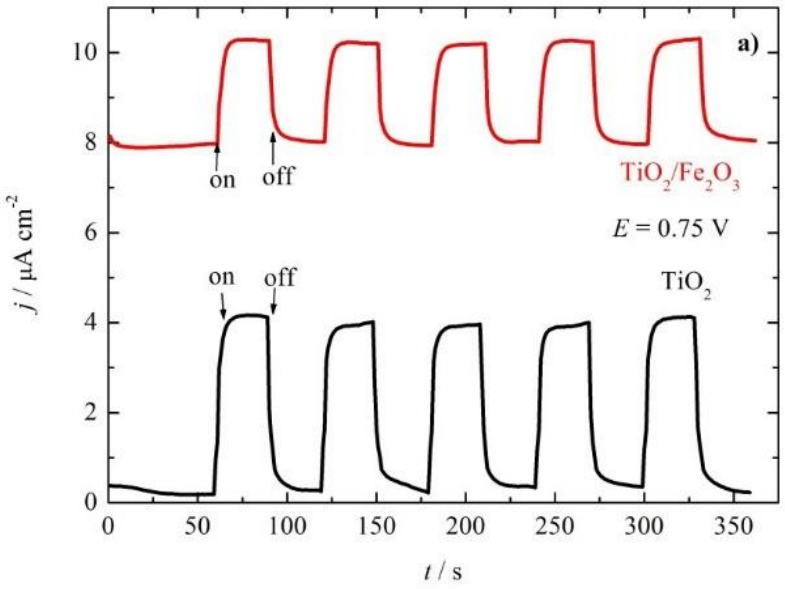

Figure 4.13. Potentiostatic photoresponse of TNT's and TNTF's electrodes.

When applying this current density (8 μA cm^{-2}), conditions were such as to ensure oxygen evolution on both electrodes in the dark Figure 4.14. Nevertheless, after illumination, a negative shift in the potentials, of -0.15 for TNT's and –0.26 V for TNTF's, is observed. Under these conditions, the potential of TNTF's is below reversible oxygen potential, but even then, it was by 0.73 V more negative than for the pure TNT's electrode. Consequently, a higher current should be applied to reach the thermodynamic potential of water decomposition.

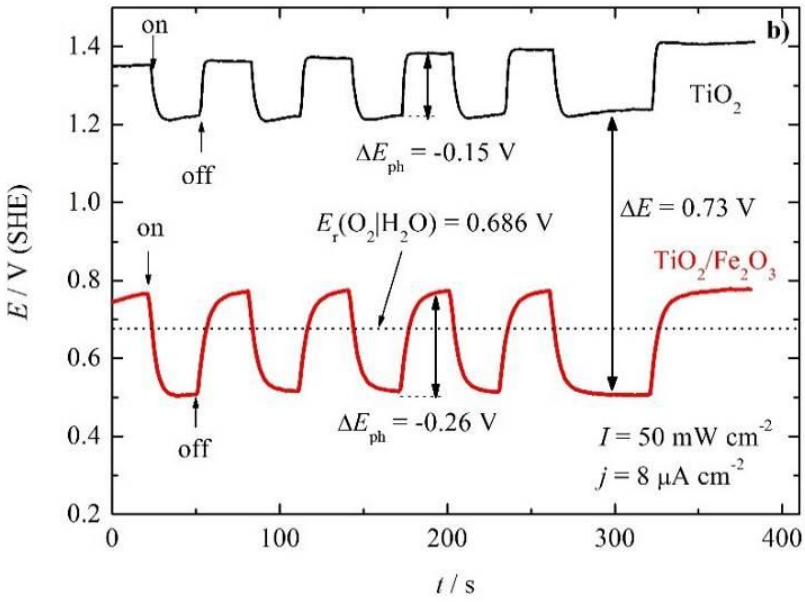

Figure 4.14. Galvanostatic photoresponse of TNT's and TNTF's electrodes.

Figure 4.15 shows the potentials and voltages for the investigated electrodes and platinum cathodes in PEC, under galvanostatic conditions with an external current density of 10 μA cm^{-2}. This current density is chosen because it is the minimal external current density at which water splitting could be theoretically obtained on a TNTF's electrode. Under the light, the potential of the TNTF's electrode was ~100 mV above oxygen reversible potentials, while the cathodic potential was shifted by ~200 mV in the negative direction. At the same time, the cell voltage of the PEC under light conditions with the TNTF's electrode is ~1.39 V, while with TNT's it is ~2.1 V. According to the structure of cell voltage given as:

$$U = U_0 + \Sigma\Delta E_{\pm} + I\Sigma R \qquad (4.7)$$

where U_0 is reversible cell voltage, e.g. 1.23 V, $\Sigma\Delta E_{\pm}$ is the sum of all anodic and cathodic polarizations (overpotentials), and $I\Sigma R$ is the sum of all Ohmic drops in PEC, the lower voltage of the TNTF's-based cell, is associated with the smaller anodic overpotentials. The energy consumption at the same current given as:

$$W = UIt \qquad (4.8)$$

will be by ~30% smaller in the PEC with the TNTF's anode than with TNT's anode; while the voltage efficiency of the PEC, defined as $\eta_U = U_0/U$, will be 88% for TNTF's and 58% for TNT's anode.

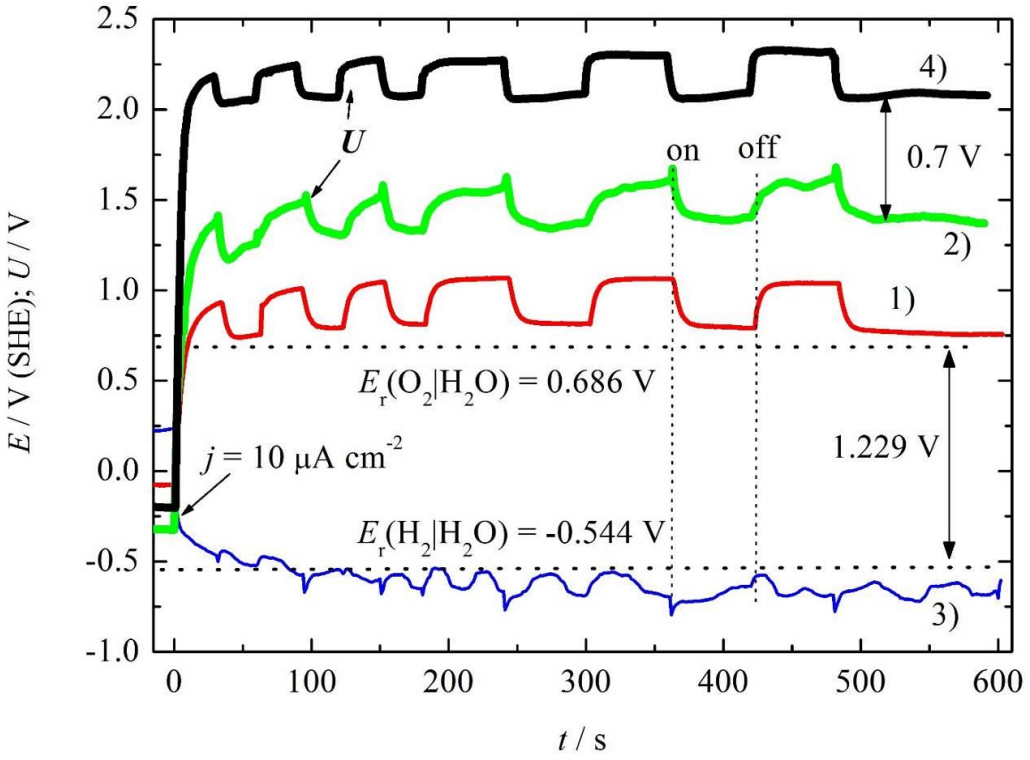

Figure 4.15. Potential (1) and voltage (2) for TNTF's anode and potential for Pt cathode (3), compared to the voltage for the TNT's anode (4), during PEC operation at the constant current density of 10 μA cm^{-2}, and light intensity of 50 mW cm^{-2}.

4.3. The proposed structure of the band gap and possible charge transfer reactions

Figure 4.16 shows the UV-vis spectra of colloidal particles in water. The estimated band gaps for pure TiO_2 of ~3.3 eV and Fe_2O_3 of 2.2 eV were in good agreement with the literature data. For the TiO_2 modified by Fe_2O_3 the band gap is estimated to be 2.5 eV, which is similar to the results reported by Kılıç et al. [24].

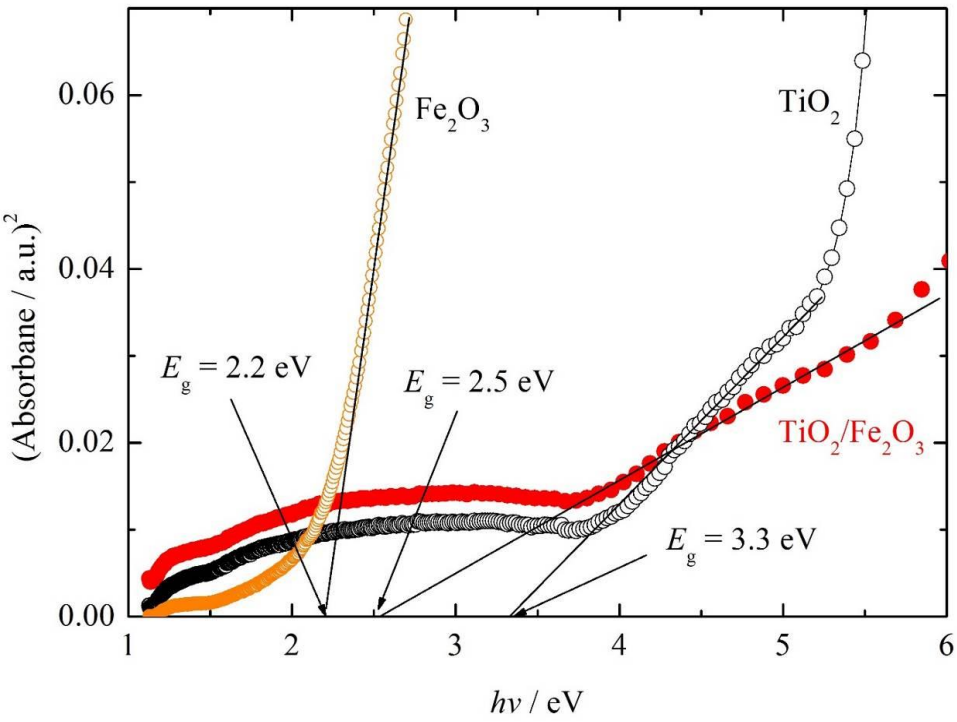

Figure 4.16. The dependence of the absorbance square on the light energy of colloidal particles in water.

Knowing the values of band gaps, the band gap diagram can be constructed by determining the flat-band potentials of the investigated systems. By applying a relatively simple procedure [139], the flat-band potentials are estimated by determining the open circuit potentials at different light intensities, as shown in Figure 4,17. The E_{ocp} of the TNT's electrode strongly depends on the light intensity, while the E_{ocp} of the TNTF's electrode depends on the light intensity to a lesser degree. By plotting the values of E_{ocp} over the reciprocal values of the light intensity and extrapolating the line

to the maximum light intensity ($I^{-1}\rightarrow 0$), the flat-band potentials of the TNT's electrode of -0.14 V, and for the TNTF's electrode of -0.1 V, are estimated, inset in Figure 4.17.

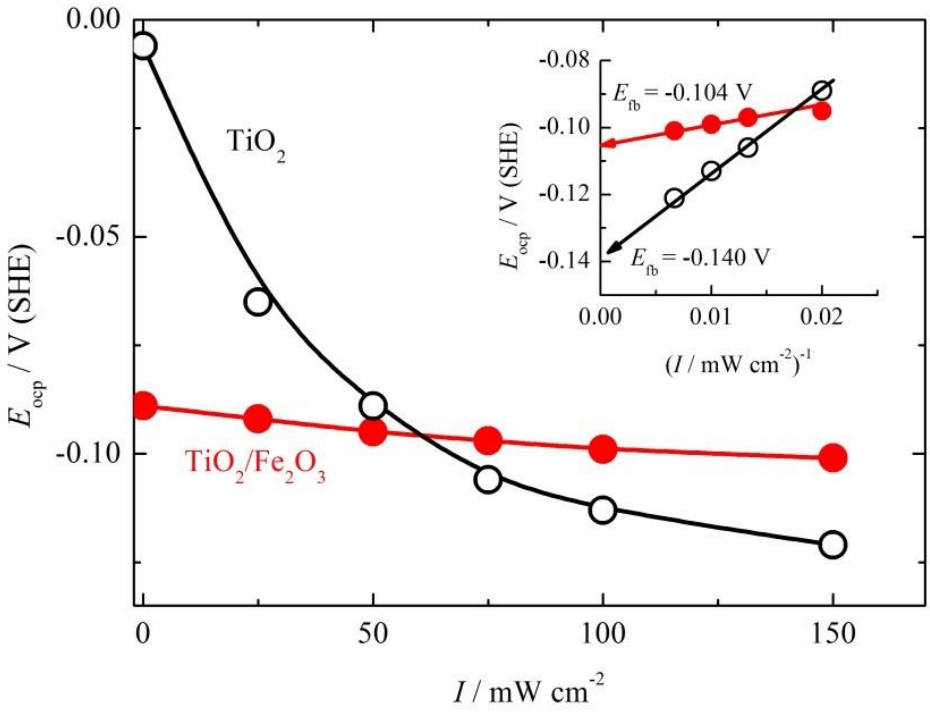

Figure 4.17. The dependence of the open circuit potentials on light intensity. Inset: the dependence of the open circuit potentials on the reciprocal values of light intensity.

In case of heavily doped n-type metal oxides, such as TiO_2, the conduction band edge, CB, position practically merged with the quasi-Fermi level, $|U_{CB} - E_F| < 0.1$ V [137,138,139]. Knowing the values of the band gap, flat-bend potentials, and assuming that the positions of conducting bands were >0.1 eV above the quasi-Fermi level, it is possible to construct a band gap diagram of the investigated materials. Figure 4.18 shows the structure of the band gap at open circuit potentials under the dark and maximum light intensity ($I\rightarrow\infty$), on the absolute vacuum, and the corresponding standard hydrogen scale, taking into account that 0 V SHE = –4.44 ±0.02 eV [39]. At increased light intensities, the shift of the TiO_2 Fermi level of is 0.14 eV, while at TiO_2/Fe_2O_3, it is only 0.04 eV. Therefore, under a moderate light intensity, e.g. in our

case 50 mW cm^{-2}, favorable positions of conduction bands for electron transfer can be achieved.

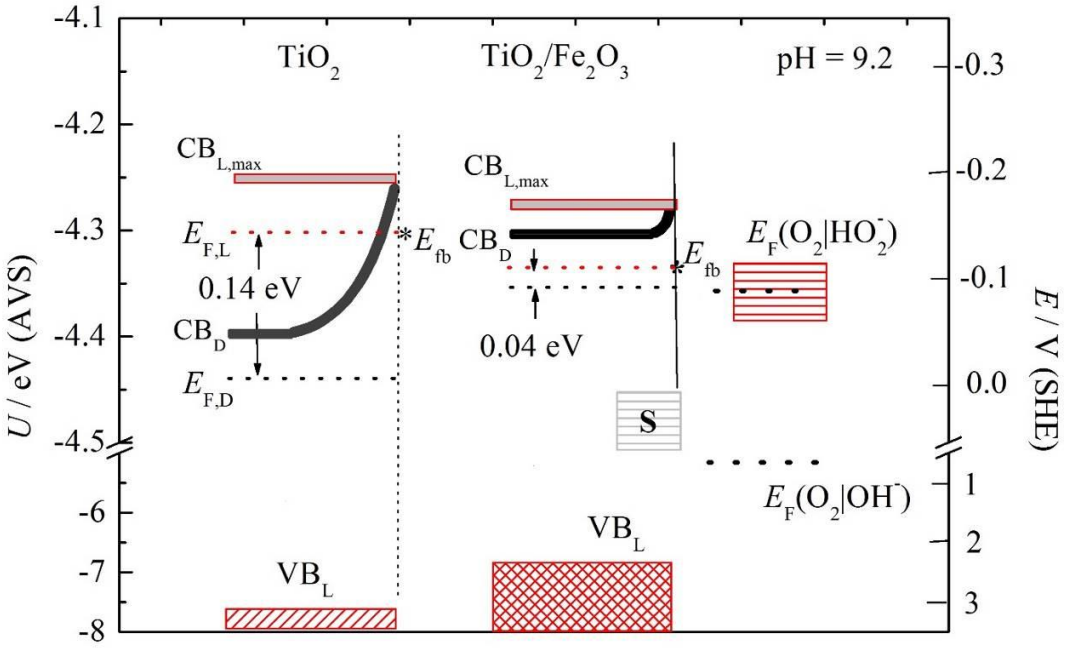

Figure 4.18. Proposed structure of the band-gap of TNT's and TNTF's at the open circuit potential under the dark and maximum light intensity. VB - valence band; CB - conducting band; E_F - Fermi level; $*E_{fb}$ – flat band potential; L - light; D – dark; S – surface state.

The Fermi level of the solution species can be assigned to the redox potential of hydrogen peroxide $E^{\theta}_{r}(O_2|HO_2^-) \approx -0.08$ V [140], because TiO_2 is reported to be a good selective catalyst for the oxygen reduction to hydrogen peroxide [141]. Under the light, in principle, both materials can produce *h-e* pairs, TiO_2 in UV and only Fe_2O_3 in visible, ~500 nm region. But due to the short hole diffusion length, 2−4 nm and short lifetime, in the bulk of Fe_2O_3, one should expect the produced holes to be short lived, and to rapidly recombine with excited electrons from the conducting band on the surface state (S), approximately shown in Figure 4.18 at the Fe_2O_3-electrolyte interface. Different role and the origins of the surface state in Fe_2O_3 are proposed, like oxygen vacancies, the crystalline disorder, or different iron oxidation states [142,143]. However, today, the prevalent mechanism is proposed to be hole trapping in the surface state, which leads to a prolonged lifetime and a better oxidation ability [109,144,145,146]. The reaction that occurred during hole trapping is probably [147]:

$$=Fe^{III}–O^{-} + h^{+} \rightleftarrows =Fe^{IV}=O \quad (9)$$

Hence, we can suggest a plausible mechanism that occurred during the anodic photo oxidation processes, under UV-vis light and applied anodic bias, E_a. The TiO_2 phase was highly covered with Fe_2O_3 (Figure 4.4) so, excitation of TiO_2 with UV light, in the first approximation, could be neglected. On the contrary, from Figure 4.5d it can be seen that TiO_2 nanotubes and Fe_2O_3 deposits are well separated. Accordingly, on the nanometric edge interphase between TiO_2 and Fe_2O_3, or eventually on TiO_2 nanotubes covered with a thin Fe_2O_3 film, charge carriers could be efficiently separated. Probably, the charge is accumulated on Fe_2O_3, because it can benefit from absorption of both UV and visible light producing hole-electron pairs. Consequently, one expects an additional negative shift of the bands, and better position for electron transfer. Holes from Fe_2O_3 VB could be trapped in the surface state, Eq. 4.9, leading to a prolonged lifetime. The formed electrons from Fe_2O_3 CB can be transferred to TiO_2 CB, and further to the external circuit and cathode, because the participation of TiO_2 was negligible and should work as a sink of electrons as in dye-sensitized solar cells. Trapped holes in the surface state, as an electron acceptors, may oxidize OH^- to different products depending on potentials: at low potentials to hydrogen peroxide ions, and at higher potentials to oxygen. Some degree of recombination, with the rate v_{rec}, should be expected, as well. For the sake of simplicity, in the mechanism, species $=Fe^{III}–O^{-}$ was denoted as S, and hole trapped state, $=Fe^{IV}=O$, with S*. The simplified mechanism is schematically presented in Figure 4.19, and with following reaction scheme.

At low potentials:

$$Fe_2O_3\text{-}S + h\nu \rightarrow Fe_2O_3\text{-}S^* + Fe_2O_3\text{-}CB(e) \quad (4.10)$$

$$Fe_2O_3\text{-}S^* + OH^- \rightarrow Fe_2O_3\text{-}S\text{-}OH_{ads} \quad (4.11)$$

$$Fe_2O_3\text{-}S^* + Fe_2O_3\text{-}S\text{-}OH_{ads} + OH^- \rightarrow Fe_2O_3\text{-}S + Fe_2O_3\text{-}S\text{-}(H_2O_2)_{ads} \quad (4.12)$$

$$Fe_2O_3\text{-}S\text{-}(H_2O_2)_{ads} + OH^- \rightarrow HO_2^- + H_2O + Fe_2O_3\text{-}S \quad (4.13)$$

During the photooxidation reaction, the intermediate species, physisorbed hydrogen peroxide, Eq 4.13, could desorb as OH_2^- ions, but it can also decompose to OH^* radicals or O_2. At higher potentials, the photo electrochemical formation of O_2, via overall reaction, may occur:

$$2Fe_2O_3\text{-}S^* + 2Fe_2O_3\text{-}S\text{-}(OH^-)_{ads} + 2OH^- \rightarrow 4Fe_2O_3\text{-}S + O_2 + 2H_2O \qquad (4.14)$$

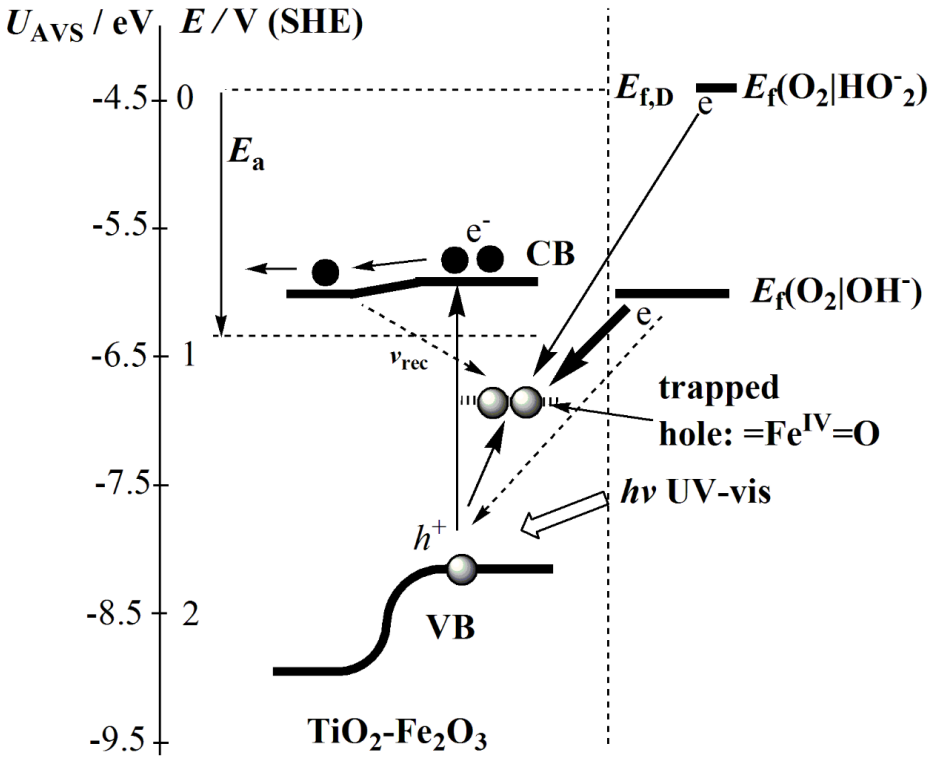

Figure 4.19. The plausible mechanism occurred during the anodic photo oxidation processes, at the applied anodic bias, E_a.

4.4. Urea photooxidation

4.4.1. Urea oxidation on platinum

In order to investigate the electrochemical urea oxidation, the reaction is first investigated on platinum electrode, and the results are shown in Figure 4.20. Without urea in solution, no activity is observed below potential of ~0.8 V (SCE). Above that potential, the oxygen evolution reaction occurred:

$$4OH^- \rightarrow O_2 + 2H_2O + 4e \qquad E_r = 0.93 \text{ V (SCE)} \tag{4.15}$$

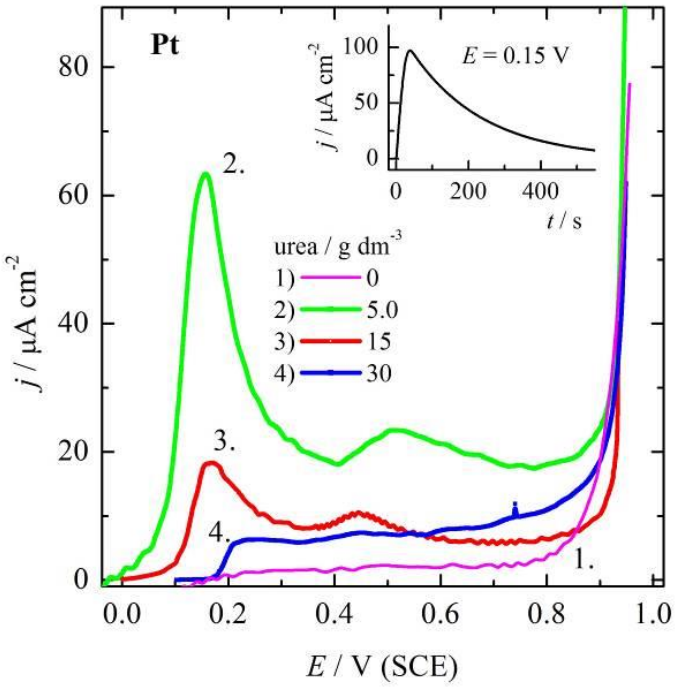

Figure. 4.20. Linear anodic polarization curves (v = 1 mV s^{-1}) of the urea oxidation, in the concertation range from 0-30 g dm^{-3}, onto platinum electrode (A=1 cm^2) at room temperature in the electrolyte containing 0.1 M Na_2SO_4 buffered with 0.05 M borax to pH = 9.2. Inset: potentiostatic pulse at 0.15 V in electrolyte containing 5 g dm^{-3} urea.

In the presence of 5 g dm^{-3} urea in solution, the oxidation starts at low potentials of –0.05 V (SCE). The oxidation occurred up to the potential of 0.15 V (SCE) reaching the

maximum current density of 65 μA cm^{-2}, followed by decreased activity at higher potentials. Some additional small activity is observed in the potential range of 0.4 V to 0.75 V. Above 0.9 V the activity is practically identical to platinum without urea in solution. The observed activity at low potentials can be associated with transition phenomena, because under steady state conditions activity rapidly decreases over time, as shown in inset of Figure 4.20. Through the increasing the concentration of the urea to 15 g dm^{-3} the activity decrease for three times, and in solution contained 30 g dm^{-3} of the urea, the activity is insignificant, below potentials of ~0.9 V (SCE).

Using the *in situ* FTIR spectroscopy, Bezerra et al. [148], investigated the adsorption and oxidation of the urea on platinum in different pH of the electrolytes. They found that surface urea adsorbates and the reaction products are dependent on pH of the solutions. At low pH values, *e.g.* in 0.1 M $HClO_4$, the main detected oxidation product is CO_2, while adsorption of the urea occurred through nitrogen atoms with loss of two hydrogen atoms, followed by the formation of CO due hydrolysis. In the neutral solutions, *e.g.* 0.1 M KF, the urea adsorption in the double layer proceed with the formation of CNO^- and $[N_2O_2]^{2-}$, and at higher potentials the main detected oxidation products are NO_2 and NO_3^-. In the alkaline solutions, *e.g.* 0.1 M KOH, the urea is adsorbed depending on the potentials via NH_2 group at low potentials and via oxygen atoms at higher potentials. The oxidation products were not reported or proposed.

Thus, based on these results it could be suggested that oxidation of the urea onto platinum occurred via the surface heterogeneous Langmuir–Hinshelwood kinetics [149]. Namely, the reaction involved chemical reaction between adsorbed species onto the surface can be given by the following reaction scheme:

$$Pt + OH^- \rightarrow Pt\text{-}(OH)_{ads} + e \quad (4.16)$$

$$Pt + CH_4N_2O \rightarrow Pt\text{-}(CH_4N_2O)_{ads} \quad (4.17)$$

$$Pt\text{-}(OH)_{ads} + Pt\text{-}(CH_4N_2O)_{ads} \rightarrow \text{products} \quad (4.18)$$

Assuming that the rate determining is step given by Eq. 4.18, the rate of the reaction can be given as:

$$r = k\theta(OH)\theta(CH_4N_2O) \quad (4.19)$$

where k is the apparent rate constants, and θ surface coverage of the reacting species. It is obvious that the reaction occurred as competitive surface adsorption, for which the maximum rate is under conditions that $\theta(OH) = \theta(CH_4N_2O) = 0.5$. By increasing the $\theta(CH_4N_2O)$, the reaction rate decrease and practically stops when $\theta(CH_4N_2O) \rightarrow 1$. So, increasing the concentration of the urea in solution the rate of the adsorption reaction step, Eq. 4.17, increased and the rate of the overall reaction decreased.

4.4.2. The photo-electrooxidation of the urea onto TiO_2 modified by hematite

In Figure 4.21 the photo-pulsed polarization curves for pure TiO_2-NT's and hematite modified electrode in the supporting electrolyte, are shown. From the inset in Figure 4.21, because both electrodes shows decrease of the open circuit potentials in negative direction after illumination, it can be concluded that electrodes behave as *n*-type semiconductor.

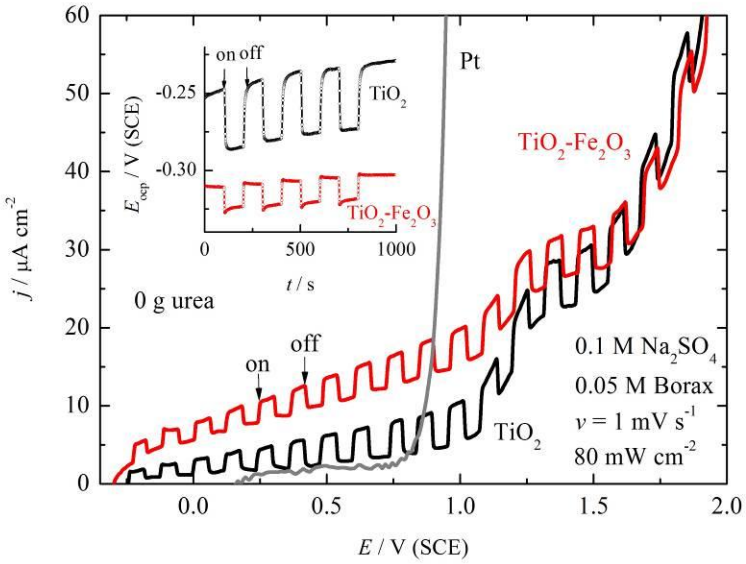

Figure 4.21. Photo-pulsed (light on-off) polarization curves (v = 1 mV s^{-1}) of TiO_2-NT's and hematite modified electrode (A=2 cm^2) in the supporting electrolyte (0.1 M Na_2SO_4 buffered with 0.05 M borax to pH = 9.2). Inset: The dependence of the open circuit potentials over time under dark and light conditions.

From Figure 5, it can be seen that both electrodes show photo activity in the anodic direction, from the open circuit potentials. TiO_2-NT's show characteristic photo-response of a thermally untreated sample. The TiO_2 nanotubes prepared according to the described procedure are amorphous in nature, but after further annealing treatment (under oxidizing conditions in air or O_2), they are transformed to anatase or rutile, which can significantly improve their photo-electrochemical activity. The dark current is higher on the modified electrode, and can be connected with the oxidation of OH^- ions to the hydrogen peroxide ions, according to the previously described electrochemical route:

$$S + OH^- = S\text{-}(OH)_{ads} + e \quad (4.20)$$

$$S\text{-}OH_{ads} + OH^- = S\text{-}(H_2O_2)_{ads} + e \quad (4.21)$$

$$S\text{-}(H_2O_2)_{ads} + OH^- = S + HO_2^- + H_2O \quad (4.22)$$

Under illumination the photocurrent is of the same magnitude as for pure TiO_2-NT's, and reaction can be given as:

$$Fe_2O_3\text{-}S + h\nu \rightarrow Fe_2O_3\text{-}S^* + Fe_2O_3\text{-}CB(e) \quad (4.23)$$

$$Fe_2O_3\text{-}S^* + OH^- \rightarrow Fe_2O_3\text{-}S\text{-}OH_{ads} \quad (4.24)$$

$$Fe_2O_3\text{-}S^* + Fe_2O_3\text{-}S\text{-}OH_{ads} + OH^- \rightarrow Fe_2O_3\text{-}S + Fe_2O_3\text{-}S\text{-}(H_2O_2)_{ads} \quad (4.25)$$

$$Fe_2O_3\text{-}S\text{-}(H_2O_2)_{ads} + OH^- \rightarrow HO_2^- + H_2O + Fe_2O_3\text{-}S \quad (4.27)$$

where S represents the active surface centers (species, $=Fe^{III}–O^-$), S^* iron oxide oxidized surface states (species, $=Fe^{IV}=O$) in which holes are trapped, and CB is conducting band of hematite.

Increased electrochemical and photoelectrochemical activity of TiO_2-NT's hematite modified electrode is explained in more details in previous discussion. Briefly summarizing, on the nanometric interphase edges between TiO_2 and Fe_2O_3, or eventually on the TiO_2 nanotubes covered with a thin nanometric Fe_2O_3 film, charge carriers could be efficiently separated. Possibly, the charge is accumulated on Fe_2O_3, because it can benefit from absorption of both visible and UV light, due smaller band gap of ~2.2 to 2.6 eV than TiO_2 of ~3.2 eV, producing hole-electron pairs. Holes from

Fe_2O_3 valence band could be trapped in the surface state, leading to a prolonged lifetime and better oxidation ability. Trapped holes in the surface state, as an electron acceptors, may oxidize OH^- to different products depending on potentials: at low potentials to hydrogen peroxide ions, and at much higher potentials to oxygen. The formed electrons from Fe_2O_3 conducting band can be relocated to TiO_2 conducting band, and further to the external circuit and cathode. The contribution of TiO_2 in the light absorption could be neglected, and should serve as a sink of the electrons as in dye-sensitized solar cells.

Figure 4.22 shows photo-pulsed polarization curves of TiO_2-NT's-hematite modified electrode in the urea contained electrolyte. It can be seen that with increasing the urea concentration both dark and light current increase as well. From the inset of Figure 4.22 which shows the comparison of the pulsed and continuous light on or off polarization curves, one can see that the same activity is obtained, consequently the photooxidation should not be connected with some transition phenomena during the switching light on or off. Under constant potential, reaction order based on the urea concentration is determined to be ~0.4 for both light and dark conditions (results are not shown).

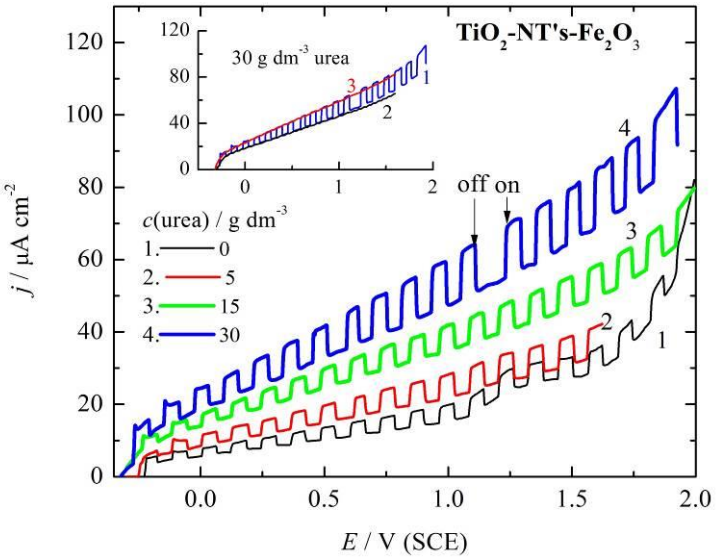

Figure 4.22. Photo-pulsed (light on-off) polarization curves (v = 1 mV s^{-1}) of TiO_2-NT's-hematite modified electrode (A=2 cm^2) in the urea (concentrations marked in the figure) containing 0.1 M Na_2SO_4 buffered with 0.05 M borax to pH = 9.2 electrolyte. Inset: The comparison of the pulsed (1) and continuous polarization curves with light off (2) or on (3).

In Figure 4.23 the polarization curves of TiO_2-NT's-hematite modified electrode in the urea contained electrolyte with different concentrations, under constant light on or off conditions are shown. From the figure can be seen that modified electrode possesses better activity for the urea oxidation than pure TiO_2-NT's electrode and Pt electrode at potentials negative than 0.9 V, which are shown for comparison. The current density under dark conditions at constant potential increased with increased urea concentration, and additionally for ~30% under light conditions. Hereafter, the electrooxidation of the urea on TiO_2-NT's-hematite modified electrode can be considered as a photo-assisted electrochemical reaction.

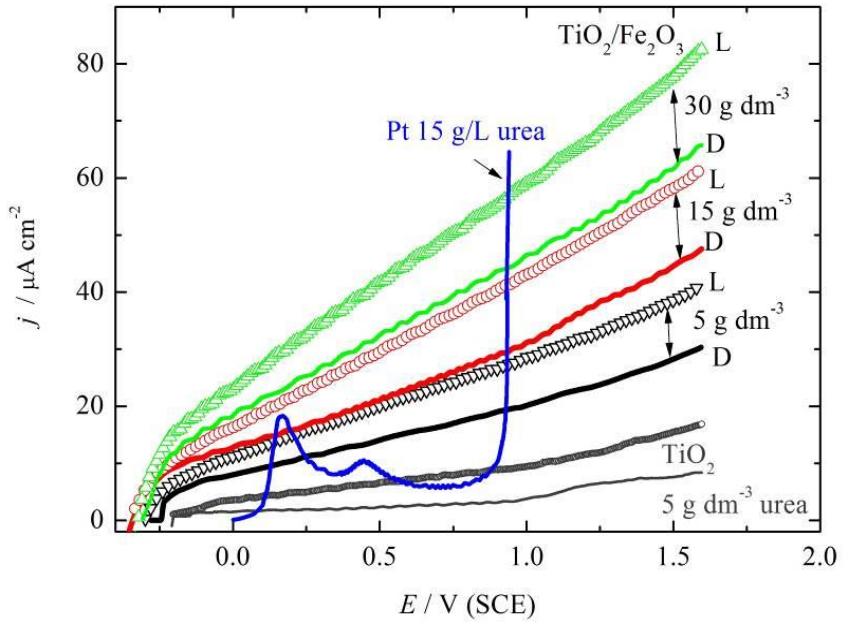

Figure 4.23. The polarization curves (v = 1 mV s^{-1}) under constant light on (L) or off (D) conditions of TiO_2-NT's-hematite modified electrode (A=2 cm^2) in the urea (concentrations marked in the figure) contained 0.1 M Na_2SO_4 buffered with 0.05 M borax to pH = 9.2 electrolyte, in comparison with pure Pt (A=1 cm^2) and pure TiO_2-NT's (A= 2 cm^2).

In accordance with the above shown mechanism, Eqs 4.23-4.27, for the overall reaction the photo-activity of the modified electrode could be described with the following equation:

$$Fe_2O_3\text{-}S^* + 3OH^- \rightarrow HO_2^- + H_2O + Fe_2O_3\text{-}S + e \qquad (4.28)$$

and it could be proposed that urea photo-assisted oxidation, proceeded by the chemical oxidation with adsorbed hydrogen peroxide or with hydrogen peroxide ions near the electrode surface:

$$HO_2^- + CH_4N_2O \rightarrow \text{products} \qquad (4.29)$$

For the purpose of this work the nature of the products was not investigated.

To test the initial stability, the TiO_2-NT's-hematite modified electrode is subjected to the galvanostatic and potentiostatic polarization under pulsed light on and off conditions over time. At a constant current density of 45 μA cm^{-2}, Figure 4.24a, the potential under dark is ~1.1 V and after illumination as low as 0.55 V, suggesting the successful separation of the electron-hole pairs onto a modified electrode.

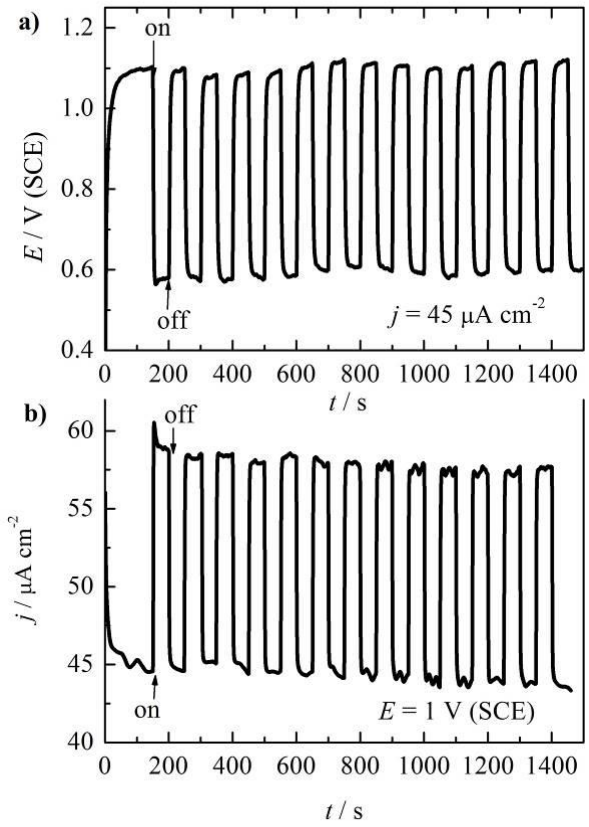

Figure 4.24. The galvanostatic (a) and potentiostatic (b) polarization of TiO_2-NT's-hematite modified electrode (A=2 cm^2) under pulsed light on and off conditions over time in 0.1 M Na_2SO_4 buffered with 0.05 M borax to pH = 9.2 electrolyte containing 30 g dm^{-3} urea.

The potential does not vary over time significantly. Under the potentiostatic conditions, Figure 4.24b, at 1 V the dark current was ~45 μA cm^{-2}, while under light conditions 58 μA cm^{-2} or 27% higher. Some small deterioration of the characteristics over time is observed.

4.5. Possible application of the urea oxidation reaction

As mentioned in the Introduction, the urea could be used as good energy carriers during the water electrolysis or in the fuel cells. In Figure 4.25 the structure of the potentials during anodic oxidation of 30 g dm^{-3} of urea on Pt and TiO_2-NT's-hematite modified electrode, converted to electrode area of 1 m^2, as well as a polarization curve for hydrogen evolution reaction on the stainless steel electrode is shown.

The structure of the cell voltage can be given as:

$$U_{cell} = U_0 + \Sigma|\eta_{\pm}| + I\Sigma R_{\Omega} \tag{4.30}$$

where U_0 is the reversible cell voltage ($U_o = E_a - E_c$), $\Sigma\eta_{\pm}$ is the sum of the absolute values of the cathodic and anodic overpotentials, and $I\Sigma R_{\Omega}$ the sum of all Ohmic drops in the cell.

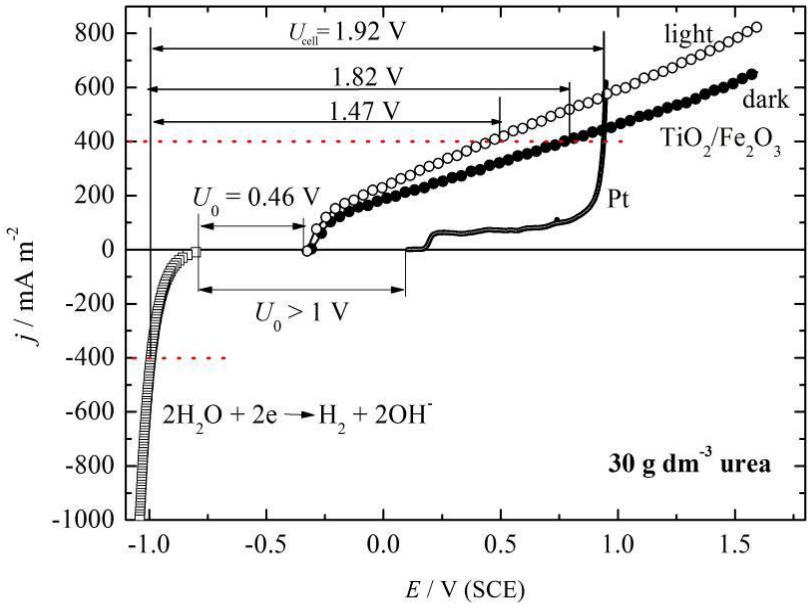

Figure 4.25. The structure of the cell voltage for 30 g dm^{-3} urea in the anodic oxidation on Pt (—), and TiO_2-NT's-hematite electrode under dark (●) and light conditions (○), and hydrogen evolution reaction on the stainless steel electrode as cathodic reaction (□) in the 0.1 M Na_2SO_4 buffered with 0.05 M borax to pH = 9.2 electrolyte. Electrodes area are converted to 1 m^2.

The obtained open circuit voltage of the cell for hydrogen production and urea oxidation with TiO_2-NT's-hematite electrode is ~0.46 V, and with platinum anode >1 V. Also, the electrolysis cell voltage, for example, at 0.4 A m^{-2} is 1.92 V for Pt anode, 1.82 V for TiO_2-NT's-hematite anode under dark, or 1.47 V under light conditions, or 30% smaller energy consumption, $w = UIt$, than with the platinum anode. This analysis clearly shows that TiO_2-NT's-hematite electrode possess much smaller anodic overpotential, than Pt electrode. With further optimization, for example, using the thermally treated TiO_2-NT's-hematite anode, such systems could be considered as a good catalytic materials for photo assisted electrolysis of water solutions containing urea with near neutral pH. This observations is very encouraging, because the main limit of the photo-electrochemical cells is dysfunctionality without external light sources, which increase operational cost without Sun during the night. The TiO_2-NT's-hematite anode could operate in the dark and with increased efficiency in the light conditions. Hence such a cell will not necessary require an external light source. Also, the anode can operate in the near neutral solutions, so the modification of the waste water composition by the means of increasing pH is not required.

In order to simulate possible cell voltage and the power of the fuel cell, in Figure 4.26a the polarization curves of the urea oxidation (under dark and light conditions) on TiO_2-NT's-hematite electrode as anodic reaction, and oxygen reduction from the air on platinum as the cathodic reaction is shown. Figure 4.26b shows the simulated voltage-current density curve for the possible fuel cell. It can be seen that the open circuit voltage was ~0.6 V, and operating voltage of 0.4 to 0.2 V is obtained for the ranges of the current density of ~25 to 150 mA m^{-2}. The maximum power density (Figure 4.26b) for the fuel cell is 22 mW m^{-2} under dark and 28 mW m^{-2} under light conditions.

This result also indicated that with further optimization of TiO_2-NT's-hematite anode, such cell could be used for simultaneous urea degradation and electricity production, in both light and dark conditions.

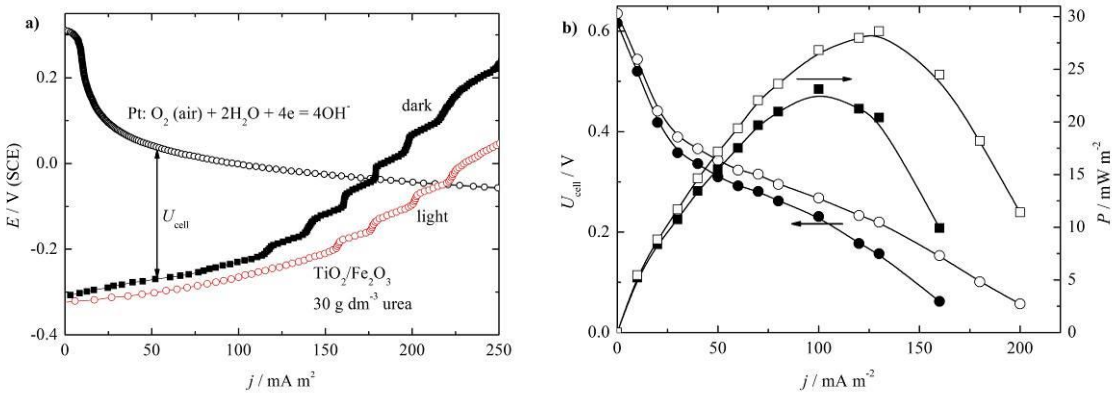

Figure 4.26. a) Polarization curves of the oxygen (from air) reduction on the Pt electrode, and 30 g dm^3 urea oxidation on TiO_2-NT's-hematite under dark and light conditions. b) The dependence of the cell voltage (left), and power density (right) on current density, under dark-full symbols, and light-open symbols. 0.1 M Na_2SO_4 buffered with 0.05 M borax to pH = 9.2 electrolyte, electrodes area are converted to 1 m^2.

5. CONCLUSIONS

The study shows that the fast forced hydrolysis of iron(III) nitrate in a hypochlorite solution at room temperature, can lead to the formation of hematite, α-Fe_2O_3. By applying this reaction in successive ion adsorption and reaction (SILAR) on an electrochemically formed TiO_2 nanotube electrode, a successful modification of TiO_2 with micrometric 2D α-Fe_2O_3 islands were achieved. This electrode shows better anodic photoelectrochemical characteristics than pure TiO_2 NT's. It is also shown that energy consumption at the same current in case of PEC with TiO_2 modified with an α-Fe_2O_3 anode will be by ~30% lower than in a pure TiO_2 NT's anode, while the voltage efficiency of the PEC, will be 88% and 58%, respectively. The following explanation of the improved characteristics of TiO_2 modified with α-Fe_2O_3 anode was suggested. The TiO_2 phase was highly covered with Fe_2O_3 so, excitation of TiO_2 with UV light, could be neglected. But, on the nanometric TiO_2-Fe_2O_3 edge interfaces, or eventually on TiO_2 nanotubes covered with a thin Fe_2O_3 film, electron-hole pairs could be formed in Fe_2O_3 phase under both UV and visible lights. Holes from Fe_2O_3 valence band can be trapped in the surface state, leading to a prolonged lifetime. The formed electrons from Fe_2O_3 CB can be transferred to TiO_2 CB, and further to the external circuit and cathode, because the participation of TiO_2 was negligible and should work as a sink of electrons as in dye-sensitized solar cells. It should be suggested that optimizations, such as the number of SILAR cycles, thermal treatment, etc. could further improve photoelectrochemical characteristics of TiO_2 nanotube electrode modified with α-Fe_2O_3.

It is also concluded that anodically formed titanium dioxide in the shape of nanotubes modified by hematite using the successive ion layer adsorption and reaction (SILAR) method could be used as anode in the reaction of the urea oxidation. The electrode shows increased electrocatalytic activity in comparison with pure platinum anode in

near neutral solutions (which are the typical conditions of the waste waters containing urea) under the dark conditions. Further improvement of the electrocatalytic behavior is observed under the electrode illumination by the light, in the so called photo assisted oxidation reaction. The possible applications of the photo assisted reaction using urea as the energy carriers are considered. It was shown that in the reaction of water electrolysis with simultaneous oxidation of urea and hydrogen production, the energy efficiency will be 30% smaller than with platinum anode. The photo-electrochemical fuel cell using oxygen reduction as a cathodic reaction is also considered with encouraging results. The open circuit voltage will be above 0.6 V, and operating cell voltage among 0.4 to 0.2 V. It is important to notice that both presented applications does not require modification of the electrolyte by the means of pH increase above 12, due strong corrosion of the previously reported behavior of the anodic materials based on the nickel and cobalt.

REFERENCES

[1] M.D. Archer, A.J. Nozik, eds. Nanostructured and Photoelectrochemical Systems for Solar Photon Conversion, in Series on Photoconversion of Solar Energy — Vol. 3, Imperial College Press, Covent Garden, London, 2008.

[2] X. Chen, C. Li, M. Grätzel, R. Kostecki, S.S. Mao Nanomaterials for renewable energy production and storage, Chem. Soc. Rev., 41 (2012) 7909–7937.

[3] L. J. Minggu, W.R.W. Daud, M.B. Kassim, An overview of photocells and photoreactors for photoelectrochemical water splitting, Int. J. Hydrogen Energy 35 (2010) 5233-5244.

[4] A. Kudo, Photocatalysis and solar hydrogen production, IUPAC, Pure Appl. Chem. 79 (2007) 1917–1927.

[5] A.J. Nozik, R. Memming, Physical chemistry of semiconductor-liquid interfaces, J. Phys. Chem. 100 (1996) 13061-13078.

[6] T. Bak, J. Nowotny, M. Rekas, C.C. Sorrell, Photo-electrochemical hydrogen generation from water using solar energy. Materials-related aspects, Int. J. Hydrogen Energy 27 (2002) 991–1022.

[7] X. Chen, S. Shen, L. Guo, S. S. Mao, Semiconductor-based photocatalytic hydrogen generation, Chem. Rev. 110 (2010) 6503–6570.

[8] Choudhary, S. Upadhyay, P. Kumar, N. Singh, V.R. Satsangi, R. Shrivastav, S. Dass, Nanostructured bilayered thin films in photoelectrochemical water splitting: A review, Int. J. Hydrogen Energy 37 (2012) 18713-18730.

[9] J. Sun, D.K. Zhong, D.R. Gamelin, Composite photoanodes for photoelectrochemical solar water splitting, Energy Environ. Sci. 3 (2010) 1252–1261.

[10] D.A. Wheeler, G. Wang, Y. Ling, Y. Li, J.Z. Zhang, Nanostructured hematite: synthesis, characterization, charge carrier dynamics, and photoelectrochemical properties, Energy Environ. Sci., 5 (2012) 6682–6702.

[11] M. Mishra, D-M Chun, α-Fe2O3 as a photocatalytic material: A review, Appl. Catal. 498 (2015) 126–141.

[12] K. L. Hardee, A.J. Bard, Semiconductor electrodes V. The application of chemically vapor deposited iron oxide films to photosensitized electrolysis. J. Electrochem. Soc. 123 (1976) 1024-1026.

[13] B. Iandolo, B. Wickman, I. Zorić, A. Hellman, The rise of hematite: origin and strategies to reduce the high onset potential for the oxygen evolution reaction, J. Mater. Chem. A 3 (2015) 16896–16912.

[14] X. Zhang, H. Li, S. Wang, F-R. F. Fan, A.J. Bard. Improvement of hematite as photocatalyst by doping with tantalum, J. Phys. Chem. C, 118 (30) (2014) 16842-16850.

[15] Q. Liu, A.M. Asiri, X. Sun, Hematite nanorods array on carbon cloth as an efficient 3D oxygen evolution anode, Electrochem. Commun. 49 (2014) 21–24.

[16] R. Chong, Z. Wang, J. Li, H. Han, J. Shi, C. Li, Transition metal (Ni, Fe, and Cu) hydroxides enhanced α-Fe2O3 photoanode-based photofuel cell, RSC Adv. 4 (2014) 47383–47388.

[17] M.E.G. Lyons, M.P. Brandon, Redox switching and oxygen evolution electrocatalysis in polymeric iron oxyhydroxide films, Phys. Chem. Chem. Phys. 11 (2009) 2203-2217

[18] W. D. Chemelewski, H-C. Lee, J.-F. Lin, A.J. Bard, C.B. Mullins, Amorphous FeOOH oxygen evolution reaction catalyst for photoelectrochemical water splitting, J. Am. Chem. Soc. 136 (2014) 2843−2850.

[19] R.R. Rangaraju, A. Panday, K.S. Raja, M. Misra, Nanostructured anodic iron oxide film as photoanode for water oxidation, J. Phys. D: Appl. Phys. 42 (2009) 135303

[20] M. Mohapatra, S. Anand, Synthesis and applications of nano-structured iron oxides/hydroxides - a review, Int. J. Eng. Sci. Tech. 2 (8) (2010) 127-146.

[21] D. Fu, P.G. Keech, X. Sun, J.C. Wren, Iron oxyhydroxide nanoparticles formed by forced hydrolysis: dependence of phase composition on solution concentration, Phys. Chem. Chem. Phys. 13 (2011) 18523-18529.

[22] M. Müller, J.C. Villalb, F.Q. Mariani, M. Dalpasquale, M.Z. Lemos, M.F.G. Huila, F.J. Anaissi, Synthesis and characterization of iron oxide pigments through the method of the forced hydrolysis of inorganic salts, Dyes Pigm. 120 (2015) 271-278.

[23] P. Luan, M. Xie, D. Liu, X. Fu, L. Jing, Effective charge separation in the rutile TiO2 nanorod-coupled α-Fe2O3 with exceptionally high visible activities, Sci. Rep. 4 (2014) 6180

[24] B. Kılıç, N. Gedik, S. P. Mucur, A.S. Hergul, E. Gür, Band gap engineering and modifying surface of TiO2 nanostructures by Fe2O3 for enhanced-performance of dye sensitized solar cell, Mater. Sci. Semicond. Process. 31(2015)363–371.

[25] G. Hodes, Chemical solution deposition of semiconductor films, Marcel Dekker, Inc. New York, 2002.

[26] H.M. Pathan, C.D. Lokhand, Deposition of metal chalcogenide thin films by successive ionic layer adsorption and reaction (SILAR) method. Bull. Mat. Sci., 27 (2004) 85–111.

[27] R.S. Mane, C.D. Lokhande, Chemical deposition method for metal chalcogenide thin films, Mater. Chem. Phys. 65 (2000) 1-31.

[28] G. Hodes, Comparison of dye- and semiconductor-sensitized porous nanocrystalline liquid junction solar cells, J. Phys. Chem. C, 112 (2008) 17778–17787.

[29] J. Tian, G. Cao, Semiconductor quantum dot-sensitized solar cells, Nano Reviews, 4 (2013) 22578.

[30] N. Ibrahim, S.K. Kamarudin, L.J. Minggu, Biofuel from biomass via photo-electrochemical reactions: An overview, J. Pow. Sources, 259 (2014) 33-42.

[31] M. Kanekoa, S. Suzuki, H. Uenoa, J. Nemoto, Y. Fujii, Photoelectrochemical decomposition of bio-related compounds at a nanoporous semiconductor film photoanode and their photocurrent–photovoltage characteristics, Electrochim. Acta 55 (2010) 3068–3074.

[32] L. J. Minggu, W.R.W. Daud, M.B. Kassim, An overview of photocells and photoreactors for photoelectrochemical water splitting, Int. J. Hydrogen Energy, 35 (2010) 5233-5244.

[33] G. Palmisano, V. Augugliaro, M. Pagliaro, L. Palmisano, Photocatalysis: a promising route for 21st century organic chemistry, Chem. Commun, 33 (2007) 3425–3437.

[34] Akihiko Kudo, Photocatalysis and solar hydrogen production, IUPAC, Pure Appl. Chem., 79 (2007) 1917–1927.

[35] B.N. Grgur, Basic principles and applications of photoelectrochemical reactions, Zaštita materijala, 57 (1) (2016) 93-100.

[36] https://en.wikipedia.org/wiki/List_of_semiconductor_materials

[37] A.W. Bott, Electrochemistry of Semiconductors, Current Separations, 17 (3) (1998) 87-91.

[38] S.Weinberg, Lectures on Quantum Mechanics, Cambridge University Press, Cambridge UK, 2013.

[39] S. Trasatti, The Absolute electrode potential: An explanatory note, Pure & Appl. Chem. 58 (7) (1986) 955-966.

[40] J. Bisquert, P. Cendula, L. Bertoluzzi, S. Gimenez, Energy Diagram of Semiconductor/Electrolyte Junctions, J. Phys. Chem. Lett. 5 (2014) 205−207.

[41] Y. Xu, M. A. A. Schoonen, The absolute energy positions of conduction and valence bands of selected semiconducting minerals, Am. Mineral. 85 (2000) 543-552.

[42] A. Fujishima, K. Honda, Electrochemical photolysis of water at a semiconductor electrode, Nature, 238 (1972) 37-38

[43] P. Lianos, Review of recent trends in photoelectrocatalytic conversion of solar energy to electricity and hydrogen, Applied Catalysis B: Environmental, 210 (5) (2017) 235-254.

[44] M. Kaneko, J. Nemoto, H. Ueno, N. Gokan, K. Ohnuki, M. Horikawa, R. Saito, T. Shibata, Photoelectrochemical reaction of biomass and bio-related compounds with nanoporous TiO2 film photoanode and O2-reducing cathode, Electrochem. Commun., 8 (2006) 336-340

[45] P. Lianos, Production of electricity and hydrogen by photocatalytic degradation of organic wastes in a photoelectrochemical cell: the concept of the photofuelcell: a review of a Re-Emerging research field, J. Hazard. Mater., 185 (2011) 575-590

[46] R. Michal, S. Sfaelou, P. Lianos, Photocatalysis for renewable energy production using PhotoFuelCells, Molecules, 19 (2014) 19732-19750

[47] S. Sfaelou, P. Lianos, Photoactivated Fuel Cells (PhotoFuelCells). An alternative source of renewable energy with environmental benefits, AIMS Mater. Sci., 3 (2016) 270-288

[48] L.-C. Pop, I. Tantis, P. Lianos, Photoelectrocatalytic hydrogen production using nitrogen containing water soluble wastes, Int. J. Hydrogen Energy, 40 (2015) 8304-8310

[49] M. Antoniadou, P. Lianos, Production of electricity by photoelectrochemical oxidation of ethanol in a PhotoFuelCell, Appl. Catal. B, 99 (2010) 307-313

[50] Y. Liu, J. Li, B. Zhou, X. Li, H. Chen, Q. Chen, Z. Wang, L. Li, J. Wangc, W. Cai, Efficient electricity production and simultaneously wastewater treatment via a high-performance photocatalytic fuel cell, Wat. Res. 45 (2011) 399-3998.

[51] J. Kim, D. Monllor-Satoca, W. Choi, Simultaneous production of hydrogen with the degradation of organic pollutants using TiO2 photocatalyst modified with dual surface components, Energy Environ. Sci., 5 (2012) 7647–7656.

[52] A. N. Rollinson, J. Jones, V. Dupont, M. V. Twigg, Urea as a hydrogen carrier: A perspective on its potential for safe, sustainable and long-term energy supply, Energy Environ. Sci., 4 (2011) 1216–1224.

[53] B. K. Boggs, R. L. King, G. G. Botte, Urea electrolysis: direct hydrogen production from urine, Chem. Commun., 32 (2009) 4859–4861.

[54] P.M. Glibert, J. Harrison, C. Heil, S. Seitzinger, Escalating worldwide use of urea – A global change contributing to coastal eutrophication, Biogeochemistry, 77 (3) (2006) 441–463.

[55] E. Urbańczyk, M. Sowa, W. Simka, Urea removal from aqueous solutions-a review, J. Appl. Electrochem., 46 (2016) 1011–1029.

[56] W. Yan, D. Wang, G.G. Botte, Template-assisted synthesis of Ni–Co bimetallic nanowires for urea electrocatalytic oxidation, J. Appl. Electrochem. 45 (2015) 1217–1222.

[57] R. Lan, S. Tao, J.T.S. Irvine, A direct urea fuel cell – power from fertilizer and waste, Energy Environ. Sci., 3 (2010) 438–441.

[58] W. Xu, H. Zhang, G. Li, Z. Wu, Nickel-cobalt bimetallic anode catalysts for direct urea fuel cell, Sci. Rep., 4 (2014) 5863.

[59] J. Choulera, G.A. Padgett, P.J. Cameron, K. Preussd, M-M Titiricid, I. Ieropoulosf, M. Di Lorenzo, Towards effective small scale microbial fuel cells for energy generation from urine, Electrochim. Acta 192 (2016) 89–98.

[60] G. Wang, Y, Ling, X. Lu, H. Wang, F. Qian, Y. Tong, Y. Li, Solar driven hydrogen releasing from urea and human urine, Energy Environ. Sci., 5 (2012) 8215-8219

[61] K. Cho, D. Kwonac, M.R. Hoffmann, Electrochemical treatment of human waste coupled with molecular hydrogen production, RSC Adv., 4 (2014) 4596–4608.

[62] M. Antoniadou, P. Lianos, A photoactivated fuel cell used as an apparatus that consumes organic wastes to produce electricity. Photochem. Photobiol. Sci., 10 (2011) 431-435.

[63] P. Roy, S. Berger, P. Schmuki, TiO2 nanotubes: Synthesis and applications, Angew. Chem. Int. Ed. 50 (2011) 2904 – 2939.

[64] J.C. Colmenares, R. Luque, J.M. Campelo, F. Colmenares, Z. Karpiński, A.A. Romero, Nanostructured photocatalysts and their applications in the photocatalytic transformation of lignocellulosic biomass: An Overview, Materials, 2 (2009) 2228-2258.

[65] Y. Lan, Y. Lu, Z. Ren, Mini review on photocatalysis of titanium dioxide nanoparticles and their solar applications, Nano Energy, 2 (2013) 1031–1045.

[66] G. Cacciato, M. Zimbone, F. Ruffino, M.G. Grimaldi, TiO2 nanostructures and nanocomposites for sustainable photocatalytic water purification, Chapter 4 in: Green Nanotechnology - Overview and Further Prospects, Edited by M.L. Larramendy and S. Soloneski, InTech, 2016.

[67] Z. S. Li, W.J. Luo, M. L. Zhang, J. Y. Feng, Z. G. Zou, Photoelectrochemical cells for solar hydrogen production: current state of promising photoelectrodes, methods to improve their properties, and outlook. Energy Environ. Sci. 6 (2013) 347–370.

[68] L.Q. Jing, J. Zhou, J.R. Durrant, J. Tang, D. Liu, H. Fu, Dynamics of photogenerated charges in the phosphate modified TiO2 and the enhanced activity for photoelectrochemical water splitting. Energy Environ. Sci. 5 (2012) 6552–6558.

[69] K. E. Dekrafft, C. Wang, W.B. Lin, Metal-organic framework templated synthesis of Fe2O3/TiO2 nanocomposite for hydrogen production. Adv. Mater. 24 (2012) 2014–2018.

[70] W. T. Sun, Q. Q. Meng, L.Q. Jing, D.N. Liu, Y. Cao, Facile synthesis of surface-modified nanosized α-Fe2O3 as efficient visible photocatalysts and mechanism insight. J. Phys. Chem. C 117 (2013) 1358–1365.

[71] X. Liu, K. Chen, J-J Shim, J. Huang, Facile synthesis of porous Fe2O3 nanorods and their photocatalytic properties, J. Saudi Chem. Soc. 19 (2015) 479–484.

[72] M. Danish, S. Ambreen, A. Chauhan, A. Pandey, Optimization and comparative evaluation of optical and photocatalytic properties of TiO2 thin films prepared via sol–gel method, J. Saudi Chem. Soc., 19 (2015) 557–562.

[73] Y. Lan, Y. Lu, Z. Ren, Mini review on photocatalysis of titanium dioxide nanoparticles and their solar applications, Nano Energy, (2013) 2, 1031–1045

[74] S. Chaturvedi, P.N. Dave, N.K. Shah, Applications of nano-catalyst in new era, J. Saudi Chem. Soc., 16 (3) (2012) 307–325.

[75] D.A. Hanaor, C.C. Sorrell, Review of the anatase to rutile phase transformation, J. Mat. Sci., 46 (2011) 855-874

[76] D. Eder, M. Motta, A.H. Windle, Iron-doped Pt–TiO2 nanotubes for photo-catalytic water splitting, Nanotechnology, 20 (2009) 055602 (6pp), doi:10.1088/0957-4484/20/5/055602

[77] Shigeru Kohtani, Eito Yoshioka, Hideto Miyabe. Photocatalytic Hydrogenation on Semiconductor Particles, Hydrogenation, Prof. Iyad Karamé (Ed.), InTech, 2012.

[78] R. van de Krol, Principles of Photoelectrochemical Cells. In: van de Krol R., Grätzel M. (eds) Photoelectrochemical Hydrogen Production. Electronic Materials: Science & Technology, vol 102. Springer, Boston, MA, 2012.

[79] J. Bai, Baoxue Zhou, Titanium dioxide nanomaterials for sensor applications, Chem. Rev., 114 (2014) 10131−10176.

[80] L. Zhang, Y. Zhu, Y. He, W. Li, H. Sun, Preparation and performances of mesoporous TiO2 film photocatalyst supported on stainless steel, Appl. Catal. B: Environ. 40 (2003) 287–292.

[81] S. Yang, Y. Liu, C. Sun, Preparation of anatase TiO2/Ti nanotube-like electrodes and their high photoelectrocatalytic activity for the degradation of PCP in aqueous solution, Appl. Catal. A 301 (2006) 284–291.

[82] X. Wu, Q. Jiang, Z. Ma,M. Fu, W.F. Shangguan, Synthesis of titania nanotubes by microwave irradiation, Solid State Commun. 136 (2005) 513–517.

[83] S. Srimala, C.W. Lai, Study on the formation and photocatalytic activity of titanate nanotubes synthesized via hydrothermal method, J. Alloys Compd. 490 (2010) 436–442.

[84] S.I. Na, S.S. Kim, W.K. Hong, J.W. Park, J. Jo, Y.C. Nah, T. Lee, D.Y. Kim, Fabrication of TiO2 nanotubes by using electrodeposited ZnO nanorod template and their application to hybrid solar cells, Electrochim. Acta 53 (2007) 2560–2566

[85] C.C. Chen, J.S. Lin, E.W. Diau, T.Z. Liu, Self-cleaning characteristics on a thin-film surface with nanotube arrays of anodic titanium oxide, Appl. Phys. A 92 (2008) 615–620.

[86] M. Bestetti, S. Franz, M. Cuzzolin, P. Arosio, P.L. Cavallotti, Structure of nanotubular titanium oxide templates prepared by electrochemical anodization in H2SO4/HF solutions, Thin Solid Films 515 (2007) 5253–5258.

[87] K. Bauer, S. Kleber, P. Schmuki, TiO2 nanotubes: Tailoring the geometry in H3PO4/HF electrolytes, Electrochem. Commun. 8 (2006) 1321–1325.

[88] H. Yang, C. Pan, Diameter-controlled growth of TiO2 nanotube arrays by anodization and its photoelectric property, J. Alloys Compd., 492 (2010) L33–L35.

[89] D.J. Yang, H. Park, H.G. Kim, S.J. Cho, W.Y. Choi, Fabrication of a patterned TiO2 nanotube arrays in anodic oxidation, J. Electroceram. 23 (2009) 159–163.

[90] J.M. Macak, P. Schmuki, Anodic growth of self-organized anodic TiO2 nanotubes in viscous electrolytes, Electrochim. Acta 52 (2006) 1258–1264.

[91] Z. Zhang, M.F. Hossai, T. Takahashi, Photoelectrochemical water splitting on highly smooth and ordered TiO2 nanotube arrays for hydrogen generation, Int. J. Hydrogen Energy 35 (2010) 8528–8535.

[92] J. Guo, W. Fu, H. Yang, Q. Yu, W. Zhao, X. Zhou, Y. Sui, J. Ding, Y. Li, S. Cheng, M. Li, A NiO/TiO2 junction electrode constructed using self-organized TiO2 nanotube arrays for highly efficient photoelectrocatalytic visible light activations, J.Phys. D: Appl. Phys. 43 (2010) 245202.

[93] J.M. Macak, K. Sirotna, P. Schmuki, Self-organized porous titanium oxide prepared in Na2SO4/NaF electrolytes, Electrochim. Acta 50 (2005) 3679–3684.

[94] K.M. Deen, A. Farooq, M.A.Raza, W. Haider, Effect of electrolyte composition on TiO2 nanotubular structure formation and its electrochemical evaluation, Electrochimica Acta, Volume 117, 20 January 2014, Pages 329-335

[95] M. Russo, Titanium Oxide Hydrates: Optical Properties and Applications, Doctoral thesis, University of London, 2009.

[96] J. Krysa, M. Zlamal, S. Kment, M. Brunclikova, Z. Hubicka, TiO2 and Fe2O3 films for photoelectrochemical water splitting, Molecules, 20 (2015) 1046-1058
[97] Y.-C. Lim, Z. Zainal, M. Zobir Hussein, W.-T. Tan, The effect of heat treatment on phase transphormation, morphology and photoelectrochemical response of short TiO2 nanotubes, Digest Journal of Nanomaterials and Biostructures, 8 (1) (2013) 167 – 176.
[98] A. Ghicov, H. Tsuchiya, J.M. Macak, P. Schmuki, Annealing effects on the photoresponse of TiO2 nanotubes, Phys. Stat. Sol. (a) 203 (4) (2006) R28–R30.
[99] RM Cornell, U. Schwertmann, (2003). The iron oxides: structure, properties, reactions, occurrences and uses. Wiley VCH.
[100] https://en.wikipedia.org/wiki/Iron(III)_oxide
[101] https://en.wikipedia.org/wiki/Iron_oxide
[102] M.M.V Snyder, W. Um, Adsorption mechanisms and transport behavior between selenate and seleniteon different sorbents, , Int J Waste Resources 4 (2) (2014) 100014
[103] http://rruff.info/index.php/new_search=1 RRUFF Project website containing an integrated database of Raman spectra, X-ray diffraction and chemistry data for minerals
[104] D.A. Wheeler , G. Wang , Y. Ling , Y. Li, J.Z. Zhang, Nanostructured hematite: synthesis, characterization, charge carrier dynamics, and photoelectrochemical properties, Energy Environ. Sci., 2012, 5, 6682-6702
[105] K.M.H. Young, B.M. Klahr, O. Zandi, T.W. Hamann, Photocatalytic water oxidation with hematite electrodes, Catal. Sci. Technol., 3 (2013) 1660-1671
[106] S.R. Pendlebury, M. Barroso, A.J. Cowan, K. Sivula, J.Tang, M. Gra¨tzel, D. Kluga, J.R. Durrant, Dynamics of photogenerated holes in nanocrystalline a-Fe2O3 electrodes for water oxidation probed by transient absorption spectroscopy, Chem. Commun., 47 (2011) 716–718
[107] C. Du, M. Zhang, Ji-W. Jang, Y. Liu, G.-Y. Liu, D. Wang, Observation and alteration of surface states of hematite photoelectrodes, J. Phys. Chem. C, 118 (2014) 17054−17059
[108] K. G. U. Wijayantha, S. Saremi-Yarahmadia, L.M. Peter, Kinetics of oxygen evolution at a-Fe2O3 photoanodes: a study by photoelectrochemical impedance spectroscopy, Phys. Chem. Chem. Phys., 13 (2011) 5264–5270.
[109] C.Y. Cummings, F. Marken, L.M. Peter, K.G. Upul Wijayantha, A.A. Tahir, New insights into water splitting at mesoporous α-Fe2O3 films: A study by modulated

transmittance and impedance spectroscopies, J. Am. Chem. Soc. 134 (2012) 1228−1234.

[110] L. Wanga, C.-Y. Lee, P. Schmuki, Improved photoelectrochemical water splitting of hematite nanorods thermally grown on Fe–Ti alloys, Electrochem. Comm., 44 (2014) 49-53.

[111] N.D. Jayram, D. Aishwarya, S. Sonia, D. Mangalaraj, P.S. Kumar, G.M Rao, Analysis on superhydrophobic silver decorated copper: Oxide nanostructured thin films for SERS studies, J. Colloid. Interface Sci. 477 (2016) 209-219.

[112] S. Sonia, P.S. Kumar, N.D. Jayram, Y. Masuda, D. Mangalaraj, C. Lee, Superhydrophobic and H2S gas sensing properties of CuO nanostructured thin films through a successive ionic layered adsorption reaction process, RSC Adv., 6 (2016), pp. 24290-24298

[113] A.U. Ubale, M.R. Belkhedkar, Size dependent physical properties of nanostructured α-Fe2O3 thin films grown by successive ionic layer adsorption and reaction method for antibacterial application, J. Mater. Sci. Technol., 31(1) (2015) 1-9.

[114] V. Cristino, S. Berardi, S. Caramori, R. Argazzi, S. Carli, L. Meda, A. Taccac, C.A. Bignozzi, Efficient solar water oxidation using photovoltaic devices functionalized with earth-abundant oxygen evolving catalysts, Phys. Chem. Chem. Phys. 15 (2013) 13083-13092.

[115] S. Kment, F. Riboni, S. Pausova, L. Wang, L. Wang, H. Han, Z. Hubicka, J. Krysa, P. Schmuki, R. Zboril, Photoanodes based on TiO2 and a-Fe2O3 for solar water splitting – superior role of 1D nanoarchitectures and of combined heterostructures, Chem. Soc. Rev., 46 (2017) 3716-3769.

[116] A.I. Kontos, V. Likodimos, T. Stergiopoulos, D.S. Tsoukleris, P. Falaras, Self-organized anodic TiO2 nanotube arrays functionalized by iron oxide nanoparticles, Chem. Mater., 21, (2009) 662–672.

[117] T. H. Jeon, W. Choi, H. Park, Photoelectrochemical and photocatalytic behaviors of hematite-decorated titania nanotube arrays: Energy level mismatch versus surface specific reactivity, J. Phys. Chem. C, 115 (2011) 7134–7142.

[118] S.K. Mohapatra, S. Banerjee, M. Misra, Synthesis of Fe2O3/TiO2 nanorod–nanotube arrays by filling TiO2 nanotubes with Fe, Nanotechnology, 19 (2008) 315601

[119] S. Li, P. Zhang, X. Song, L. Gao, Ultrathin Ti-doped hematite photoanode by pyrolysis of ferrocene, Int. J. Hydrogen Energy, 39 (27) (2014) 14596-14603

[120] D. Barreca, G. Carraro, A. Gasparotto, C. Maccato, M.E.A. Warwick, K. Kaunisto, C. Sada, S. Turner, Y. Gönüllü, T.-P. Ruoko, L. Borgese, E. Bontempi, G. Van Tendeloo, H. Lemmetyinen, S. Mathur, Fe2O3–TiO2 Nano-heterostructure photoanodes for highly efficient solar water oxidation, Adv. Mater. Interfaces, 2 (17) (2015) 1500313.

[121] X. Zhang, Y. Xie, H. Chen, J. Guo, A. Meng, C. Li, One-dimensional mesoporous Fe2O3@TiO2 core–shell nanocomposites: Rational design, synthesis and application as high-performance photocatalyst in visible and UV light region, Appl. Surf. Sci., 317 (2014) 43-48.

[122] Y. Ling, P. Steven, L. Hwai, C. Ong, W.T. Chong, Synthesis, characteristics and sonocatalytic activities of calcined γ-Fe2O3 and TiO2 nanotubes/γ-Fe2O3 magnetic catalysts in the degradation of Orange G, Ultrasonics Sonochemistry, 29 (2016) 317-327.

[123] C. Cao, C. Hu, W. Shen, S. Wang, S. Song, M. Wang, Improving photoelectrochemical performance by building Fe2O3 heterostructure on TiO2 nanorod arrays, Mat. Res. Bull., 70 (2015) 155-162.

[124] X. Li, H. Lin, X. Chen, H. Niu, J. Liu, T. Zhang, F. Qu, Dendritic α-Fe2O3/TiO2 nanocomposites with improved visible light photocatalytic activity, Phys. Chem. Chem. Phys., 18 (2016) 9176-9185

[125] M. Žic, M. Ristić, S. Musić, Monitoring the hydrothermal precipitation of α-Fe2O3 from concentrated Fe(NO3)3 solutions partially neutralized with NaOH, J. Mol. Struct. 993 (2011) 115–119.

[126] W. Kraus, G. Nolze, PowderCell for Windows, V.2.4, Federal Institute for Materials Research and Testing, Berlin, Germany, 2000.

[127] D. Maiti, P.S. Devi, Selective formation of iron oxide and oxyhydroxide nanoparticles at room temperature: Critical role of concentration of ferric nitrate, Mater. Chem. Phys., 154 (2015) 144-151.

[128] M. Ristić, S. Musić, M. Godec, Properties of γ -FeOOH, α-FeOOH and α-Fe2O3 particles precipitated by hydrolysis of Fe3+ ions in perchlorate containing aqueous solutions, J. Alloys Compd. 417 (2006) 292–299.

[129] M. Gotić, S. Musić, Mössbauer, FT-IR and FE SEM investigation of iron oxides precipitated from FeSO4 solutions, J. Mol. Struct. 834–836 (2007) 445–453.

[130] J.E. Iglesias, C.J. Serna, The IR spectra of hematite-type compounds with different particle shapes, Miner. Petrogr. Acta, 29A (1985) 363-370.

[131] A.N. Christensen, T.R. Jensen, C.R.H. Bahl, E. DiMasi, Nano size crystals of goethite, α-FeOOH: Synthesis and thermal transformation, J. Solid State Chem. 180 (2007) 1431–1435.

[132] D. Fu, P. G. Keech, X. Sun, J.C. Wren, Iron oxyhydroxide nanoparticles formed by forced hydrolysis: dependence of phase composition on solution concentration, Phys. Chem. Chem. Phys. 13 (2011) 18523-18529.

[133] Y. Dai, Y. Sun, J. Yao, D. Ling, Y. Wang, H. Long, X. Wang, B. Lin, T.H. Zeng, Y. Sun, Graphene-wrapped TiO2 nanofibers with effective interfacial coupling as ultrafast electron transfer bridges in novel photoanodes, J. Mater. Chem. A 2 (2014) 1060–1067.

[134] A. Mazare, I. Paramasivam, K. Lee, P. Schmuki, Improved water-splitting behaviour of flame annealed TiO2 nanotubes, Electrochem. Commun. 13 (2011) 1030-1034.

[135] K. Siuzdak, M. Szkoda, M. Sawczaka, A. Lisowska-Oleksiak, Novel nitrogen precursors for electrochemically driven doping of titania nanotubes exhibiting enhanced photoactivity, New J. Chem., 39 (2015) 2741-2751.

[136] M. Radecka, M. Rekas, A. Trenczek-Zajac, K. Zakrzewska, Importance of the band gap energy and flat band potential for application of modified TiO2 photoanodes in water photolysis, J. Power Sources 181 (2008) 46–55.

[137] R R Rangaraju, A Panday, K S Raja and M Misra, Nanostructured anodic iron oxide film as photoanode for water oxidation, J. Phys. D: Appl. Phys. 42 (2009) 135303

[138] Y. Jih-Sheng, L. Wan-Hsien, L. Chia-Yu, W. Bo-Sheng, W Jih-Jen, n‑Fe2O3 to N+‑TiO2 heterojunction photoanode for photoelectrochemical water oxidation, ACS Appl. Mater. Interfaces 7 (2015) 13314−13321.

[139] R. Beranek, (Photo)electrochemical methods for the determination of the band edge positions of TiO2-based nanomaterials, Adv. Phys. Chem. 2011 (2011) doi:10.1155/2011/786759

[140] G. Milazzo, S. Caroli, Tables of Standard Electrode Potentials, John Wiley & Sons, Chichester, New York 1978.

[141] M.A. Ghanema, A.M. Al-Mayoufa, M.N. Shaddada, F. Markenc, Selective formation of hydrogen peroxide by oxygen reduction on TiO2 nanotubes in alkaline media, Electrochim. Acta 174 (2015) 557–562.

[142] K. Sivula, Nanostructured α-Fe2O3 Photoanodes, in: Photoelectrochemical Hydrogen Production, Chapter 4, Eds.: R. van de Krol and M. Graetzel, Springer, N.Y., Dordrecht Heidelberg London, 2011.

[143] M. Barroso, S. R. Pendlebury, A.J. Cowan, J.R. Durrant, Charge carrier trapping, recombination and transfer in hematite (α-Fe2O3) water splitting photoanodes, Chem. Sci. 4 (2013) 2724–2734.

[144] L.M. Peter, Energetics and kinetics of light-driven oxygen evolution at semiconductor electrodes: the example of hematite. J. Solid State Electrochem. 17 (2) (2013) 315-326.

[145] M. Orlandi, S. Caramori, F. Ronconi, C.A. Bignozzi, Z. El Koura, N. Bazzanella, L. Meda, A. Miotello, Pulsed-laser deposition of nanostructured iron oxide catalysts for efficient water oxidation, ACS Appl. Mater. Interfaces, 6 (2014) 6186−6190.

[146] B. Klahr, S. Gimenez, F. Fabregat-Santiago, T. Hamann, J. Bisquert, Water oxidation at hematite photoelectrodes: The role of surface states, J. American Chem. Soc. 134 (2012) 4294-4302.

[147] N. Yatom, O. Neufeld, M. C. Toroker, Toward settling the debate on the role of Fe2O3 surface states for water splitting, J. Phys. Chem. C, 119 (2015) 24789−24795.

[148] Â.C.S. Bezerra, E.L. de Sá , F.C. Nart, In situ vibrational study of the initial steps during urea electrochemical oxidation, J. Phys. Chem. B, 101 (33) (1997) 6443–6449.

[149] Grgur, B.N., Mijin, D.T, A kinetics study of the methomyl electrochemical degradation in the chloride containing solutions, App. Cat. B: Environ. 147 (2013) 429-438.

BIOGRAPHY

Waleed Mohammed Omymen, Master Technology Engineer, was born April 8, 1977 in Tripoli, Libya. He completed his basic academic studies in 2000 at Al-Mergheb University, Al-Khoms, Libya at the Department of Chemical Engineering. He completed his MA in 2009 at Alfateh University, Tripoli, Libya, in the field of Chemical Engineering. Since his graduation, he has been employed as an assistant lecturer at Al-Mergheb University, Al-Khoms, Department of Chemistry, Libya, where he holds lectures in general chemistry and polymer chemistry, and general chemistry and organic chemistry at Al-Khoms College, Al-Khoms, Libya, and exercises in Mathematics II. School year 2014/2015 he enrolled in doctoral studies at the Faculty of Technology and Metallurgy, University of Belgrade, Department of Chemical Engineering. He is the Author of two scientific papers.

BIOGRAFIJA

Waleed Mohammed Omymen, master inženjer tehnologije, je rođen 8 April 1977 u Tripoli, Libya. Osnovne akademske studije završio je 2000 godine, na Al-Mergheb University, Al-Khoms, Libya na odseku za Hemijsko inženjerstvo. Master studije je završio 2009 godine na Alfateh University, Tripoli, Libya, smer Hemijsko inženjerstvo. Od završetka master studija zaposlen je kao pomoćni predavač na Al-Mergheb University, Al-Khoms, Department za Hemijsko inženjerstvo, Libya gde drži predavanja iz predmeta Opšta hemija i Polimerna hemija, i vežbe iz predmeta opšta hemija i organska hemije a na Al-Khoms College, Al-Khoms, Libya, vežbe iz Matematike II. Školske 2014/2015 upisao je doktorske studije na Tehnološko-metalurškom fakultetu, Univerziteta u Beogradu, odsek za Hemijsko inženjerstvo. Do sada je autor jednog rada u vrhunskom (M21) i istaknutom (M22) međunarodnom časopisu.

Radovi proizašli iz disertacije/Papers from the Dissertation

M21. Rad u vrhunskom međunarodnom časopisu

1. **Omymen Waleed M.**, Ebshish Ali S., Jugović Branimir Z., Trišović Tomislav Lj., Gvozdenović Milica M., Grgur Branimir N., *Photoelectochemical behavior of TiO2-NT's modified with SILAR deposited iron oxide*,- Electrochimica Acta, Vol 203, 2016, pp. 136–143. ISSN 0013-4686 IF(2016)= 4.803

M22. Rad u istaknutom međunarodnom časopisu

1. **Omymen Waleed M**., Rogan Jelena R., Jugović Branimir Z., Gvozdenović Milica M., Grgur Branimir N., *Photo-assisted electrochemical oxidation of the urea onto TiO2-nanotubes modified by hematite*,- Journal of Saudi Chemical Society, 2017, DOI: 10.1016/j.jscs.2017.05.010 IF (2016) 2.887

Прилог 1.

Изјава о ауторству

Потписани-а Waleed Mohammed Omymen

број индекса 4043/2014

Изјављујем

да је докторска дисертација под насловом

Photoelectrochemical cell based on titanium dioxide nanotubes modified by iron oxide

- резултат сопственог истраживачког рада,
- да предложена дисертација у целини ни у деловима није била предложена за добијање било које дипломе према студијским програмима других високошколских установа,
- да су резултати коректно наведени и
- да нисам кршио/ла ауторска права и користио интелектуалну својину других лица.

Потпис докторанда

У Београду, _____

_____

Прилог 2.

Изјава о истоветности штампане и електронске верзије докторског рада

Име и презиме аутора Waleed Mohammed Omymen

Број индекса 4043/2014

Студијски програм Хемијско инжењерство

Наслов рада Photoelectrochemical cell based on titanium dioxide nanotubes modified by iron oxide
Ментор Др Бранимир Гргур, ред. проф.

Потписани/а Waleed Mohammed Omymen

Изјављујем да је штампана верзија мог докторског рада истоветна електронској верзији коју сам предао/ла за објављивање на порталу **Дигиталног репозиторијума Универзитета у Београду.**

Дозвољавам да се објаве моји лични подаци везани за добијање академског звања доктора наука, као што су име и презиме, година и место рођења и датум одбране рада.

Ови лични подаци могу се објавити на мрежним страницама дигиталне библиотеке, у електронском каталогу и у публикацијама Универзитета у Београду.

Потпис докторанда

У Београду, _____

_____

Прилог 3.

Изјава о коришћењу

Овлашћујем Универзитетску библиотеку „Светозар Марковић“ да у Дигитални репозиторијум Универзитета у Београду унесе моју докторску дисертацију под насловом:

Photoelectrochemical cell based on titanium dioxide nanotubes modified by iron oxide

која је моје ауторско дело.

Дисертацију са свим прилозима предао/ла сам у електронском формату погодном за трајно архивирање.

Моју докторску дисертацију похрањену у Дигитални репозиторијум Универзитета у Београду могу да користе сви који поштују одредбе садржане у одабраном типу лиценце Креативне заједнице (Creative Commons) за коју сам се одлучио/ла.

1. Ауторство

2. Ауторство - некомерцијално

3. Ауторство – некомерцијално – без прераде

4. Ауторство – некомерцијално – делити под истим условима

5. Ауторство – без прераде

6. Ауторство – делити под истим условима

(Молимо да заокружите само једну од шест понуђених лиценци, кратак опис лиценци дат је на полеђини листа).

Потпис докторанда

У Београду, _____

_____

1. Ауторство - Дозвољавате умножавање, дистрибуцију и јавно саопштавање дела, и прераде, ако се наведе име аутора на начин одређен од стране аутора или даваоца лиценце, чак и у комерцијалне сврхе. Ово је најслободнија од свих лиценци.

2. Ауторство – некомерцијално. Дозвољавате умножавање, дистрибуцију и јавно саопштавање дела, и прераде, ако се наведе име аутора на начин одређен од стране аутора или даваоца лиценце. Ова лиценца не дозвољава комерцијалну употребу дела.

3. Ауторство - некомерцијално – без прераде. Дозвољавате умножавање, дистрибуцију и јавно саопштавање дела, без промена, преобликовања или употребе дела у свом делу, ако се наведе име аутора на начин одређен од стране аутора или даваоца лиценце. Ова лиценца не дозвољава комерцијалну употребу дела. У односу на све остале лиценце, овом лиценцом се ограничава највећи обим права коришћења дела.

4. Ауторство - некомерцијално – делити под истим условима. Дозвољавате умножавање, дистрибуцију и јавно саопштавање дела, и прераде, ако се наведе име аутора на начин одређен од стране аутора или даваоца лиценце и ако се прерада дистрибуира под истом или сличном лиценцом. Ова лиценца не дозвољава комерцијалну употребу дела и прерада.

5. Ауторство – без прераде. Дозвољавате умножавање, дистрибуцију и јавно саопштавање дела, без промена, преобликовања или употребе дела у свом делу, ако се наведе име аутора на начин одређен од стране аутора или даваоца лиценце. Ова лиценца дозвољава комерцијалну употребу дела.

6. Ауторство - делити под истим условима. Дозвољавате умножавање, дистрибуцију и јавно саопштавање дела, и прераде, ако се наведе име аутора на начин одређен од стране аутора или даваоца лиценце и ако се прерада дистрибуира под истом или сличном лиценцом. Ова лиценца дозвољава комерцијалну употребу дела и прерада. Слична је софтверским лиценцама, односно лиценцама отвореног кода.